

MASSIVE DISTRIBUTED COMPUTATIONAL
ALGORITHM FOR SIMULATING MANY-BODY
HYDRODYNAMIC INTERACTIONS

A Dissertation

Presented to the Faculty of the Graduate School

of Cornell University

in Partial Fulfillment of the Requirements for the Degree of

Doctor of Philosophy

by

Yu Su

December 2018

© 2018 Yu Su

ALL RIGHTS RESERVED

MASSIVE DISTRIBUTED COMPUTATIONAL ALGORITHM FOR SIMULATING MANY-BODY HYDRODYNAMIC INTERACTIONS

Yu Su, Ph.D.

Cornell University 2018

Complex fluids comprise two phases of materials: a solvent phase and a non-continuum phase such as microscopic particles or polymers. Suspensions of colloids – microscopic particles small enough to undergo Brownian motion – are an important example and model system for understanding general complex fluids. The particles are distributed in the suspending solvent, forming a “microstructure”. The formulation of detailed models for the dynamics of condensed soft matter including colloidal suspensions and other complex fluids requires accurate description of the physical forces between microstructural constituents. In dilute suspensions, pair-level interactions are sufficient to capture hydrodynamic, interparticle, and thermodynamic forces. In dense suspensions, many-body interactions must be considered. Prior analytical approaches to capturing such interactions such as mean-field approaches replace detailed interactions with averaged approximations [104]. However, long-range coupling and effects of concentration on local structure, which may play an important role in e.g. phase transitions, are smeared out in such approaches. An alternative to such approximations is the detailed modeling of hydrodynamic interactions utilizing precise couplings between moments of the hydrodynamic traction on a suspended particle and the motion of that or other suspended particles. For two isolated spheres, a set of these functions was calculated by Jeffrey and Onishi [84], Kim and Karrila [88], and Jeffrey [83]. Along with pioneering work

by Batchelor and Green [16], Batchelor [13], these are the touchstone for low-Reynolds-number hydrodynamic interactions and have been applied directly in the solution of many important problems related to the dynamics of dilute colloidal dispersions. The Reynolds number, Re , is the dimensionless strength of flow inertia relative to viscous stress, $Re = \rho UL/\eta$, where ρ is the fluid density, η is the fluid viscosity, U is the characteristic speed of the flow, and L is the characteristic length scale such as channel width, particle size, or a surface dimension.

The overall goal of this dissertation is development of new theoretical and computational models for many-body interactions in concentrated colloidal suspensions. In the first part of the dissertation, we extend the theoretical framework of the pair-level mobility functions to concentrated systems, utilizing a new stochastic sampling technique we developed in order to rapidly calculate an analogous set of mobility functions describing the hydrodynamic interactions between two hard spheres immersed in a suspension of arbitrary concentration. This was carried out utilizing Accelerated Stokesian Dynamics [28, 55, 133, 8] simulations. These mobility functions provide precise, radially dependent couplings of hydrodynamic traction moments to particle velocity derivatives, for arbitrary colloid volume fraction $\phi = 4\pi\eta a^3/n$, where η is the suspending solvent viscosity, a is the hydrodynamic particle radius, and $n = N/V$ is the number density of colloids in the volume V of solvent. The most significant outcome of this work was to show that hydrodynamic entrainment of one particle by the disturbance flow created by a forced particle decays algebraically just as slowly as a dilute suspension: it decays linearly in the inverse separation distance, $1/r$, between the forced particle and a test particle a distance r away. In contrast with prior assertions in the literature that crowding screens hydro-

dynamic interactions, this finding holds for volume fractions $0.05 \leq \phi \leq 0.5$. At these higher concentrations, the coefficients also reveal liquid-like structural effects on pair mobility at close separations. These results confirm that long-range many-body hydrodynamic interactions are an essential part of the dynamics of concentrated systems and that care must be taken when applying renormalization schemes. In Chapter 3, this stochastic technique developed in Chapter 2 is utilized to compute pair mobility couplings between stresslet and straining motion, higher-order traction moments required for many-body couplings away from equilibrium. Thus, the couplings presented in these two chapters constitute a set of orthogonal coupling functions that are utilized to compute equilibrium properties in suspensions at arbitrary concentration and to solve many-body hydrodynamic interactions analytically.

We utilize these concentrated mobility functions to extend recently developed dilute theory for the stress in concentrated colloidal suspensions, and compare those results to direct measurement in dynamic simulation. Particle-phase stress in flowing colloidal suspensions represents the extent to which energy is stored entropically or enthalpically by microstructural distortion, minus the energy dissipated by viscous drag. It was recently shown that pair-level hydrodynamic interactions suppress energy storage in dilute dispersions of repulsive hard spheres, with corresponding changes in normal stresses, normal stress differences, and osmotic pressure [39]. In the pair limit, particle roughness or Brownian motion leads to non-Newtonian rheology, whereas pair-level hydrodynamic interactions preserve the structural fore-aft symmetry and contributes to Newtonian rheology. However, in concentrated suspensions where three-body hydrodynamic interactions matter, how three-body interactions mechanistically change rheology is not fully understood. In Chapter 4, we investigate

the dependence of non-Newtonian rheology of colloidal dispersions on particle concentration, with a focus on the role of played by pair-level and three-body particle interactions. To do so, we utilize Accelerated Stokesian Dynamics to simulate the evolution of particle-phase stress in concentrated colloidal dispersions undergoing microrheological flow, obtaining detailed measurements of particle structure and dynamics as they evolve with particle concentration, and connect these to changes in non-Newtonian rheology. We find that, in contrast to dilute suspensions where pair hydrodynamic interactions suppress normal stresses and osmotic pressure, suspension stress is enhanced by three-body hydrodynamic interactions, where their role in promoting structural asymmetry produces a concentration-dependent non-Newtonian rheology. The loss of fore-aft symmetry of a pair trajectory in the presence of a third particle inspires us to seek a concentration-dependent hydrodynamic coupling that predicts non-Newtonian behavior under the influence of many-body interactions. To do so, we utilize the set of concentrated pair hydrodynamic functions developed in Chapter 2 to extend dilute theory to concentrated suspension via scaling arguments. Scaling theory and simulations show excellent agreement for the normal stress difference and osmotic pressure, providing support for the idea that, in the presence of a third particle, the transverse displacement of a pair encounter is responsible for the non-Newtonian rheology. We also find that microviscosity is enhanced as concentration increases, and we developed a scaling theory which collapses data of different volume fractions onto the dilute theory.

Many-body hydrodynamic interactions play a crucial role in colloidal suspensions , but are notoriously difficult and expensive to model computationally. The Stokesian Dynamics [28, 55] algorithm is one approach to involve many-body hydrodynamic interactions that couple fluid and particle motion, with the

primary advantage that detailed fluid motion is not explicitly computed, saving considerable computational expense. However, since hydrodynamic disturbance flows propagate between the particles in an infinite hierarchy of reflections, modeling these so-called many-body hydrodynamic interactions requires multiple matrix operations that drive the primary computational expense of the algorithm. Separation of interactions into near-field and far-field calculations permits analytical treatment of the former and faster computation overall. But in its most optimized form – Accelerated Stokesian Dynamics (ASD) [133], the algorithm is serial and can handle at most a few thousand particles. However, ever-increasing interest in understanding properties of large-scale systems in colloidal suspensions, such as colloidal gels, has demanded development of techniques to simulate $O(10^5)$ particles. Currently techniques to handle such large-scale systems, such as LAMMPS [127], neglect hydrodynamic interactions. Other techniques which consider hydrodynamic interactions between colloids utilizing GPU architecture [139] are limited to pair-level hydrodynamic interactions. However, many open questions in the complex fluids literature – such as the mechanism of the colloidal glass transition, the role of hydrodynamics in colloidal gel collapse, and more – require accurate modeling of concentrated, hydrodynamically interacting colloids. These systems require $O(10^5)$ to $O(10^6)$ particles to evolve a statistically representative set of network structures [95, 149]. In chapter 5, we present a scalable and parallel algorithms of Accelerated Stokesian Dynamics in a distributed memory architecture to fulfill the requirement of simulating large scale particle systems suspended in Stokes flow. We solve the ASD equations with Krylov subspace methods for the sparse near-field two-body interactions and for the full many-body far-field interactions. The far-field action is matrix-free and is based on Fast Fourier Transforms. We

treat in details the cases of shear flow, brownian motion, and the introduction of attractive inter-particle force. The parallelization of the different phases of the algorithm are presented and analyzed and we show scaling up to 8192 processors for 819,200 particles.

BIOGRAPHICAL SKETCH

The author was born and grew up in China. He received his bachelor of science degree after four years' undergraduate study in Peking University. He moved to Cornell University in 2012 to pursue the master of engineering degree, and then decided to further pursue a PhD degree in Chemical Engineering, studying distributed scientific computing and fluid mechanics. During research period, he showed more and more interest in computer science and would like to develop his future career in parallel computing.

ACKNOWLEDGEMENTS

This dissertation arose in part out of five years of research that has been conducted since September 2013. In this period, I have worked with people whose contribution in assorted ways has fostered this research and brought me great experience. It is a pleasure to convey my gratitude to them all in my humble acknowledgement.

I would like to record my gratitude to my advisor Prof. Roseanna N. Zia for her genuine interest in science and my development as a scholar.

I gratefully acknowledge Prof. Donald L. Koch and Prof. David Bindel for being my research committee members.

I am pleased to be friends with my fellow groupmates and colleagues, who contributed so much to making it a memorable experience to work in Cornell: Christian Aponte-Rivera, Henry Chu, Benjamin E. Dolata, Emma Gonzalez Gonzalez, Nicholas J. Hoh, Derek E. Huang, Lilian C. Johnson, Benjamin J. Landrum, Ritesh P. Mohanty, Gaddiel Quaknin, Poornima Padmanabhan and Jialun Wang. In particular, I would like to thank Henry Chu, with whom I had many fruitful discussions.

I would like to thank my wife Yan Deng for your support. It is so amazing to meet you at Cornell!

Finally, thank you Mum and Dad for your unconditional love and support, and bringing me to this world to experience so many wonderful things in life.

TABLE OF CONTENTS

Biographical Sketch	iii
Acknowledgements	iv
Table of Contents	v
List of Figures	vii
1 Background	1
1.1 Overview of many-body hydrodynamic interactions	1
1.2 Accelerated Stokesian Dynamics (ASD) algorithm	5
1.3 Non-Newtonian rheology with many-body hydrodynamic interactions	12
2 Pair mobility functions for rigid spheres in concentrated colloidal dispersions: force, torque, translation, and rotation	15
2.1 Introduction	15
2.2 Hydrodynamic couplings	20
2.3 Computational approach	22
2.4 Results	29
2.5 Conclusions	39
2.6 Appendix	41
3 Pair mobility functions for rigid spheres in concentrated colloidal dispersions: stresslet and straining motion couplings	43
3.1 Introduction	43
3.2 Hydrodynamic couplings	44
3.3 Computational approach	47
3.4 Results	51
3.5 Summary and Conclusions	62
3.6 Appendix: Evaluation of the hydrodynamic coefficients	64
4 Microviscosity, normal stress and osmotic pressure of Brownian suspensions by Accelerated Stokesian Dynamics simulation	68
4.1 Introduction	68
4.2 Microrheology model system	74
4.3 Measurement of rheological quantities	74
4.3.1 Microviscosity	75
4.3.2 Suspension stress	76
4.4 Simulation Method	79
4.5 Results	83
4.5.1 Microstructure	83
4.5.2 Rheology	89
4.5.3 Scaling theory	94
4.6 Summary and Conclusions	104

5 Large-scale accelerated Stokesian dynamics simulation with many-body hydrodynamic interactions	106
5.1 Introduction	106
5.2 Parallel Algorithms	113
5.2.1 Overview	113
5.2.2 Initial Configuration Generation	114
5.2.3 Short-range hydrodynamic interactions	116
5.2.4 Long-range hydrodynamic interactions	117
5.2.5 Near-Field and Far-Field Inverse	125
5.2.6 Correlated Brownian motion with hydrodynamic interactions	126
5.3 Results	131
5.3.1 Validation results	131
5.3.2 Scaling Results	133
5.3.3 Large-scale dynamic simulation example: colloidal gels	141
5.4 Summary	143
6 Conclusion	145

LIST OF FIGURES

<p>2.1 Model system of identically sized colloidal hard spheres, with test particles α and β at separation r. A force F_1 exerted on particle β produces a fluid disturbance that decays as $1/r$, entraining fluid and nearby particles. From [150], with permission.</p> <p>2.2 Longitudinal and transverse mobility coefficients coupling force on the surface of a particle to the motion of that and other particles. Solid lines: dilute theory of Jeffrey and Onishi[84], scaled on the concentrated self-mobility as measured in simulation in the present study. Symbols: simulation results from present study for volume fraction $\phi = 0.05$. From [150], with permission.</p> <p>2.3 Longitudinal and transverse mobility coefficients coupling force on the surface of a particle to the motion of that and other particles, in a concentrated suspension. Solid lines: dilute theory of Jeffrey and Onishi[84], scaled on the volume-fraction dependent short-time self-diffusivity of a particle as determined in simulation in the present study. Symbols: simulation results from present study for volume fractions as shown in legend. (a) Longitudinal self- and pair-mobility. (b) Transverse self- and pair-mobility. From [150], with permission.</p> <p>2.4 Effective viscosity re-scaling. (a) Longitudinal and (b) transverse force-velocity coupling. Solid lines: dilute theory of Jeffrey and Onishi[84], scaled on the volume-fraction dependent high-frequency viscosity $\eta'(\phi)$ as determined in simulation in the present study. Symbols: simulation results from present study for volume fractions as shown in legend. From [150], with permission.</p> <p>2.5 Relative mobility in concentrated suspensions. (a) Longitudinal and (b) Transverse relative mobility for a range of concentrations as shown in legend. Dashed lines: concentration-dependent short-time self-diffusivity as computed in simulation. Symbols: relative mobility as computed in simulation in the present study, for volume fractions as shown in legend. From [150], with permission.</p> <p>2.6 Torque-rotation coupling: the self-mobility coupling the torque on one particle and its own and others' rotation. Solid lines: dilute theory of Jeffrey and Onishi[84], scaled on the concentration-dependent rotational self-diffusivity as measured in dynamic simulation in the present study. Symbols: longitudinal and transverse self-mobility coefficients for a range of concentrations, as shown in the legend. From [150], with permission.</p> <p>2.7 Torque-rotation coupling: the pair-mobility coupling the torque on one particle and its own and others' rotation. Solid lines: dilute theory of Jeffrey and Onishi[84], scaled on the concentration-dependent rotational self-diffusivity as measured in dynamic simulation in the present study. Symbols: (a) longitudinal and (b) transverse pair-mobility coefficients for a range of concentrations, as shown in the legend. From [150], with permission.</p>	<p>17</p> <p>28</p> <p>28</p> <p>28</p> <p>30</p> <p>33</p> <p>34</p> <p>35</p>
--	---

2.8	Force-rotation coupling: the self- and pair-mobility coupling the force on one particle and its own and others' rotation. (a) Self- and (b) pair-mobility coefficients for a range of concentrations, as shown in the legend. Solid lines: dilute theory of Jeffrey and Onishi[84], scaled on an average of the concentration-dependent rotational and translational self-diffusivity as measured in dynamic simulation in the present study. Symbols: coefficients computed via dynamic simulation. From [150], with permission.	38
3.1	Longitudinal and transverse mobility coefficients coupling hydrodynamic stresslet, S^H , on the surface of a particle to the hydrodynamic force, F^H , of that and other particles. (a) Profile of longitudinal coupling, x^g . (b) Profile of transverse coupling, y^g . (c) Self mobility coefficients, x_{11}^g and y_{11}^g ; (d) Pair mobility coefficients, x_{21}^g and y_{21}^g . Lines: dilute theory of Kim and Mifflin [89]. Symbols: simulation results from present study for volume fraction $\phi = 0.01$. From [136], with permission.	50
3.2	Longitudinal and transverse mobility coefficients coupling stresslet on the surface of a particle to the force of that and other particles, in a concentrated suspension. Solid lines: dilute theory of Kim and Mifflin [89]. Symbols: simulation results from present study for volume fractions as shown in legend. (a) Longitudinal self-mobility. (b) Longitudinal pair-mobility. (c) Transverse self-mobility. (d) Transverse pair-mobility. The inset of the figures are the log-log plots of the couplings, indicating the decay rate holds as concentration increases. The log-log plot of transverse self-mobility is not shown because the couplings fluctuate around zero. From [136], with permission.	52
3.3	Transverse mobility coefficients coupling stresslet on the surface of a particle to the torque of that and other particles, in a concentrated suspension. Solid lines: dilute theory of Kim and Mifflin [89]. Symbols: simulation results from present study for volume fractions as shown in legend. (a) Transverse self-mobility. (b) Transverse pair-mobility. The inset of (a) represents the profile of the couplings. The inset of (b) shows the log-log plot of transverse pair-mobility, indicating the decay rate holds as concentration increases. From [136], with permission.	53
3.4	Longitudinal, transverse and perpendicular mobility coefficients coupling stresslet on the surface of a particle to the strain of that and other particles, in a concentrated suspension. Solid lines: dilute theory of Kim and Mifflin [89]. Symbols: simulation results from present study for volume fractions as shown in legend. (a) Longitudinal mobility. (b) Transverse mobility. (c) Perpendicular mobility. The insets of (a) and (b) represent the profile of longitudinal and transverse couplings, respectively. From [136], with permission.	56
3.5	Pair distribution function $g(r)$, as a function of distance from particle center, r , for volume fraction $\phi = 0.45$. The solid line is the theoretical results calculated from Percus-Yevick equation [122]. The dash line is the measurement from our simulation. From [136], with permission.	62

3.6	High-frequency viscosity as a function of volume fraction. The symbols are from evaluating Equation (3.21) utilizing the concentrated mobility function $m(r, \phi)$. The solid line is the result of dynamic simulations from Sierou and Brady [133]. From [136], with permission.	63
4.1	Evolution of the microstructure from a side-view of the simulation cell transverse to probe forcing. The black region represents the probe and it is surrounded by a region excluded to particle centers. Probe forcing Pe increases from left to right, and volume fraction ϕ increases from top to bottom, as labeled. Regions in dark red indicate particle-center accumulation; blue regions indicate particle-center depletion.	84
4.2	Equilibrium pair distribution function $g(r)$ computed from Percus-Yevick equation ([122]) for different volume fractions.	85
4.3	The first (largest) peak of pair distribution function $g(r)$, calculated by accounting all upstream bath particles and ignore the angular distribution. The peak value of $g(r)$ is shown as a function of volume fraction ϕ and probe forcing Pe	86
4.4	Microviscosity as a function of Pe and ϕ_b . Symbols are simulation results from present study; open symbols at far right correspond to $Pe^{-1} = 0$	89
4.5	Suspension stress as functions of ϕ_b and Pe : (a) parallel normal stress; (b) perpendicular normal stress; (c) first normal stress difference; (d) osmotic pressure. Filled symbols are simulation results, solid lines are dilute theory from Chu & Zia, 2015.	92
4.6	High- Pe scaling theory (Eq. 4.28) of suspension stress, as a function of ϕ_b and Pe : (a) parallel normal stress; (b) perpendicular normal stress; (c) first normal stress difference; (d) osmotic pressure. The filled symbols are simulation results. The solid lines are dilute theory from [39].	100
4.7	Low- Pe scaling (Eq. 4.30) of the osmotic pressure as a function of ϕ_b and Pe : (a) total osmotic pressure before scaling; (b) total osmotic pressure after scaling; (c) hydrodynamic osmotic pressure before scaling; (d) hydrodynamic osmotic pressure after scaling. The filled symbols are simulation results. The solid lines are dilute theory of Chu and Zia [39].	101
4.8	Microviscosity as a function of Pe and ϕ_b . The solid line is dilute theory [87]. The filled symbols are the scaled simulation results with finite Pe	103

5.1	A system with two particles and two processors has a higher entropy if each processor can generate particles everywhere in the global domain. Indeed, if each processor is allowed to generate only in its local region the number of possible configurations is proportional to $\frac{V^2}{4}$ where V is the volume of the global domain. That is if the red particle belongs to the light blue processor and the magenta particle belongs to the dark blue processor only the upper left initial configuration can be generated. However if we allow each processor to generate particles anywhere in the global domain, the number of possible configurations is proportional to V^2 and the three other quadrants are also feasible initial configurations. In short if one allows only local generation there is a reduction of entropy proportional to $N_p \times \log P$	115
5.2	The processor grid topology for short range interactions follows a 3D domain decomposition and splits the computational domain in a way to minimize communication among neighborhood processors. Each processor (red) communicates with six of its neighbor (green) and receives the information of all the ghost particles.	117
5.3	Before performing the FFT, the particles forces are interpolated from their center locations to an uniform grid. After performing the Ewald sum and the IFFT, the velocities at the grid points are interpolated back to the particles center location. (This figure is 2D only for illustration: all our simulations are 3D.)	120
5.4	Different parallel algorithms use different data layout distribution and have different processor grid topologies. In (a), a 3D domain decomposition which is typically used for short-range interaction. In (b) 1D domain decomposition which is used for the <i>fftw3</i> . In (c) a 2D domain decomposition which is used for the <i>p3dfft</i>	121
5.5	Parallel Interpolation: before performing the FFT, the particles velocities need to be interpolated from their center locations to an uniform grid. However, when doing so, interpolation needs to be coupled with communication. As we can see on the figure the particles processor distribution is different than the uniform grid distribution and particles need to be scattered from their previous owner processor to their new owner. In practice, we first interpolate on the grid and then send the data to the appropriate processor. After performing the IFFT and the Ewald sum, the velocities at the grid points need to be interpolated back to the particles center location in a parallel manner as well.	122
5.6	FFT parallelization: (1) 2D serial FFTs are performed on the original data layout slab by slab, where each slab belongs fully and only to one processor (2) transpose, i.e communicate the data (3) 1D serial FFTs on transposed data, pencil by pencil, where each pencil belongs fully to one and only processor. (4) The data is transposed back to its original form and in is the Fourier space.	122

5.7	These graphs compare physical observables between a validated legacy Fortran serial code and our recently developed parallel code. On the left, high frequency viscosity as a function of volume fraction computed in the absence of Brownian motion and a constant shear such as $Pe = 1$: the parallel code uses 128 processors for $N_p = 10,000$ particles. On the middle, equilibrium osmotic pressure as a function of volume fraction using ASDB (2,000 particles with 16 processors) and ASDB-nf (10,000 particles with 128 processors) in the absence of shear such as $Pe = 0$. On the right non-equilibrium osmotic pressure as a function of Peclet number with ASDB (1,000 particles with 16 processors).	132
5.8	Strong scaling of one ASD step on Stampede1 with $\phi = 0.2$, an inter particle force with a Morse potential of strength $V_0 = 5$ and Brownian motion with ASDB-nf. On the left is described the scaling for different number of processors	135
5.9	Speed up for different grid topologies for $N_p = 102, 400, N_x = 256$	135
5.10	Strong scaling of one ASD step on Stampede1 with $\phi = 0.2$, an inter particle force with a Morse potential of strength $V_0 = 5$ and Brownian motion with ASDB-nf.	138
5.11	In the left, the residual obtained as function of the number of iterations during the near-field inversion. In the middle and left the number of iterations required to invert the ASD linear system as function of the number of particles and as function of the concentration (values are normalized s.t first value is one). The parameters are: (a) $\phi = 0.2, N = 102, 400$; (b) $\phi = 0.2$; (c) $N = 102, 400$ and an inter particle force with $V_0 = 5$ in all cases and Brownian force.	139
5.12	Scaling of a shear simulation with the number of processors. In a shear simulation the box is typically sheared until it reaches an angle of $\pi/4$. At this point the box returns to its original form and the shear component is removed from the particles position and the simulation continues from there. On a parallelization perspective, it means that particles will probably migrate by a distance higher than one processor. An algorithm based on neighbor communication only can not remedy to it. Instead each time that the box transits from $\gamma = \pi/4$ to $\gamma = 0$, an all-to-all communication between all the processors occurs. The parameters are $\phi = 0.18, N = 640, 000, Pe = 1, N_x = 512$ and no Brownian force and no inter particle force	141
5.13	Gelation of a hydrodynamically-interacting colloidal suspension under quiescent conditions at $t=0, 0.1, 2, 4, 16, 24, 32, 64, 100$ Brownian times. The time is non-dimensional as it is scaled by a^2/D . These pictures depict the colloids self-assembly dynamics as they form complex bi-continuous space-spanning structures within the fluid. Buried particles (blue) might be in glassy arrest (as shown in [149]) and surface particles (red) are expected to be more mobile. The parameters utilized for the parallel ASD method under quiescent conditions are: $N = 102, 400, N_x = 256$ a Brownian force with ASDB-nf and an inter particle force.	142

CHAPTER 1

BACKGROUND

1.1 Overview of many-body hydrodynamic interactions

Complex fluids comprise a broad class of materials, including everyday examples such as ketchup, paint, and personal care products as well as more exotic complex fluids such as the interior of living cells, pharmaceutical preparations, and liquid crystals. What sets them apart from simple Newtonian fluids is the dependence of their rheological behavior on flow. This difference arises from the presence of a secondary, non-continuum phase that gives the fluid a microscopic structure. Asymmetric distortion and relaxation of this microstructure produces well-known non-Newtonian rheology, such as shear-thinning and thickening [10, 143], viscoelasticity [115], normal stress differences [62], and flow-induced diffusion [60], among others. Underlying these important macroscopic phenomena are microscopic colloidal-scale forces, such as hydrodynamic, interparticle and thermodynamic forces, which depends on the particle configurations. Rheological studies focus on explaining micro-scale flow behavior via detailed micro-mechanics of constituent particles.

Pair level hydrodynamic interactions can qualitatively explain some of the rheological behaviors mentioned above. In a dilute suspension, since particles are relatively far from each other, it can be assumed that one particle can only see and interact with one particle nearby. The suspension is too dilute to have a third particle interacting with the pair. Thus only pair-level hydrodynamic interactions need to be considered. By directly solving the Stokes equation in the scenario of only a pair of particles suspended in the solvent, Jeffrey and Onishi,

and other scholars [1, 83, 84, 88, 89] worked out analytical solutions to describe pair-level hydrodynamic interactions. Furthermore, to study rheology of dilute suspensions of many particles, one can numerically solve Smoluchowski equation [142] based on the analytical solution for the pair interactions.

But many practical problems involve concentrated suspensions, where three-body or higher-order particle interactions become non-negligible. Such interactions produce more complex secondary flows and alter microstructural evolution that qualitatively changes macroscopic flow behavior. Accelerated[133] Stokesian Dynamics[28, 55] (ASD) is one approach for simulating many-body hydrodynamic interactions in suspensions of particles undergoing low-Reynolds number flow. In Stokesian Dynamics, pairwise hydrodynamic interactions among all the particles are first evaluated by applying the multipole expansion and truncating the expansion terms at the first force moment, and represented as a mobility matrix. Durlofsky et al. [55] proved that inverse of this mobility matrix gives rise to a true approximation of many-body hydrodynamic interactions. This approximated many-body interaction is the so-called “far-field” interactions. However, to involve the short-range interactions of closely spaced particles (and lubrication forces) requires infinite expansion of the pairwise interactions which is not realistic. Thus an analytical solution of pair-level interactions from Jeffrey and Onishi [84], Jeffrey [83] is involved as the near-field portion to handle the short-range interactions. Finally the Stokesian Dynamics computes many-body hydrodynamic interactions by adding far-field and near-field interactions together.

The foundation of ASD simulation is to create true particle configurations. This is done by solving the Langevin equation [96] to obtain the trajectories of

individual particles as they interact with one another and are carried along by flow. The interactions are set in part by relative particle positions. Integration of the Langevin equation in the inertialess or over-damped limit produces particle displacements that can then be utilized to determine new configuration-dependent coupling tensors, and repeated integrations produce an evolution of particle positions over time. Many such solution realizations leads to Markovian statistics for mean and mean-square displacements. The same physics obtained by this conservation of momentum approach are recovered via theoretical approaches such as solving the Smoluchowski equation, which enforces conservation of probability. This leads to an advection-diffusion type equation that can be solved analytically or at least numerically, to yield the stochastic distribution of particles in space and time, which can then be utilized as a weighting function for average velocity, stress, osmotic pressure, and viscosity. In this dissertation we present a bridge between these two approaches: a method to analytically study concentrated suspensions by representing the interaction between any particle pair as interacting across a microstructured intervening medium comprised of solvent and other particles. Thus the analytical framework can be utilized to study concentrated suspensions. The crucial part of this idea is to obtain the pair interactions between the medium. In Chapter 2 and 3, we utilize ASD simulations to extract effective concentrated pair mobilities. These functions are shown to be able to treat many-body hydrodynamic interactions as pair interactions and thus directly obtain the rheology in concentrated suspensions by solving Smoluchowski equation. In addition, the concentrated mobility functions of couplings between forces and particle motion show a $1/r$ decay for any arbitrary concentration. It clearly shows that hydrodynamic interactions are not screened. Thus for suspensions of freely diffusing spheres,

the hydrodynamic interactions cannot be truncated in analytical or numerical studies.

In this dissertation, the idea of bridging dilute theory to concentrated suspensions is tested by applying it to the case of active microrheology. In active microrheology, a spherical Brownian probe is actively driven by an externally applied force through a suspension, and changes in its velocity are related constitutively to the viscosity and osmotic pressure of the surrounding medium. This powerful technique enables the rheological interrogation of microscopically small systems such as the interior of biological cells and vesicles. It thus provides an important complement to macroscopic shear rheology. However, most such small scale systems are concentrated, and active microrheology theory thus far is limited to an assumption of diluteness, owing to the difficulty of closing three-body and higher order integrals. In Chapter 4, we present the results for viscosity and stress under strong microrheology flows, measured directly in concentrated suspensions by dynamic simulation. This is then compared to dilute theory that is scaled up utilizing our new concentrated mobility functions, showing excellent promise for this approach. This work is represented in Chapter 4.

Dynamic simulation of concentrated colloidal suspensions is indispensable for understanding complex fluids, and great strides forward in computational algorithm efficiency in the last two decades have enabled simulation of larger and larger systems, but serious limitations still exist. This limitation is present in all methods for simulating low-Reynolds number particle-laden flows, most dramatically when Brownian motion is modeled. The Reynolds number, Re , is the dimensionless strength of flow inertia relative to viscous stress, $Re = \rho UL/\eta$,

where ρ is the fluid density, η is the fluid viscosity, U is the characteristic speed of the flow, and L is the characteristic length scale such as channel width, particle size, or a surface dimension. In the case of the Stokesian dynamics algorithm, even the fastest approach, ASD, has thus far been serial, limiting system size to a few thousand particles. This capacity cannot satisfy the study of more complex non-homogenous colloidal suspensions, e.g., colloidal gels and glasses require 100,000 to 1,000,000 particles to sample a statistically representative set of network structures. We have developed parallel algorithms based on Accelerated Stokesian Dynamics, combining the massively parallel architecture with the matrix operations required to model many-body hydrodynamic interactions. This work is represented in Chapter 5.

1.2 Accelerated Stokesian Dynamics (ASD) algorithm

Accelerated[133] Stokesian Dynamics[28, 55] (ASD) is an algorithm that simulates the particle dynamics in colloidal suspensions in which many-body hydrodynamic interactions are important. This algorithm will be deeply utilized and improved in this thesis. Here, we provide a brief review of the algorithms of ASD simulation. We consider systems of N rigid particles of size a suspended in an incompressible Newtonian fluid of density ρ and viscosity η . The fluid motion is governed by the Navier-Stokes equations. The characteristic velocity U of particle motion sets the Reynolds number, $Re \equiv \rho U a / \eta$. Because the particles are small, $Re \ll 1$, inertial forces can be neglected and thus the fluid mechanics are governed by the Stokes equations.

In Stokes flow, the fluid velocity at any point is represented via a surface

integral [94],

$$\mathbf{u}(\mathbf{x}) = \mathbf{u}^\infty(\mathbf{x}) - \sum_{\alpha=1}^N \int_{S_\alpha} \mathbf{J}(\mathbf{x} - \mathbf{y}) \cdot \mathbf{f}(\mathbf{y}) dS_y, \quad (1.1)$$

where $\mathbf{u}(\mathbf{x})$ is the velocity at any field point \mathbf{x} , \mathbf{u}^∞ is any far-field imposed flow. The integral is via N particle surfaces, where for particle α the force density on its surface position \mathbf{y} is represented by $\mathbf{f}(\mathbf{y})$. The Green's function of Stokes equation, $\mathbf{J}(\mathbf{x} - \mathbf{y})$, is the well-known Stokeslet, given by

$$\mathbf{J}(\mathbf{r}) = \frac{1}{8\pi\eta a} \left(\frac{\mathbf{I}}{r} + \frac{\mathbf{r}\mathbf{r}}{r^3} \right), \quad (1.2)$$

where $\mathbf{r} = \mathbf{x} - \mathbf{y}$ and $r = \|\mathbf{r}\|$. Equation 1.1 can be expanded in moments about the center of particle α as

$$\begin{aligned} \mathbf{u}(\mathbf{x}) - \mathbf{u}^\infty(\mathbf{x}) = & - \left(1 + \frac{a^2}{6} \nabla^2 \right) \mathbf{J}(\mathbf{x} - \mathbf{y}) \cdot \mathbf{F}_\alpha^H - \frac{1}{2} (\nabla \times \mathbf{J}(\mathbf{x} - \mathbf{y})) \cdot \mathbf{L}_\alpha^H \\ & - \left(1 + \frac{a^2}{10} \nabla^2 \right) [\nabla \mathbf{J}(\mathbf{x} - \mathbf{y}) + (\nabla \mathbf{J}(\mathbf{x} - \mathbf{y}))^T] : \mathbf{S}_\alpha^H + \dots, \end{aligned} \quad (1.3)$$

where \mathbf{F}^H and \mathbf{L}^H represents the hydrodynamic force and torque. The stresslet \mathbf{S}^H is the symmetric part of the first moment of the hydrodynamic surface traction. We define a disturbance flow imposed by all other particles except particle α as $\delta\mathbf{u} = \mathbf{u} - \mathbf{u}^\infty$. The motion of particle α arising from this disturbance flow $\delta\mathbf{u}$ at the center of particle α is evaluated by Faxen's formulae,

$$\mathbf{U}_\alpha - \mathbf{u}^\infty(\mathbf{x}_\alpha) = \frac{\mathbf{F}_\alpha^H}{6\pi\eta a_\alpha} + \left(1 + \frac{a_\alpha^2}{6} \nabla^2 \right) \delta\mathbf{u}(\mathbf{x}_\alpha), \quad (1.4)$$

$$\boldsymbol{\Omega}_\alpha - \boldsymbol{\omega}^\infty(\mathbf{x}_\alpha) = \frac{\mathbf{L}_\alpha^H}{8\pi\eta a_\alpha^3} + \frac{1}{2} \nabla \times \delta\mathbf{u}(\mathbf{x}_\alpha), \quad (1.5)$$

$$-\mathbf{E}^\infty = \frac{\mathbf{S}_\alpha^H}{\frac{20}{3}\pi\eta a_\alpha^3} + \left(1 + \frac{a_\alpha^2}{10} \nabla^2 \right) \delta\mathbf{E}(\mathbf{x}_\alpha), \quad (1.6)$$

where \mathbf{U}_α , $\boldsymbol{\Omega}_\alpha$ and \mathbf{E}_α are the translational, rotational, and straining motion of particle α . For rigid particles, $\mathbf{E}_\alpha \equiv 0$. The disturbance rate of strain, $\delta\mathbf{E}$, is given by

$$\delta\mathbf{E} = \frac{1}{2} (\nabla(\delta\mathbf{u}) + [\nabla(\delta\mathbf{u})]^T). \quad (1.7)$$

Applying the Faxen's formulae into Equation 1.3 gives rise to a linear coupling between traction moments and particle motion,

$$\begin{bmatrix} \mathbf{U} - \mathbf{u}^\infty \\ \boldsymbol{\Omega} - \boldsymbol{\omega}^\infty \\ -\mathbf{E}^\infty \end{bmatrix} = -\mathcal{M} \cdot \begin{bmatrix} \mathbf{F}^H \\ \mathbf{L}^H \\ \mathbf{S}^H \end{bmatrix}. \quad (1.8)$$

The grand mobility matrix \mathcal{M} is the coupling tensor, which can be written in detail as

$$\mathcal{M} = \begin{bmatrix} \mathbf{M}^{UF} & \mathbf{M}^{UL} & \mathbf{M}^{US} & \dots \\ \mathbf{M}^{\Omega F} & \mathbf{M}^{\Omega L} & \mathbf{M}^{\Omega S} & \dots \\ \mathbf{M}^{EF} & \mathbf{M}^{EL} & \mathbf{M}^{ES} & \dots \\ \vdots & \vdots & \vdots & \ddots \end{bmatrix} \quad (1.9)$$

The superscript represents the specific couplings between velocity derivatives and force traction. Since it is not possible to keep an infinite number of terms in the multipole expansion in Equation 1.3, one must judiciously truncate it. Removal of higher-order terms simply means that the resultant approximation is accurate for wider particle spacings. We truncate at the stresslet, i.e. we retain the hydrodynamic force, torque, and stresslet in the approximated mobility matrix, \mathcal{M}^∞ , to give an accurate estimation of far-field hydrodynamic interactions. The near-field interactions lost by such an approximation are simply superimposed linearly utilizing the analytical expressions for mobility functions derived by Jeffrey and Onishi [84], Jeffrey [83]. This is a central approach of the Stokesian Dynamics algorithm [28, 55]. Meanwhile, the disturbance flow evaluated at the center of every particle comes from the pairwise addition, thus \mathcal{M}^∞ is a pair-level expression. To transform it to a many-body linearity expression, one must invert the grand mobility matrix to obtain the couplings for all particles to one another for an infinitude of reflections among them [55]. For particles close to each other, the near-field and lubrication interactions must be added. Thus

the hydrodynamic couplings among particles is written as

$$\mathcal{R} = (\mathcal{M}^\infty)^{-1} + \mathcal{R}_{nf}, \quad (1.10)$$

where $\mathcal{R} = \mathcal{M}^{-1}$ is the grand resistance tensor, represents the hydrodynamic couplings between traction moments and velocity derivatives of particles. The inverse of the truncated grand mobility matrix, $(\mathcal{M}^\infty)^{-1}$, captures the infinitude of reflections between all particles, thus is an approximation of many-body far-field hydrodynamic interactions. The near-field interactions are represented by the two-body resistance matrix, \mathcal{R}_{nf} , which is evaluated directly from theoretical solutions [84, 83, 85]. Plugging Equation 1.10 into Equation 1.8, we get

$$\begin{bmatrix} \mathbf{F}^H \\ \mathbf{S}^H \end{bmatrix} = -(\mathcal{R}_{nf} + (\mathcal{M}^\infty)^{-1}) \cdot \begin{bmatrix} \mathbf{U} - \mathbf{u}^\infty \\ -\mathbf{E}^\infty \end{bmatrix}. \quad (1.11)$$

Here for convenience, we merge force and torque together, denote as \mathbf{F}^H , and translational and rotational velocity together, as \mathbf{U} .

Equation 1.11 describes a linearity statement of hydrodynamic couplings for N particles suspended in the fluid. The $6N$ vector \mathbf{U} gives the velocity of all N particles arising from an imposed linear flow and from disturbance flows arising from infinitely coupled hydrodynamic interactions between all the particles. However, non-hydrodynamic microscopic forces, such as entropic or enthalpic forces, also influence particle motion. Brownian motion plays an important role in suspension mechanics of colloids. In dynamic simulation we can model the particle behavior arising from this stochastic force and other non-hydrodynamic forces utilizing the Langevin equation:

$$m \frac{d\mathbf{U}}{dt} = \mathbf{F}^H + \mathbf{F}^B + \mathbf{F}^P + \mathbf{F}^O, \quad (1.12)$$

where the left hand side of the equation denotes the inertia, \mathbf{F}^H , \mathbf{F}^B , \mathbf{F}^P , and \mathbf{F}^O

denotes the hydrodynamic, Brownian, interparticle, and all other microscopic forces respectively.

The stochastic Brownian force turns the Langevin equation to a stochastic differential equation (SDE), while the other forces are deterministic. To solve this SDE, we split the inertial term into a Brownian induced term and a non-Brownian induced term, i.e., $m\mathbf{d}\mathbf{U}/dt = m\mathbf{d}(\mathbf{U}^B + \mathbf{U}^{other})/dt$. Since the hydrodynamic force is coupled linearly with particle motion, i.e., $\mathbf{F}^H = -\mathbf{R}_{FU} \cdot \mathbf{U} = -\mathbf{R}_{FU} \cdot (\mathbf{U}^B + \mathbf{U}^{other})$, Equation 1.12 can be split into one with only deterministic contributions (1.13), and the other portion with only stochastic force (1.14):

$$m \frac{d\mathbf{U}^{other}}{dt} = -\mathbf{R}_{FU} \cdot \mathbf{U}^{other} + \mathbf{F}^P + \mathbf{F}^O, \quad (1.13)$$

$$m \frac{d\mathbf{U}^B}{dt} = -\mathbf{R}_{FU} \cdot \mathbf{U}^B + \mathbf{F}^B. \quad (1.14)$$

Solving Equation 1.13 directly results in a particle displacement physically arising from the hydrodynamic couplings between particle motion and non-Brownian forces, while the displacement arising from inertia vanishes when the integrating time step Δt is larger than the inertial relaxation time, $m/6\pi\eta a$ (smaller than the time scale for configuration change to assume that the hydrodynamic coupling matrix remains the same). The numerical results for solving this equation reads:

$$\Delta\mathbf{x}^{other} = \mathbf{R}_{FU}^{-1}(\mathbf{x}(t)) \cdot (\mathbf{F}^P(\mathbf{x}(t)) + \mathbf{F}^O(\mathbf{x}(t)))\Delta t. \quad (1.15)$$

Equation 1.14 is a stochastic differential equation, where the Brownian force \mathbf{F}^B is a random Gaussian deviate, which satisfies

$$\langle \mathbf{F}^B \rangle = 0, \quad (1.16)$$

$$\langle \mathbf{F}^B(0)\mathbf{F}^B(t) \rangle = 2\mathbf{R}_{FU}\delta(t), \quad (1.17)$$

where $\langle \cdot \rangle$ represents an ensemble average over the thermal fluctuations in the fluid, and δ is the delta function. By integrating Equation 1.14 twice with the same time scale as in Equation 1.13, the displacement from Brownian contribution reads:

$$\Delta \mathbf{x}^B = \sqrt{2} \mathbf{R}_{FU}^{-1/2}(\mathbf{x}(t)) \cdot \Delta \mathbf{w} + 2 \mathbf{R}_{FU}^{-1/2}(\mathbf{x}(t)) \cdot (\nabla \cdot \mathbf{R}_{FU}^{-1/2}(\mathbf{x}(t))) \Delta t, \quad (1.18)$$

where $\Delta \mathbf{w}$ is the Wiener process. The first term on the right hand side of the equation is the Brownian displacement present in the Euler-Mayurma scheme. The last term is the Brownian drift, which improves the convergence from $(\Delta t)^{0.5}$ to $(\Delta t)^1$. Finally, by combining the displacement arising from Equation 1.15 and 1.18, the Langevin equation is solved and the particle displacement is obtained.

After demonstrating the integral scheme in ASD, we now discuss how to incorporate the non-hydrodynamic forces into the linearity statement of hydrodynamic coupling (Equation 1.11) and evaluate the stresslet. We define a far-field hydrodynamic force, \mathbf{F}_{ff}^H , and a far-field hydrodynamic stresslet, \mathbf{S}_{ff}^H , which satisfy

$$\begin{bmatrix} \mathbf{F}_{ff}^H \\ \mathbf{S}_{ff}^H \end{bmatrix} = -(\mathcal{M}^\infty)^{-1} \cdot \begin{bmatrix} \mathbf{U}^H - \mathbf{u}^\infty \\ -\mathbf{E}^\infty \end{bmatrix}, \quad (1.19)$$

where \mathbf{U}^H represents the motion arising from the imposed flow. The near-field resistance matrix, \mathcal{R}_{nf} can be further expressed blockwise according to different couplings,

$$\mathcal{R}_{nf} = \begin{bmatrix} \mathbf{R}_{nf}^{FU} & \mathbf{R}_{nf}^{FE} \\ \mathbf{R}_{nf}^{SU} & \mathbf{R}_{nf}^{SE} \end{bmatrix} \quad (1.20)$$

Then the particle motion arising from hydrodynamic interactions is expressed as

$$\mathbf{U}^H = \mathbf{R}_{nf}^{FU-1} \cdot (\mathbf{F}_{ff}^H + \mathbf{R}_{nf}^{FE} : \mathbf{E}^\infty). \quad (1.21)$$

The far-field hydrodynamic force and stresslet are solved via the following linear system,

$$\begin{aligned} & \left(\mathbf{M}^\infty + \begin{bmatrix} \tilde{\mathbf{R}}_{nf}^{FU-1} & \mathbf{0} \\ \mathbf{0} & \mathbf{0} \end{bmatrix} - \beta \mathbf{M}^\infty \cdot \begin{bmatrix} \tilde{\mathbf{R}}_{nf}^{FU-1} & \mathbf{0} \\ \mathbf{0} & \mathbf{0} \end{bmatrix} \right) \cdot \begin{bmatrix} \tilde{\mathbf{F}}_{ff}^H \\ \mathbf{S}_{ff}^H \end{bmatrix} \\ &= - \begin{bmatrix} \tilde{\mathbf{R}}_{nf}^{FU-1} \cdot \mathbf{R}_{nf}^{FE} : \mathbf{E}^\infty \\ -\mathbf{E}^\infty \end{bmatrix} + \beta \mathbf{M}^\infty \cdot \begin{bmatrix} \tilde{\mathbf{R}}_{nf}^{FU-1} \cdot \mathbf{R}_{nf}^{FE} : \mathbf{E}^\infty \\ \mathbf{0} \end{bmatrix}. \end{aligned} \quad (1.22)$$

Here, $\tilde{\mathbf{R}}_{nf}^{FU} = \mathbf{R}_{nf}^{FU} + \beta \mathbf{I}$, and $\tilde{\mathbf{F}}_{ff}^H = \mathbf{F}_{ff}^H + \beta \mathbf{U}^H$, and β is a positive number. Such transformation arises from the non-positive definite behavior of the near-field resistance matrix \mathbf{R}_{nf}^{FU} . To facilitate the inverse operation of this matrix, a positive value, β , is added manually onto its diagonal components to make it positive definite. Thus, the particle motion arising from imposed flow is expressed as

$$\mathbf{U}^H = \tilde{\mathbf{R}}_{nf}^{FU-1} \cdot (\tilde{\mathbf{F}}_{ff}^H + \mathbf{R}_{nf}^{FE} : \mathbf{E}^\infty). \quad (1.23)$$

To evaluate the particle motion arising from the Brownian force, the challenge is to generate Gaussian variates of the form $\psi = \mathbf{R}_{FU}^{-1/2}(\mathbf{x}(t))\Delta\mathbf{w}$. The Brownian force must be obtained first to evaluate Brownian velocity and displacement. Since the resistance tensor is expressed as an addition of near-field resistance and the inverse of far-field mobility, the Brownian force is also separated into a near-field portion and a far-field portion to simulate respectively,

$$\mathbf{F}^B = \mathbf{F}_{nf}^B + \mathbf{F}_{ff}^B. \quad (1.24)$$

We define the near-field and far-field Brownian force as follows:

$$\langle \mathbf{F}_{nf}^B \rangle = \langle \mathbf{F}_{ff}^B \rangle = 0, \quad (1.25)$$

$$\langle \mathbf{F}_{ff}^B \mathbf{F}_{ff}^B \rangle = 2(\mathbf{M}_{UF}^\infty)^{-1}/\Delta t, \quad (1.26)$$

$$\langle \mathbf{F}_{nf}^B \mathbf{F}_{nf}^B \rangle = 2\mathbf{R}_{nf}^{FU} / \Delta t, \quad (1.27)$$

and the covariance between \mathbf{F}_{nf}^B and \mathbf{F}_{ff}^B is zero. The detailed simulation method to generate the Brownian forces will be discussed in Chapter 5. With the Brownian forces, a linearity statement similarly to Equation 1.11 is constructed and the motion due to Brownian force is solved from the linear system.

1.3 Non-Newtonian rheology with many-body hydrodynamic interactions

The Stokes or ‘creeping flow’ equations have the nature of fore-aft symmetry and time reversibility. These two behaviors are well-known and have been proved theoretically for dilute suspension in simple-shear flow [16]. The streamline shows two parts: within a critical boundary closed trajectories form, thus particles inside the boundary cannot escape from this region; particles outside the boundary stay in the region of open streamlines and cannot go inside. In this case of two particles with pure hydrodynamic interactions, this microstructure implies the Newtonian behaviors, i.e., isotropic microstructure, zero normal stress differences and no osmotic pressure. When we say particle suspensions with purely hydrodynamic interactions, we consider the situation of no Brownian motion and smooth spheres. It is expected in concentrated suspensions with only many-body hydrodynamic interactions, such behaviors hold since the governing equations are still Stokes’ equations. Brownian motion, particle roughness and polydispersity can all introduce perturbations to the particle trajectories and destroy both the fore-aft symmetry and time reversibility of the Stokes flow, lead to anisotropic microstructure, and thus pro-

duce non-Newtonian behaviors. However, many experiments [66] and simulations [125] show contradictory results with the theoretical prediction where even at large enough Pe that Brownian motion is negligible, the microstructure is still anisotropic. This conflict arises from the chaotic nature of hydrodynamic interactions. Jánosi et al. [82] analytically solved the sedimentation of three particles in Stokes flow and found the particle motions are extremely sensitive to initial configurations. They found that the particle trajectories separate exponentially in time with a positive Lyapunov exponent, which clearly illustrates the chaotic nature of hydrodynamic interactions. Furthermore, Marchioro and Acrivos [111] and Drazer et al. [53] proved that in simple shear flow, though the equation system is deterministic, particle trajectories are stochastic and chaotic. Pine et al. [126] measured the diffusivity of non-colloidal particles in an oscillatory shear flow with both experiments and simulations. They found there exists a threshold as the magnitude of the shear rate to distinguish reversibility of particle trajectories and chaotic behaviors. In particular, higher concentration facilitates a smaller shear rate required to introduce chaos. This gives a clear clue of the role of many-body hydrodynamic interactions in non-Newtonian behaviors. Many-body hydrodynamic behaviors are significant at higher concentrations and thus give rise to more sensitivity to perturbation factors such as Brownian motion, machine error, particle roughness and polydispersity. In general, three- and many-body hydrodynamic interactions lead to non-Newtonian behaviors by combining with non-hydrodynamic interactions among particle suspensions. Theoretically the nature of fore-aft symmetry and time reversibility of Stokes equation indicates that hydrodynamic interactions lead to Newtonian behaviors. However, its chaotic nature can give rise to the non-Newtonian rheologies. Stronger many-body hydrodynamic interactions make particles more

sensitive to the small perturbations from e.g., non-hydrodynamic interactions, trajectories unpredictable, and thus produce more pronounced non-Newtonian behaviors.

CHAPTER 2

**PAIR MOBILITY FUNCTIONS FOR RIGID SPHERES IN
CONCENTRATED COLLOIDAL DISPERSIONS: FORCE, TORQUE,
TRANSLATION, AND ROTATION**

2.1 Introduction

Complex fluids span an extraordinary range of materials: macromolecular solutions, hydrogels, paint, foodstuffs, colloidal glasses, and more. Common to all of these materials is a two-phase structure comprising a collection of microscopic domains embedded in a suspending solvent. These microscopic domains form a microstructure whose presence and shape alters the mechanical properties and flow behavior of such fluids. Einstein's first-order correction to the viscosity for a dilute suspension of hard spheres at infinite dilution[56] was one of the earliest models for the influence of suspended materials on flow behavior. Batchelor later extended this work to account for the role played by thermodynamic and hydrodynamic interactions in the diffusion and rheology of semi-dilute colloidal dispersions, deriving analytical solutions for settling rate, the short- and long-time self-diffusion coefficients, as well as the shear viscosity [16, 13, 15], among others. Batchelor's expansion of hydrodynamic functions gave the first estimates for the hydrodynamic coupling between the motion of one particle to forces exerted on another. Subsequent work by Jeffrey and Onishi [84], Kim and Karrila [88] and Jeffrey [83] produced exact analytical expressions for these functions in a well-ordered set of reflected interactions between a pair of particles moving in Stokes flow. These mobility functions have enabled the solution of many fundamental problems in suspension dy-

namics, including hydrodynamic diffusion, polydisperse sedimentation, high-frequency linear viscoelasticity [104], shear thinning [13, 24], and shear thickening [28, 11, 51, 22, 110, 24]. Direct extension of these theories to concentrated systems is difficult, however, owing to the long-range nature of hydrodynamic disturbance flows which produces many-body interactions that are notoriously difficult to model analytically.

Calculations of the properties of concentrated suspensions have been attempted via numerous theoretical approaches, including scaling approximation[27], direct accounting for many-body interactions [21, 20, 58, 59, 42], closure approximations [104, 105, 106, 118, 119], kinetic models [129, 43, 50], mode-coupling approximations [76, 71, 46, 64, 67, 7, 116], and others [140]. Some yield excellent predictions of material properties for concentrated suspensions at equilibrium, but many rely on *ad hoc* approximations. Lionberger and Russel [104] compared several mean-field approaches in their study of the high-frequency elastic modulus, all of which assume a near-field lubrication form of the mobility combined with a mean far-field value. Their success in reproducing both the divergent and plateau behaviors of the high-frequency elastic modulus emerged from their observation that such approximations must vary smoothly from near-contact to the far-field, to recover the latter behavior. Once the transition is made smooth, the far-field approximation of a mean value was quite accurate in capturing the concentration dependence of near-equilibrium properties. While qualitatively accurate for weak departures from equilibrium, e.g., the long-time self-diffusion and zero-shear viscosity, such approximations consistently under-predict the concentration-dependence.[106] Such behavior is not surprising, as any screening of hydrodynamic interactions leads to a reduction in viscous dissipation: particles move faster on average in such models. In response to these diffi-

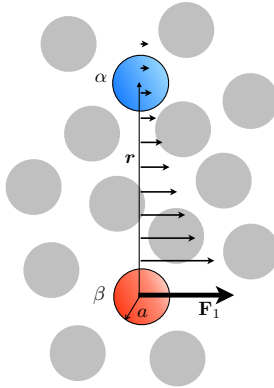


Figure 2.1: Model system of identically sized colloidal hard spheres, with test particles α and β at separation r . A force F_1 exerted on particle β produces a fluid disturbance that decays as $1/r$, entraining fluid and nearby particles. From [150], with permission.

culties, several models for the evolution of particulate suspensions that neglect many-body hydrodynamics have been proposed, e.g., mode-coupling theory [65], based on a variety of physical justifications.

In contrast to models that assume screening of long-range hydrodynamics, the theory of low-Reynolds number hydrodynamics suggests that such screening is not an appropriate approximation in suspensions of force-free particles: mobile translating particles entrain fluid and other particles with a strength that decays as $1/r$, where r is the separation between an interacting pair (figure 2.1). That is, the particle mobility allows the fluid to remain force free, assuring that the fluid mechanics are governed by the Stokes equations, rather than by Brinkman-like[33] flow. Indeed, some predictive theories for the rheological behavior of complex fluids are built upon the inclusion of long-range interactions. In dual-probe microrheology for example, the Brownian motion of a pair of tracer particles embedded in a complex fluid is tracked in order to infer bulk properties of the material. This approach employs a phenomenological extension of the Stokes-Einstein relation that capitalizes on long-

range, $1/r$ hydrodynamic coupling between the tracers to probe the intervening medium.[45, 100, 101, 102]

Thus there exist well-known theoretical models for the physical interactions between particles in freely diffusing concentrated suspensions that utilize widely variant and fundamentally different approaches: in one perspective, long-range hydrodynamics are assumed to be screened completely by crowding, and are neglected entirely [65]; in another, screening is applied but in a less severe manner, where a transition from near-contact lubrication gives way to long-range average mobility that approximates many-body coupling [104, 106, 118, 119]; and in yet another, inclusion of long-range many-body hydrodynamics forms the very basis of the theory [45, 100, 101, 102]. However, until now no systematic study has been carried out to test these implied assumptions that hydrodynamics are screened to some extent.

Dynamic simulation has proven an important complement to theory, and has been extremely successful in capturing the equilibrium and non-equilibrium rheological behavior of concentrated colloidal suspensions [28, 55, 62, 61, 27, 29, 124, 133, 8, 137, 148]. Included in these investigations was the study by Durlofsky and Brady [54] of the propagator of fluid disturbances around fixed arrays of particles. The goal of their study was to utilize simulation to determine the Green's function propagator of flow through a fixed array of particles and compare it to the corresponding Brinkman propagator and, in so doing, determine if fixed arrays of particles screen hydrodynamic interactions as occurs in porous media. Their results indicate that indeed such screening does occur, which is expected: fixed particles exert a force on the fluid, and the resulting forced flow is not governed by Stokes equations but rather by a

Brinkman equation. Momentum is dissipated more rapidly over distance, with a decay scaling as $1/r^3$. When particles are free to diffuse, the fluid is force free and its motion governed by Stokes equations, with fluid disturbances that decay slowly, as $1/r$. The idea that crowding (i.e. high concentration) somehow leads to screening behavior has somehow emerged. In essence, the property of hydrodynamic screening present in arrays of fixed particles is conferred to concentrated suspensions of freely diffusing (mobile) particles, justified by the concentration-driven reduction of self-mobility. While providing some degree of success in equilibrium problems, this idea has not been rigorously tested until now.

In the present study we address the question of whether reduction in particle self-mobility due to crowding in concentrated suspensions can be extrapolated to pair interactions and thus effectively screens out long-range hydrodynamic coupling between particles and, if so, over what range this takes place. To this end, our primary goal is to develop mobility functions for the many-body hydrodynamic coupling between pairs of colloidal particles diffusing through a suspension at arbitrary concentration. These functions can serve as an extension of their well-known counterparts for a pair of spheres interacting through a Newtonian solvent, where now the particles interact through an intervening medium. To model this behavior, we study the motion of two colloidal particles immersed in and interacting in a suspension of freely diffusing particles.

The remainder of this chapter is organized as follows. In section 2.2 we briefly review the mobility tensors that couple particle motion to force and torque. In section 2.3, we develop the computational approach utilized to obtain the mobility functions giving particle translation and rotation resulting from im-

posed forces and torques. Accelerated Stokesian Dynamics Simulations are employed to calculate the self, pair, and relative mobility of the particles, in terms of functions describing the motions along and transverse to a line of centers between a particle pair. Care is taken to efficiently compute these quantities over a range of separations, thus capturing the strength of the hydrodynamic coupling over long distances in the suspension. In section 2.4, the results are presented for suspensions with volume fraction ranging from dilute to very concentrated. The hydrodynamic functions are compared to dilute theory and to the results of mean-field approaches. The study is concluded with a summary in section 2.5.

2.2 Hydrodynamic couplings

The most frequently utilized hydrodynamic coupling between a pair of particles is that which gives the velocity \mathbf{U}_α of a particle α due to a force \mathbf{F}_β exerted on a particle β , important for the calculation of *e.g.* translational diffusivity. An externally forced particle translating in Stokes flow propagates a disturbance that decays with distance from the particle, as $1/r$ (cf figure 2.1). A nearby particle will be entrained by this disturbance flow. The strength of the coupling between the force exerted on the first particle and that on another particle is the mobility $\mathbf{M}_{\alpha\beta}^{UF}$,

$$\mathbf{U}_\alpha = \mathbf{M}_{\alpha\beta}^{UF} \cdot \mathbf{F}_\beta, \quad (2.1)$$

where superscript *UF* refers to the velocity-force coupling. The mobility is a second-rank tensor that can be, for an isotropic suspension, expressed in terms of the isotropic unit tensor \mathbf{I} and the unit normal dyadic $\hat{\mathbf{r}}\hat{\mathbf{r}}$, where $\hat{\mathbf{r}} = \mathbf{r}/r$ and \mathbf{r} is the vector separation between a pair of particles. Projection of this tensor onto two orthogonal subspaces with projectors $\hat{\mathbf{r}}\hat{\mathbf{r}}$ and $(\mathbf{I} - \hat{\mathbf{r}}\hat{\mathbf{r}})$ gives the particle

velocity in response to a force acting along and transverse to the line of centers between a pair of particles, respectively:

$$\mathbf{M}_{\alpha\beta}^{UF} = \frac{1}{6\pi\eta a} [x_{\alpha\beta}^a(r)\hat{\mathbf{r}}\hat{\mathbf{r}} + y_{\alpha\beta}^a(r)(\mathbf{I} - \hat{\mathbf{r}}\hat{\mathbf{r}})]. \quad (2.2)$$

The coefficients $x_{\alpha\beta}^a(r)$ and $y_{\alpha\beta}^a(r)$ give the strength of the coupling in each direction, and the superscript A signifies the velocity-force coupling. For brevity we assume identical particles of size a although this restriction is easily relaxed.

As shown in equation 2.2, for pairs of particles $\alpha\beta$ immersed in a Newtonian solvent, the hydrodynamic functions depend only on the separation r between a particle pair. Jeffrey and Onishi [84] utilized the method of reflections and twin multipole expansions to develop exact analytical expressions for the force-velocity coupling in addition to torque-rotation, force-rotation, and torque-velocity couplings.

The aim of our method is to construct the elements of the corresponding mobility matrix that couple the motion of a pair of test particles, where the coupling between force and velocity is a function of both separation and of the concentration of the intervening and surrounding suspension. We thus consider the same two particles embedded in an isotropic suspension of identically sized particles with number density n . Because the suspending medium is isotropic and the fluid is force-free, the linear coupling between force and velocity still holds, but now the mobility functions also depend on the volume fraction $\phi = 4\pi a^3 n / 3$ of the intervening medium, giving

$$\mathbf{M}_{\alpha\beta}^{UF}(\phi) = \frac{1}{6\pi\eta a} [x_{\alpha\beta}^a(r; \phi)\hat{\mathbf{r}}\hat{\mathbf{r}} + y_{\alpha\beta}^a(r; \phi)(\mathbf{I} - \hat{\mathbf{r}}\hat{\mathbf{r}})]. \quad (2.3)$$

Evaluation of the hydrodynamic coupling between three or more particles requires a computational approach. For a suspension of N particles, the couplings

between a pair comprise motion due to all disturbance flows created by an infinitude of reflected interactions between all particles. For the velocity/force coupling,

$$\begin{pmatrix} \mathbf{U}_1 \\ \mathbf{U}_2 \\ \vdots \\ \mathbf{U}_N \end{pmatrix} = \begin{pmatrix} \mathbf{M}_{11}^{UF} & \mathbf{M}_{12}^{UF} & \cdots & \mathbf{M}_{1N}^{UF} \\ \mathbf{M}_{21}^{UF} & \mathbf{M}_{22}^{UF} & \cdots & \mathbf{M}_{2N}^{UF} \\ \vdots & \vdots & \ddots & \vdots \\ \mathbf{M}_{N1}^{UF} & \mathbf{M}_{N2}^{UF} & \cdots & \mathbf{M}_{NN}^{UF} \end{pmatrix} \cdot \begin{pmatrix} \mathbf{F}_1 \\ \mathbf{F}_2 \\ \vdots \\ \mathbf{F}_N \end{pmatrix}. \quad (2.4)$$

The diagonal elements of the particle mobility matrix are related to the translational short-time self-diffusivity as

$$\mathbf{D}_0^S(\phi) = kT\langle \mathbf{M}_{\alpha\alpha}^{UF}(\phi) \rangle, \quad (2.5)$$

where the angle brackets signify an ensemble average over many arrangements of particles. Such analysis is challenging owing to the long-range nature of disturbance flows generated by forced particles, as well as by the singular nature of lubrications forces when particles are close to contact. We discuss one well-known computational approach that resolves these issues next.

2.3 Computational approach

One approach that resolves the issues associated with singular lubrication and long-range hydrodynamic forces is the Stokesian dynamics algorithm [31, 55], where near-field and far-field hydrodynamics are computed separately. This approach is described in detail in the literature and so will not be reviewed here. Early realizations of this algorithm were of $O(N^3)$ computational complexity, where N is the number of particles in the simulation. This limited system

size to approximately 100 particles. More recently, Sierou and Brady [133] developed the Accelerated Stokesian Dynamics (ASD) algorithm which reduces the computational cost to $O(N \log N)$. Central to this efficiency is the avoidance of directly forming the mobility matrix \mathbf{M} . The information about the hydrodynamic couplings in \mathbf{M} remain encoded in particle motion and the hydrodynamic forces, however, and this information can be extracted utilizing a judicious choice of imposed forces.

Sierou and Brady computed the short-time concentration-dependent self-diffusion coefficient, a quantity frequently utilized in mean-field renormalization schemes for concentrated theory, from the trace of the average self-mobility: $\mathbf{D}_0^s = kT \text{tr}\langle \mathbf{M}^{UF} \rangle \mathbf{I}$, where kT is the thermal energy.[133] ASD is efficient in the computation of the velocity of a particle β due to a force on a particle α , $\mathbf{U}_\beta = \mathbf{M}_{\beta\alpha}^{UF} \cdot \mathbf{F}_\alpha$. To extract the diagonal elements of the mobility tensor, they selected for the perturbing force a random force \mathbf{F}^R with zero mean and identity covariance,

$$\overline{\mathbf{F}^R} = 0, \quad \overline{\mathbf{F}^R \mathbf{F}^R} = \mathbf{I}_{3N}, \quad (2.6)$$

where \mathbf{I}_{3N} is the 3N-dimensional identity tensor, and the overline signifies an average over realizations of the random force. The inner product of the velocity with the force can be written

$$\begin{aligned} \overline{\langle \mathbf{U} \cdot \mathbf{F}^R \rangle} &= \overline{\langle \mathbf{F}^R \mathbf{F}^R : \mathbf{M}^{UF} \rangle} \\ &= \overline{\langle \mathbf{I}_{3N} : \mathbf{M}^{UF} \rangle} \\ &= \text{tr} \langle \mathbf{M}^{UF} \rangle, \end{aligned} \quad (2.7)$$

where the angle brackets $\langle \cdot \rangle$ signify an average over many configurations of the particles. Because all particles are statistically identical, simply averaging the diagonal elements of each $\mathbf{M}_{\alpha\alpha}$ sub-matrix accounts for many configurations

surrounding a test particle. Only a few configurations are required to obtain an excellent statistical sampling. However, only the diagonal elements of the mobility tensor are extracted, resulting in a mean value of the self-mobility, with no information about particle entrainment or relative mobility.

In the current approach, we seek the pair mobility and ultimately the relative mobility. To begin, a suspension of N randomly distributed, equally sized hard spheres is placed in a simulation cell filled with an implicit solvent of viscosity η and density ρ . A force is exerted on a “test” particle, and its resulting motion disturbs the fluid; this disturbance is propagated throughout the domain, entraining all other particles with its motion. The perturbed particles move in response, thus generating their own disturbance flow, in turn leading to a reflected set of entrainment flows. These reflections are automatically captured in the ASD algorithm.

The dependence on radial separation of the coefficients $x^a(r; \phi)$ and $y^a(r; \phi)$ must be determined by placing the two test particles at a range of separations. We select one pair of particles at a time, at a given separation \mathbf{r} , and compute $\langle \mathbf{M}_{\alpha\beta}^{UF} \rangle_2$, where the subscript 2 indicates that the average is over many configurations of the other $N - 2$ particles. This procedure can be repeated for a range of separations to obtain the characteristics of the interaction through an effective medium as a function of radial separation. This approach, while effective, is computationally inefficient, most obviously due to the repeated computation over statistically equivalent configurations. In addition, computing the average over all configurations would give the pair diffusivity of each particle relative to any other particle, but would produce an isotropic tensor for each radial position. In many problems in the dynamics of suspensions, the longi-

tudinal and transverse couplings are of interest however, and this detail would be lost. This expense and loss of information can be avoided by recognizing that the longitudinal and transverse mobility coefficients (cf equation 2.3) can be measured directly.

For a given pair of particles $\beta \neq \alpha$, one can extract the longitudinal and transverse mobility couplings via the random sampling approach described above. For a given configuration of intervening particles, the longitudinal coupling for self-motion for an interacting pair separated by a distance r is given by

$$\begin{aligned} x_{11}^a &= \frac{1}{2} \hat{\mathbf{r}}_{\alpha\beta} \hat{\mathbf{r}}_{\alpha\beta} : (\mathbf{M}_{\alpha\alpha}^{UF} + \mathbf{M}_{\beta\beta}^{UF}) \\ &= \frac{1}{2} \hat{\mathbf{r}}_{\alpha\beta} \hat{\mathbf{r}}_{\alpha\beta} : (\mathbf{U}_\alpha \mathbf{F}_\alpha^R + \mathbf{U}_\beta \mathbf{F}_\beta^R) \\ &= \frac{1}{2} [(\mathbf{U}_\alpha \cdot \hat{\mathbf{r}}_{\alpha\beta})(\mathbf{F}_\alpha^R \cdot \hat{\mathbf{r}}_{\alpha\beta}) + (\mathbf{U}_\beta \cdot \hat{\mathbf{r}}_{\alpha\beta})(\mathbf{F}_\beta^R \cdot \hat{\mathbf{r}}_{\alpha\beta})], \end{aligned} \quad (2.8)$$

where $\mathbf{r}_{\alpha\beta} = \mathbf{x}_\alpha - \mathbf{x}_\beta$ and $\hat{\mathbf{r}}_{\alpha\beta} = \mathbf{r}_{\alpha\beta}/r$. Similarly,

$$x_{21}^a = \frac{1}{2} [(\mathbf{U}_\alpha \cdot \hat{\mathbf{r}}_{\alpha\beta})(\mathbf{F}_\beta^R \cdot \hat{\mathbf{r}}_{\alpha\beta}) + (\mathbf{U}_\beta \cdot \hat{\mathbf{r}}_{\alpha\beta})(\mathbf{F}_\alpha^R \cdot \hat{\mathbf{r}}_{\alpha\beta})]. \quad (2.9)$$

To obtain the transverse coefficients, a similar procedure to project onto $(\mathbf{I} - \hat{\mathbf{r}}_{\alpha\beta} \hat{\mathbf{r}}_{\alpha\beta})$ is employed:

$$\begin{aligned} y_{11}^a &= \frac{1}{4} (\mathbf{I} - \hat{\mathbf{r}}_{\alpha\beta} \hat{\mathbf{r}}_{\alpha\beta}) : (\mathbf{M}_{\alpha\alpha}^{UF} + \mathbf{M}_{\beta\beta}^{UF}) \\ &= \frac{1}{4} (\mathbf{I} - \hat{\mathbf{r}}_{\alpha\beta} \hat{\mathbf{r}}_{\alpha\beta}) : (\mathbf{U}_\alpha \mathbf{F}_\alpha^R + \mathbf{U}_\beta \mathbf{F}_\beta^R) \\ &= \frac{1}{4} (\mathbf{U}_\alpha \cdot \mathbf{F}_\alpha^R + \mathbf{U}_\beta \cdot \mathbf{F}_\beta^R - 2x_{11}^a) \end{aligned} \quad (2.10)$$

and

$$y_{21}^a = \frac{1}{4} (\mathbf{U}_\alpha \cdot \mathbf{F}_\beta^R + \mathbf{U}_\beta \cdot \mathbf{F}_\alpha^R - 2x_{21}^a). \quad (2.11)$$

The same procedure can be followed for the couplings between torque/rotation and force/rotation, and are given in the Appendix. This can be carried out

for any pair, and all pairs at a given separation are statistically equivalent. We average the coefficients for pairs within radial ‘bins’ within a width of $a/50$, and repeat this procedure for 30 configurations. Thus, averaging within a radial bin leverages the statistics available in one macroscopic particle configuration. After 30 particle configurations, the standard deviation ranged from 0.01 for $\phi = 0.05$ to 0.0001 for $\phi = 0.5$. We take into account pair separations only up to $r/a = 8$ as this recovers the relevant physics in the problem at a moderate computational cost. One can compare this length to the Brinkman screening length, where for a suspension at $\phi = 0.05$ is $\alpha \approx 3a$; this gets smaller as volume fraction increases. Stated alternatively, $8a$ is the Brinkman screening length in a suspension of volume fraction $\phi = 0.01$. Any screening effects produced by the periodicity of the domain appear at lengths scales that are three times larger than this value and thus do not contribute.

Other couplings between particle motion and surface tractions influence suspension dynamics, including that between torque and rotation. A torque exerted on one particle can cause it and other nearby particles to rotate, where the coupling is given by

$$\mathbf{M}_{\alpha\beta}^{\Omega L}(r, \phi) = \frac{1}{8\pi\eta a^3} [x_{\alpha\beta}^c(r; \phi)\hat{\mathbf{r}}\hat{\mathbf{r}} + y_{\alpha\beta}^c(r; \phi)(\mathbf{I} - \hat{\mathbf{r}}\hat{\mathbf{r}})]. \quad (2.12)$$

The coefficients $x_{\alpha\beta}^c$ and $y_{\alpha\beta}^c$ give the rotation of particle α due to a hydrodynamic torque on particle β , about the axis along and transverse to the line of centers, respectively. In addition we consider the coupling between rotation of one particle and the hydrodynamic force on another,

$$\mathbf{M}_{\alpha\beta}^{\Omega F}(r, \phi) = \frac{1}{8\pi\eta a^3} y_{\alpha\beta}^b(r; \phi) \boldsymbol{\varepsilon} \cdot \hat{\mathbf{r}}. \quad (2.13)$$

Only one coefficient, $y_{\alpha\beta}^b$, is needed to define this coupling: A force exerted on one particle tending to push it along their line of centers produces no rotation.

However, a hydrodynamic force on a particle that acts transverse to the line of centers between a pair will drag fluid between the two, resulting in rotational motion of the the second. The computations of $x_{\alpha\beta}^c$, $y_{\alpha\beta}^c$ and $y_{\alpha\beta}^b$ via our stochastic technique are given in the Appendix.

Effects of system size on structure and mechanical properties must be taken into account when setting the simulation box size or, equivalently, the number of particles utilized at a given volume fraction. An important example of such effects can arise from the utilization of periodic replication to simulate an infinite suspension, which can produce interactions between any given particle and its periodic images. When a force is exerted on one such particle, its motion, combined with that of all of its periodic images, produces a weak back-flow; however, this well-known quantitative effect is easily accounted for; when system size is small, analytical corrections can be applied [90, 93], which show that as system size is increased, sensitivity of short-time self-diffusion and sedimentation coefficients on system size become weak. In the present study, only one pair of particles among a random sea of N_p particles is subjected to a force during a given calculation; thus, as N_p grows, this effect weakens. A range of system sizes was tested for each volume fraction studied here, where it was found that sensitivity of mobility coefficients on system size becomes negligible for $N_p > 1,500$. A system size of $N_p = 2,000$ was thus selected for all volume fractions studied.

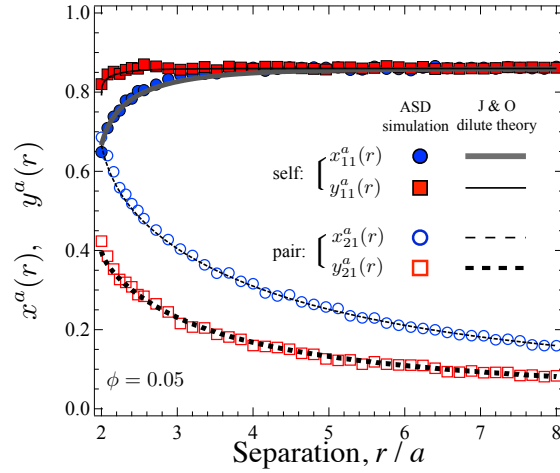


Figure 2.2: Longitudinal and transverse mobility coefficients coupling force on the surface of a particle to the motion of that and other particles. Solid lines: dilute theory of Jeffrey and Onishi[84], scaled on the concentrated self-mobility as measured in simulation in the present study. Symbols: simulation results from present study for volume fraction $\phi = 0.05$. From [150], with permission.

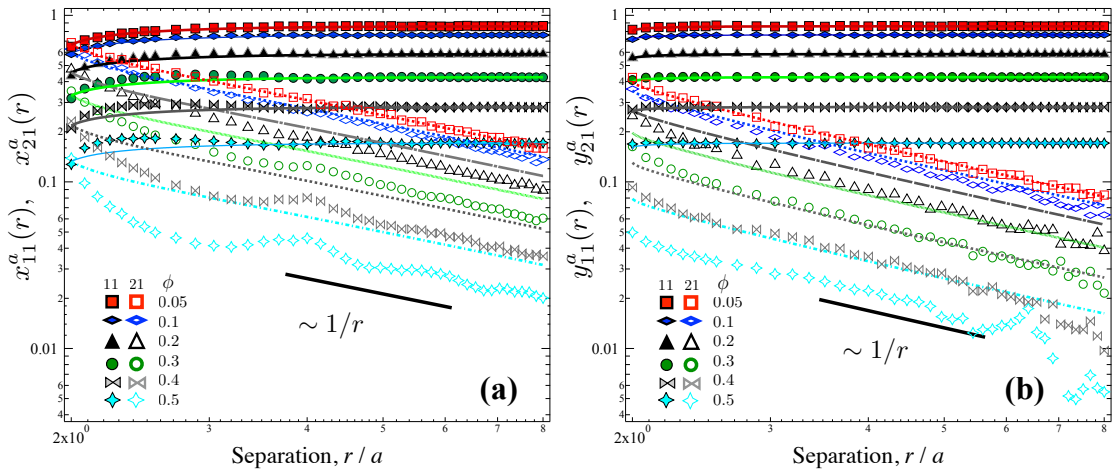


Figure 2.3: Longitudinal and transverse mobility coefficients coupling force on the surface of a particle to the motion of that and other particles, in a concentrated suspension. Solid lines: dilute theory of Jeffrey and Onishi[84], scaled on the volume-fraction dependent short-time self-diffusivity of a particle as determined in simulation in the present study. Symbols: simulation results from present study for volume fractions as shown in legend. (a) Longitudinal self- and pair-mobility. (b) Transverse self- and pair-mobility. From [150], with permission.

2.4 Results

In this section we present the concentration-dependent mobility coefficients in equations 2.3, 2.12, and 2.13, as computed via equations 2.8 - 2.11, 2.21 - 2.24, and 2.31 - 2.32, for suspensions at volume fractions ranging from $0.05 \leq \phi \leq 0.5$. We begin with the velocity-force coupling $M_{\alpha\beta}^{UF}$ and the coefficients $x_{\alpha\beta}^a(r, \phi)$ and $y_{\alpha\beta}^a(r, \phi)$. Here, α and β take on all values from 1 to N , that is, the interactions between all particle pairs is obtained by computing an average over all but two particles. Thus, in all plots that follow, the interacting pair are simply labeled $\alpha = 1$ and $\beta = 2$. Because the particles are identically sized, $\mathbf{M}_{11}^{UF} = \mathbf{M}_{22}^{UF}$ and $\mathbf{M}_{12}^{UF} = \mathbf{M}_{21}^{UF}$; only the coefficients corresponding to \mathbf{M}_{11}^{UF} and \mathbf{M}_{21}^{UF} are shown.

To lay the groundwork for discussion, we begin by presenting the dilute theory results and discussing the physical meaning of each of the coefficients. As discussed in section 2.2, for an isolated pair of particles, the hydrodynamic functions depend only on their separation r and were computed by Jeffrey and Onishi [84]. Those coefficients $x_{\alpha\beta}^a(r, \phi \rightarrow 0)$ and $y_{\alpha\beta}^a(r, \phi \rightarrow 0)$ are plotted in figure 2.2 (solid and dashed lines).

The longitudinal and transverse self-mobility coefficients $x_{11}^a(r)$ and $y_{11}^a(r)$ give the degree to which the motion of a forced particle β is reduced by the presence of the no-slip surface of a nearby particle α . In contrast, the longitudinal and transverse *pair* mobilities $x_{21}^a(r)$ and $y_{21}^a(r)$ give the strength of entrainment of particle α due to the same force on particle β ; that is, particle α gets dragged along in the disturbance flow produced by forced particle β . The former, the self-mobility coefficients, grow with separation r/a toward the self-mobility of an isolated particle. Physically, a particle can move more freely when the sec-

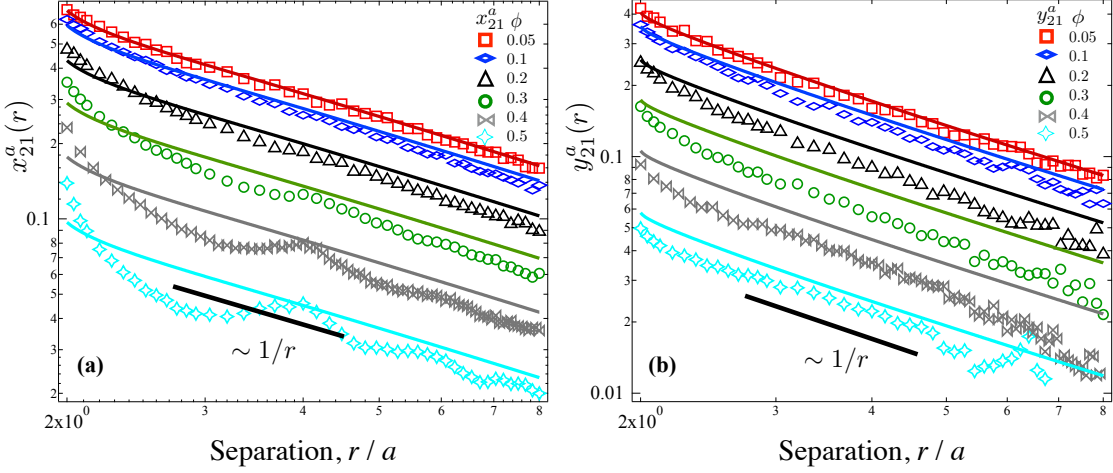


Figure 2.4: Effective viscosity re-scaling. (a) Longitudinal and (b) transverse force-velocity coupling. Solid lines: dilute theory of Jeffrey and Onishi[84], scaled on the volume-fraction dependent high-frequency viscosity $\eta'(\phi)$ as determined in simulation in the present study. Symbols: simulation results from present study for volume fractions as shown in legend. From [150], with permission.

ond particle is far away. For closely spaced particles, $r/a \rightarrow 2$, the self-mobility is strongly hindered by the neighboring no-slip surface, and lubrication forces become important. The self- and pair-mobility take on the same value at contact, i.e., two particles in contact move together. In contrast, the transverse self- and pair coefficients y_{11}^a and y_{21}^a differ at contact: one particle can pass the other on a trajectory offset from the line of centers. Comparing the self-mobility coefficients to the pair-mobility coefficients, a final contrast can be noted: the latter decay with separation, owing to weakening entrainment as the two get farther apart. However, the decay is slow: it scales as $1/r$, owing to the leading-order fluid disturbance propagated by a particle translating in Stokes flow. It is this long-range coupling that leads to complex interactions when there are more than two particles.

We compare these dilute theory results to simulation, where x^a and y^a have

been computed for volume fraction $\phi = 0.05$. These results are plotted in figure 2.2 as a function of separation distance r/a (filled and open symbols). The dilute theory is scaled up for finite concentrations with the short-time self-diffusivity of a single particle, $D_0^S(\phi)$,[27] as computed in simulation. Agreement between simulation and theory is excellent, demonstrating the accuracy of the simulation measurements and confirming that a dilute intervening medium of mobile particles does not screen hydrodynamic interactions.

To examine the effect of higher concentrations on the pair mobility, the suspension concentration is increased, spanning the range $0.1 \leq \phi \leq 0.5$. The self- and pair mobility coefficients were measured and are plotted in figures 2.3(a) and (b) for the longitudinal (x^a) and transverse (y^a) couplings, respectively, alongside the dilute theory of Jeffrey & Onishi. Several interesting trends emerge.

The self and pair mobility both decay as $1/r$ over the entire range, confirming that entrainment of one particle in the flow created by the motion of another extends over long distances, over many particle sizes. At wide separations, the self mobility eventually asymptotes to a mean, far-field behavior. At close separations, interesting behavior can be observed. At higher concentrations, undulations in the curves appear near contact. The first such undulation occurs at the separation at which only a single particle is admitted into the intervening gap. Here, particle mobility is reduced by the neighboring no-slip surfaces as well as steric hindrance. As the separation decreases further, the pair excludes any intervening particles, and the self mobilities increase because the particles diffuse with a pure solvent-filled pocket between them. This behavior is even more prominent in the pair mobility. The pair mobility at close separations could then

be viewed as a sensitive measure of local liquid structure. This interesting structure occurs at separations where mean-field theories approximate the coupling as monotonically (linearly) varying, or simply constant.

While the qualitative behavior is the same for all the curves, there is a quantitative difference between dilute theory and finite concentrations. The offset suggests an $O(1)$ suppression of the coupling that becomes more pronounced as volume fraction increases. This is unsurprising, because a suspension of particles with its many no-slip surfaces is a more dissipative medium than a pure solvent. The $1/r$ power-law behavior, combined with the weak quantitative reduction in mobility indicates that the medium still obeys Stokes equations but suggests an effective viscosity set by the background suspension. The natural scaling for the effective viscosity is the high-frequency viscosity, $\eta'_\infty(\phi)$, as it corresponds to short time scale motion of the particles. This suggests a rescaling of the pair mobility coefficients with $\eta'_\infty(\phi)$. Figure 2.4 shows that scaling the coefficients on the high-frequency viscosity (as measured in simulation) gives excellent agreement between the pair mobility of particles interacting via a Newtonian solvent of viscosity η and interacting via a suspension of effective viscosity $\eta'_\infty(\phi)$. This suggests that one can approximate the concentrated self and pair mobility as

$$\mathbf{M}_{11}^{UF}(\phi) = \frac{\mathbf{D}_0^S(\phi)}{kT} + \frac{\eta}{\eta'_\infty(\phi)} \left(\mathbf{M}_{11}^{UF, dilute} - \frac{\mathbf{I}}{6\pi\eta a} \right), \quad (2.14)$$

$$\mathbf{M}_{21}^{UF}(\phi) = \frac{\eta}{\eta'_\infty(\phi)} \mathbf{M}_{21}^{UF, dilute}. \quad (2.15)$$

The *relative* mobility of a pair of particles is an important quantity employed extensively in the analysis of suspension dynamics. Using Batchelor's

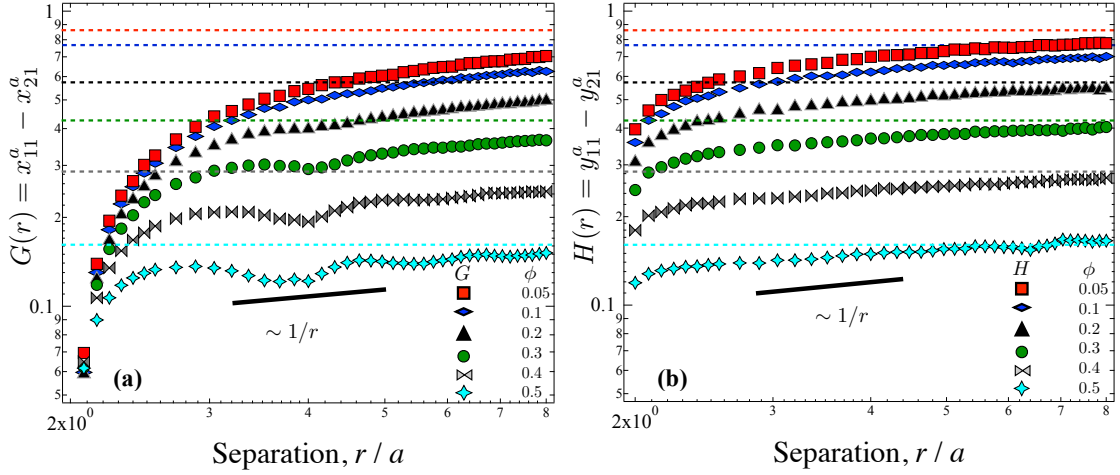


Figure 2.5: Relative mobility in concentrated suspensions. (a) Longitudinal and (b) Transverse relative mobility for a range of concentrations as shown in legend. Dashed lines: concentration-dependent short-time self-diffusivity as computed in simulation. Symbols: relative mobility as computed in simulation in the present study, for volume fractions as shown in legend. From [150], with permission.

notation[13] the longitudinal and transverse relative mobilities are

$$G(r) \equiv x_{11}^a(r, \phi) - x_{21}^a(r, \phi), \quad (2.16)$$

$$H(r) \equiv y_{11}^a(r, \phi) - y_{21}^a(r, \phi). \quad (2.17)$$

These functions are plotted in figures 2.5 (a) and (b) for the longitudinal and transverse relative mobility, respectively. At contact the longitudinal relative mobility $G(r, \phi)$ vanishes as the two particles travel together in tandem motion. In contrast, $H(r)$ remains nonzero at contact, showing that a pair of particles can pass one another. The growth in mobility is initially rapid as a pair separates, but asymptotes toward the far-field value slowly, as $1/r$. For $\phi \leq 0.4$, the far-field value is not reached even at separations of eight particle radii – much longer ranged than transition points identified in mean-field theories. Only in the case

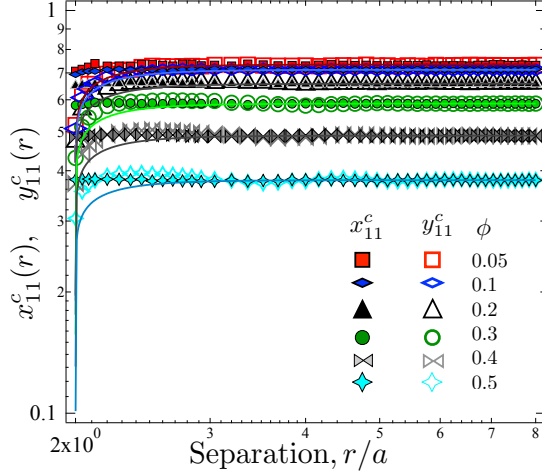


Figure 2.6: Torque-rotation coupling: the self-mobility coupling the torque on one particle and its own and others' rotation. Solid lines: dilute theory of Jeffrey and Onishi[84], scaled on the concentration-dependent rotational self-diffusivity as measured in dynamic simulation in the present study. Symbols: longitudinal and transverse self-mobility coefficients for a range of concentrations, as shown in the legend. From [150], with permission.

of $\phi = 0.5$ is the asymptote reached, but only at eight particle separations, and only after slow $1/r$ growth.

Thus far we have seen that the long-ranged coupling between forces exerted on one particle and the velocity of another persists regardless of suspension concentration. Further, the relative mobilities, the workhorse functions employed in the modeling of suspension dynamics, also display this strong $1/r$ behavior. Clearly, then, it is neither physically appropriate nor accurate to model such interactions as constant beyond the lubrication range, and even less so to neglect entirely the impact of long-range hydrodynamic forces on the relative motion of particles.

Another coupling between particle motion and surface tractions is that between rotation and torque, $M_{\alpha\beta}^{\Omega L}$. A torque exerted on one particle can cause it and other nearby particles to rotate, where the coupling is given by equation 2.12. The coefficients $x_{\alpha\beta}^c$ and $y_{\alpha\beta}^c$ give the rotation of particle α due to a hydrody-

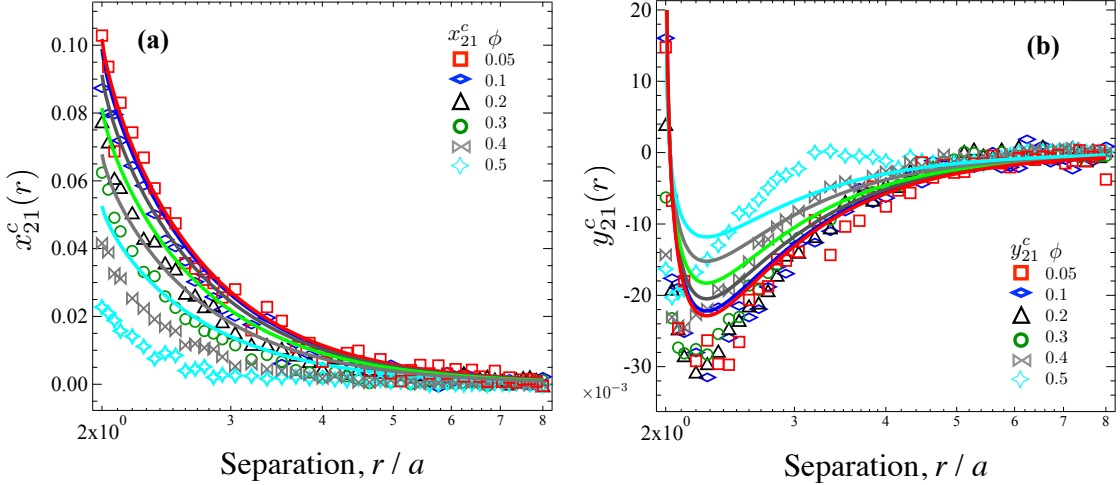


Figure 2.7: Torque-rotation coupling: the pair-mobility coupling the torque on one particle and its own and others' rotation. Solid lines: dilute theory of Jeffrey and Onishi[84], scaled on the concentration-dependent rotational self-diffusivity as measured in dynamic simulation in the present study. Symbols: (a) longitudinal and (b) transverse pair-mobility coefficients for a range of concentrations, as shown in the legend. From [150], with permission.

namic torque on particle β , about the axis along and transverse to the line of centers, respectively (equations 2.21 - 2.24) . These couplings are plotted in figure 2.6 for a range of volume fractions as obtained via simulation (filled symbols) alongside the values computed via the dilute theory of Jeffrey and Onishi [84] (solid lines). The torque-rotation self-mobilities follow a trend similar to that of the force-velocity self-mobility: the more distant a particle is from a neighboring particle, the easier it is for that particle to freely rotate. An increase in volume fraction of the surrounding and intervening particles decreases the self-mobility of a test particle, regardless of its distance from the other test particle. However, as a pair of test particles gets closer than the distance required to admit one intervening particle, the rotational self-mobility increases slightly (even above the normalized value for an isolated pair), as the intervening medium is simply solvent. Near contact, this gives way to a decrease in self mobility to a finite value,

reflecting the reduction in rotational speed due to the no-slip surface of the second particle.

The corresponding entrainment, or rotational pair-mobility, is plotted in figure 2.7, where $x_{21}^c(r)$ is shown in (a) and corresponds to the rotation of one particle about the line of centers between the pair, due to a hydrodynamic torque on the other particle about the same axis. The coupling is strongest near contact, but it is weaker than that for the force-velocity coupling at contact. Physically, one can imagine the ease with which two parallel discs enclosing a fluid can be rotated on their common axis, compared to the force required to squeeze the discs together. The coupling weakens as the pair becomes widely separated, vanishing at infinite separation—even in concentrated suspensions. The decay scales as $\sim 1/r^3$ in the dilute case. As concentration increases, the coupling grows weaker due to the many no-slip surfaces between the pair, but the effect of concentration is, as with the force-velocity coupling, quantitative rather than qualitative. That is, there is no evidence of hydrodynamic screening of the axial torque-rotation coupling.

Besides rotation about the line of centers connecting two particles, each particle can rotate about an axis transverse to the line of centers and passing through its own center. The coefficient y_{21}^c describes the tendency for one particle to rotate about such a transverse axis due to a hydrodynamic torque on the other particle about its own transverse axis. This coefficient is plotted in figure 2.7(b). When two particles are well-separated, the coupling is weak, and they do not respond to one another. As they approach, the coupling is negative because the particles counter-rotate, that is, each rotates about an axis parallel to the axis of rotation of the other, in a calendering motion.

However, the coefficient is non-monotonic in the separation: the strength of the coupling first grows in magnitude as they approach. When the pair gets very close, the coupling reverses, changing from counter- to co-rotation: they rotate as a couplet. A strong lubrication force is responsible for the reversal in the coupling. This behavior is present whether the particles interact via a pure solvent or via a suspension of particles at any concentration. However, as concentration grows, the point of reversal (the dip in the curve) moves, suggesting that the particles must get closer to co-rotate, owing to steric hindrance. While increasing concentration quantitatively suppresses the coupling at all finite separations, the interaction always scales as $1/r^3$.

The final coupling we consider is between rotation of one particle and the hydrodynamic force on another, $\mathbf{M}_{\alpha\beta}^{\Omega F}$, as given by equations 2.13 and 2.27. A force exerted on one particle tending to push it along their line of centers produces no rotation. However, a hydrodynamic force on a particle that acts transverse to the line of centers between a pair will drag fluid between the two, resulting in rotational motion of the second. The self-mobility coefficient y_{11}^b and the negative of the pair-mobility coefficient y_{21}^b for an isolated pair of spheres and for a pair interacting in a suspension are plotted in figures 2.8(a) and (b) respectively. When a pair of particles is widely separated, a hydrodynamic force on one will induce no rotation of the other. As the two particles approach one another, the forced particle drags fluid between the pair, inducing rotation of the second. In the dilute limit, y_{11}^b grows monotonically to a finite value. While high concentration quantitatively suppresses the coupling at close separations, it always scales as $1/r^3$, regardless of concentration. Interestingly, for concentrated suspensions the coupling changes sign when the pair just excludes particles from their intervening (pure solvent) gap, suggesting that the coupling of the forced particle

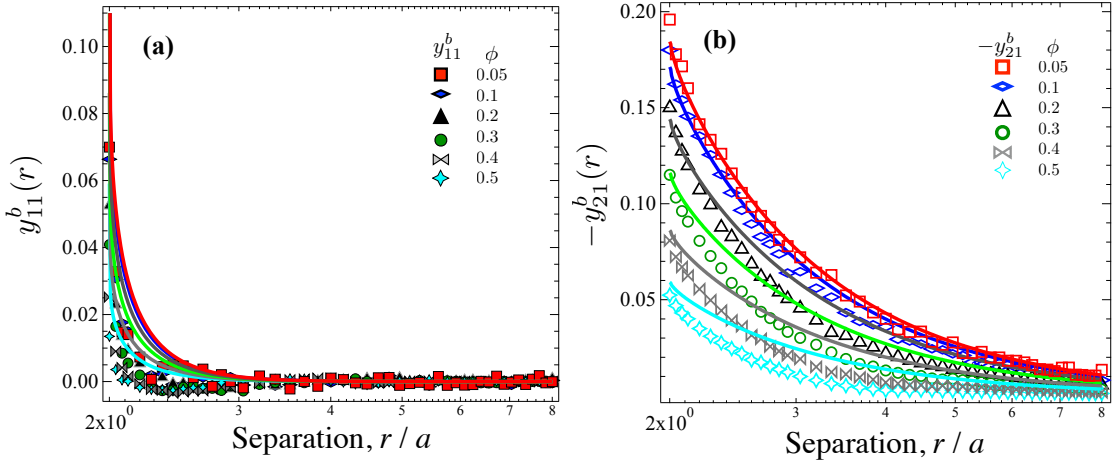


Figure 2.8: Force-rotation coupling: the self- and pair-mobility coupling the force on one particle and its own and others' rotation. (a) Self- and (b) pair-mobility coefficients for a range of concentrations, as shown in the legend. Solid lines: dilute theory of Jeffrey and Onishi[84], scaled on an average of the concentration-dependent rotational and translational self-diffusivity as measured in dynamic simulation in the present study. Symbols: coefficients computed via dynamic simulation. From [150], with permission.

to the background suspension particles in such configurations reverses its rotation compared to an isolated pair. At separations less than a particle size, the forced particle rotates in a motion that would cause it to roll around the second particle. While concentration and crowding do not screen long-range hydrodynamic interactions this near-field effect, arising from local liquid-like structure, is indeed a consequence of crowding and may lead to important consequences in collective motion in e.g. biophysical systems.

The transverse force/rotation pair mobility, y_{21}^b , is shown in 2.8(b). It increases monotonically from a small finite value at wide separations as a pair approaches one another, regardless of concentration. The $1/r^2$ scaling does in fact change with concentration, suggesting screening. At any concentration, interaction even at wide separations is weakened by the presence of the intervening particles. The two particles must get closer before the force on one induces

rotation of the other.

Comparison of the transverse self- and pair-mobility coefficients y_{11}^b and y_{21}^b shows that when separated, they take on different numerical values and opposite sign. That is, one particle will “roll” around the surface of the other. But at contact, the similarity of the coefficients depends on volume fraction. For an isolated pair alone in a solvent (the dilute theory), the coefficients take on the same magnitude but opposite sign, meaning that the pair will rotate as a solid body, with no relative rolling motion. But at finite concentrations, even as small as $\phi = 0.05$, this reflective/rotational symmetry is broken, owing to three-body interactions.

2.5 Conclusions

We have formulated a theoretical and computational approach, based on the Accelerated Stokesian Dynamics algorithm, for measuring the concentration-dependent hydrodynamic mobility functions coupling the motion of one particle to hydrodynamic tractions on its surface and the surface of a second particle, with a view toward developing a set of hydrodynamic pair- and relative-mobility functions analogous to the dilute functions of Jeffrey and Onishi [84], but now for arbitrary suspension concentration. Utilizing these functions, we addressed the question of whether reduction in particle self-mobility due to crowding in concentrated suspensions can be extrapolated to pair interactions and thus effectively screens out long-range hydrodynamic coupling between particles and, if so, over what range this takes place. To model this behavior, we have devised a new stochastic sampling technique to rapidly calculate an

analogous set of mobility functions describing the hydrodynamic interactions between two spheres immersed in a suspension of identical spheres. Our results confirm that long-range hydrodynamic interactions in suspensions of freely diffusing particles are not screened, regardless of the concentration of the suspension.

Three couplings were presented: that between velocity and force, between rotation and torque, and between rotation and force. The strongest long-range interaction derives from the first coupling, that of force and velocity, which decays as $1/r$ for an isolated pair of particles alone in a Newtonian solvent. When the pair is placed in a suspension, our computations of the coupling functions show that the entrainment of one particle by another still scales as $1/r$, regardless of the volume fraction of intervening particles. Thus, the pair- and relative mobilities show no qualitative dependence on volume fraction. Rather, a re-scaling of the simulation data on the volume-fraction dependent high-frequency viscosity $\eta'_\infty(\phi)$ shows that a pair of test particles interacts via an effective medium with an effective viscosity given by $\eta'_\infty(\phi)$. Similarly, neither the torque/rotation coupling nor the force/rotation coupling displayed hydrodynamic screening behavior. In all three couplings, interesting near-contact behavior manifested at finite concentrations, including undulating values of the force-velocity mobility as the local liquid-like structure of particles between a pair was interrupted. The results we have presented constitute a full set of orthogonal coupling functions which may now be used in a pair-like Smoluchowski equation governing many hydrodynamically interacting particles. The quantities measured in simulation correspond to analogous measurements that can be taken in microscopy experiments, thus providing a natural means to validate the theory. Further, such experiments could be extended to systems of

non-spherical or soft particles.

2.6 Appendix

The coupling between particle rotation and hydrodynamic force is given by

$$\boldsymbol{\Omega}_\alpha = \mathbf{M}_{\alpha\beta}^{\Omega L} \cdot \mathbf{L}_\beta. \quad (2.18)$$

Each particle is subjected to a random torque, with zero mean and identity covariance:

$$\overline{\mathbf{L}^R} = 0, \quad \overline{\mathbf{L}^R \mathbf{L}^R} = \mathbf{I}_{3N}. \quad (2.19)$$

Thus we have

$$\begin{aligned} \langle \overline{\boldsymbol{\Omega}_\alpha \mathbf{L}} \rangle &= \langle \overline{\mathbf{L}^R \mathbf{L}^R} \cdot \mathbf{M}^{\Omega L} \rangle \\ &= \langle \mathbf{I}_{3N} \cdot \mathbf{M}^{\Omega L} \rangle \\ &= \langle \mathbf{M}^{\Omega L} \rangle, \end{aligned} \quad (2.20)$$

where $\langle \cdot \rangle$ denotes the ensemble average over many configurations. The longitudinal rotation/torque coefficient for self motion is given by

$$\begin{aligned} x_{11}^c &= \frac{1}{2} \hat{\mathbf{r}}_{\alpha\beta} \hat{\mathbf{r}}_{\alpha\beta} : (\mathbf{M}_{\alpha\alpha}^{\Omega L} + \mathbf{M}_{\beta\beta}^{\Omega L}) \\ &= \frac{1}{2} \hat{\mathbf{r}}_{\alpha\beta} \hat{\mathbf{r}}_{\alpha\beta} : (\boldsymbol{\Omega}_\alpha \mathbf{L}_\alpha^R + \boldsymbol{\Omega}_\beta \mathbf{L}_\beta^R) \\ &= \frac{1}{2} [(\boldsymbol{\Omega}_\alpha \cdot \hat{\mathbf{r}}_{\alpha\beta})(\mathbf{L}_\alpha^R \cdot \hat{\mathbf{r}}_{\alpha\beta}) + (\boldsymbol{\Omega}_\beta \cdot \hat{\mathbf{r}}_{\alpha\beta})(\mathbf{L}_\beta^R \cdot \hat{\mathbf{r}}_{\alpha\beta})], \end{aligned} \quad (2.21)$$

and for pair motion,

$$x_{21}^c = \frac{1}{2} [(\boldsymbol{\Omega}_\alpha \cdot \hat{\mathbf{r}}_{\alpha\beta})(\mathbf{L}_\beta^R \cdot \hat{\mathbf{r}}_{\alpha\beta}) + (\boldsymbol{\Omega}_\beta \cdot \hat{\mathbf{r}}_{\alpha\beta})(\mathbf{L}_\alpha^R \cdot \hat{\mathbf{r}}_{\alpha\beta})]. \quad (2.22)$$

The transverse rotation/torque coupling for self motion is

$$\begin{aligned} y_{11}^c &= \frac{1}{4} (\mathbf{I} - \hat{\mathbf{r}}_{\alpha\beta} \hat{\mathbf{r}}_{\alpha\beta}) : (\mathbf{M}_{\alpha\alpha}^{\Omega L} + \mathbf{M}_{\beta\beta}^{\Omega L}) \\ &= \frac{1}{4} (\mathbf{I} - \hat{\mathbf{r}}_{\alpha\beta} \hat{\mathbf{r}}_{\alpha\beta}) : (\boldsymbol{\Omega}_\alpha \mathbf{L}_\alpha^R + \boldsymbol{\Omega}_\beta \mathbf{L}_\beta^R) \\ &= \frac{1}{4} (\boldsymbol{\Omega}_\alpha \cdot \mathbf{L}_\alpha^R + \boldsymbol{\Omega}_\beta \cdot \mathbf{L}_\beta^R - 2x_{21}^{11}) \end{aligned} \quad (2.23)$$

and for the corresponding pair mobility we have

$$y_{21}^c = \frac{1}{4}(\boldsymbol{\Omega}_\alpha \cdot \mathbf{L}_\beta^R + \boldsymbol{\Omega}_\beta \cdot \mathbf{L}_\alpha^R - 2x_C^{21}). \quad (2.24)$$

The coupling between particle rotation and the hydrodynamic force is expressed as:

$$\boldsymbol{\Omega}_\alpha = \mathbf{M}_{\alpha\beta}^{\Omega F} \cdot \mathbf{F}_\beta, \quad (2.25)$$

where the forces on the particles are still selected to be random with zero mean and identity covariance,

$$\overline{\mathbf{F}^R} = 0, \quad \overline{\mathbf{F}^R \mathbf{F}^R} = \mathbf{I}_{3N}. \quad (2.26)$$

Similar to the procedure above in equation 2.20, we have

$$\begin{aligned} \langle \overline{\boldsymbol{\Omega}_\alpha \mathbf{F}} \rangle &= \langle \overline{\mathbf{F}^R \mathbf{F}^R} \cdot \mathbf{M}^{\Omega F} \rangle \\ &= \langle \mathbf{I}_{3N} \cdot \mathbf{M}^{\Omega F} \rangle \\ &= \langle \mathbf{M}^{\Omega F} \rangle, \end{aligned} \quad (2.27)$$

The mobility $\mathbf{M}^{\Omega F}$ can only have transverse coupling,

$$\mathbf{M}_{ij}^{\Omega F, \alpha\beta} = \Omega_i^\alpha F_j^{R\beta} = y_{\alpha\beta}^B \varepsilon_{ijk} \hat{r}_k^{\alpha\beta} \quad (2.28)$$

where ε_{ijk} is the third-order Levi-Civita tensor. Then we double dot the Levi-Civita tensor to both sides of equation 2.28,

$$\Omega_i^\alpha F_j^{R\beta} \varepsilon_{ijl} = y_{\alpha\beta}^B \varepsilon_{ijk} \varepsilon_{ijl} \hat{r}_k^{\alpha\beta} = 2y_{\alpha\beta}^B \delta_{kl} \hat{r}_k^{\alpha\beta} = 2y_{\alpha\beta}^B \hat{r}_l^{\alpha\beta} \quad (2.29)$$

where δ_{kl} is the identity tensor. Thus we get,

$$y_{\alpha\beta}^B = \frac{1}{2} \Omega_i F_j^R \varepsilon_{ijl} \hat{r}_l^{\alpha\beta} \quad (2.30)$$

i.e.,

$$y_{11}^B = \frac{1}{4} [(\boldsymbol{\Omega}_\alpha \times \mathbf{F}_\alpha^R) \cdot \hat{\mathbf{r}}_{\alpha\beta} - (\boldsymbol{\Omega}_\beta \times \mathbf{F}_\beta^R) \cdot \hat{\mathbf{r}}_{\alpha\beta}] \quad (2.31)$$

and

$$y_{21}^B = \frac{1}{4} [(\boldsymbol{\Omega}_\beta \times \mathbf{F}_\alpha^R) \cdot \hat{\mathbf{r}}_{\alpha\beta} - (\boldsymbol{\Omega}_\alpha \times \mathbf{F}_\beta^R) \cdot \hat{\mathbf{r}}_{\alpha\beta}] \quad (2.32)$$

CHAPTER 3

**PAIR MOBILITY FUNCTIONS FOR RIGID SPHERES IN
CONCENTRATED COLLOIDAL DISPERSIONS: STRESSLET AND
STRAINING MOTION COUPLINGS**

3.1 Introduction

In Chapter 2, we studied monodisperse, hard spheres suspended in a Newtonian fluid, where small particle size gives a vanishingly small Reynolds number. We developed a set of hydrodynamic mobility functions coupling particle translation and rotation to hydrodynamic force and torque. The primary goals of that study were to establish a means by which one could compute properties of dense suspensions analytically, and to determine the degree to which such level of detail was necessary, i.e., to understand whether the entrainment of one particle by the motion of another is “screened out” at high concentrations. We showed that hydrodynamic interactions are not screened by crowding. This finding is consistent with earlier results from Banchio et al. [9], who found that theoretical analysis of many-body hydrodynamic interactions matches the observations from experiments for dense suspensions of charged colloidal spheres (but without connection to the concept of hydrodynamic screening). Here we put forth an extension of Chapter 2 to include the coupling of particle motion and straining flow to the hydrodynamic stresslet. We again utilize a stochastic sampling technique to obtain suspension-averaged self- and entrained mobility for a pair of particles interacting with one another through an intervening medium of solvent and particles, with volume fraction ranging from $0.01 \leq \phi \leq 0.5$.

The remainder of this chapter is organized as follows. In Section 3.2, we briefly review the mobility tensors that couple particle motion to hydrodynamic force, torque and straining motion. In Section 3.3, the computational approach is presented, where Accelerated Stokesian Dynamics (ASD) simulations [133] are utilized with our recently developed stochastic sampling technique [150]. In Section 3.4, we present results for suspensions of various volume fractions, ranging from dilute to concentrated. The study is concluded with a discussion in Section 3.5.

3.2 Hydrodynamic couplings

In Chapter 2, we developed mobility tensors coupling force and torque to translation and rotation for a pair of particles interacting through an intervening colloidal suspension, as a function of their separation from one another, for a range of suspension concentrations. In this section we give an overview of the hydrodynamic couplings to be studied in this work.

We start with a general linearity expression of the coupling between particle motion and hydrodynamic traction moments. In many problems in suspension mechanics, while the forces and torques on particles are known, the resulting motion is sought. This is expressed compactly as

$$\begin{pmatrix} \mathbf{U} - \mathbf{U}^\infty \\ \boldsymbol{\Omega} - \boldsymbol{\Omega}^\infty \\ \mathbf{E} - \mathbf{E}^\infty \\ \vdots \end{pmatrix} = \mathcal{M} \cdot \begin{pmatrix} \mathbf{F}^H \\ \mathbf{L}^H \\ \mathbf{S}^H \\ \vdots \end{pmatrix}. \quad (3.1)$$

On the left hand side of (3.1) are the velocity derivatives: translational veloc-

ity, rotational velocity, rate of strain, and higher-order derivatives. On the right hand side are the hydrodynamic traction moments: force, torque, stresslet and higher-order moments. The grand mobility matrix, \mathbf{M} , is the coupling tensor. However, expression (3.1) has two limitations: first, there are an infinite number of unknowns on the right hand side even when one knows the values of imposed forces and torques, because all higher-order moments are induced by flow and cannot be known a priori. Second, when assembled analytically from pair theory, \mathbf{M} is a pair-level matrix that does not account for many-body hydrodynamic interactions. The first problem is overcome by recognizing that, in the case of rigid particles, all stresslets and higher order traction moments are induced by flow. Kim and Mifflin [89] proposed that it is thus logical for these elements to appear on the left hand side of the linearity statement (3.1), alongside the particle velocities, \mathbf{U} and $\boldsymbol{\Omega}$. Rearrangement of the couplings in this manner places all unknown quantities on the left-hand side. On the right-hand side are now the known quantities. The new linearity expression includes a coupling matrix with notation that replaces the familiar mobility tensors \mathbf{M} with tensors that include linear transformations required for the left-right exchange of higher-order couplings:

$$\begin{pmatrix} \mathbf{U} - \mathbf{U}^\infty \\ \boldsymbol{\Omega} - \boldsymbol{\Omega}^\infty \\ \mathbf{S} \\ \vdots \end{pmatrix} = \begin{pmatrix} \left[\begin{matrix} \mathbf{a} & \tilde{\mathbf{b}} \\ \mathbf{b} & \mathbf{c} \end{matrix} \right] & \tilde{\mathbf{g}} & \cdots \\ \mathbf{g} & \mathbf{h} & \mathbf{m} \\ \vdots & \vdots & \ddots \end{pmatrix} \cdot \begin{pmatrix} \mathbf{F} \\ \mathbf{L} \\ -\mathbf{E}^\infty \\ \vdots \end{pmatrix}. \quad (3.2)$$

Here, \mathbf{U}^∞ , $\boldsymbol{\Omega}^\infty$, and \mathbf{E}^∞ give the imposed far-field uniform, rotational, and straining flow, and the superscripts H are dropped for brevity. Because the particles are rigid, the rate of strain \mathbf{E} of a particle is identically zero. The terms in the square bracket inside the grand matrix, \mathbf{a} , \mathbf{b} , $\tilde{\mathbf{b}}$, and \mathbf{c} , are the familiar mobility

functions giving the translational velocity and rotational velocity arising from hydrodynamic force and torque between particle pairs [84, 88]. The remaining tensors include the coupling \mathbf{g} of hydrodynamic stresslet to force; the coupling \mathbf{h} of hydrodynamic stresslet to torque; the coupling $\tilde{\mathbf{g}}$ of velocity to flow rate of strain; the coupling $\tilde{\mathbf{h}}$ of rotation to flow rate of strain; and the coupling \mathbf{m} of hydrodynamic stresslet to flow strain rate. Kim and Mifflin [89] utilized the method of boundary collocation to develop exact analytical expressions for all the pair-level couplings in the above grand matrix for two spheres in pure solvent.

The aim of our method is to construct the above elements for a pair of test particles interacting through a suspension of arbitrary concentration, where the couplings are a function both of pair separation and of the volume fraction of the intervening medium. To do so, one must transform the pair- level expression to a many-body linearity expression. In this approach, the pair couplings between all particle pairs, to first reflection, is obtained by a Taylor expansion of the fluid velocity integral equation [94]. This is combined with Fáxen formulae to give couplings between all pairs. Inversion of this matrix automatically couples all particles to one another for an infinitude of reflections among them. Following the Stokesian Dynamics (SD) algorithm [31], this quantity is combined with near-field pair functions to form a complete coupling, including many-body hydrodynamic interactions in near- and far-field as well as lubrication interactions. Following the successful implementation of this program in Chapter 2 on this topic, we employ this method here as well.

We consider two particles embedded in an isotropic suspension of identical spheres of number density n and volume fraction $\phi = 4\pi a^3 n / 3$, where a is the

particle radius. Because on average the suspending medium is isotropic and the fluid is force-free, the couplings can be projected onto orthogonal subspaces, formed by the isotropic tensor \mathbf{I} , multiples of the unit vector $\hat{\mathbf{r}}$, and combinations therein, where \mathbf{r} is the vector of length r separating a pair of particles, and $\hat{\mathbf{r}} = \mathbf{r}/r$. For example, the coupling \mathbf{g} of hydrodynamic stresslet to hydrodynamic force is

$$S_\alpha = \mathbf{g}_{\alpha\beta} \cdot \mathbf{F}_\beta. \quad (3.3)$$

Physically, the hydrodynamic force \mathbf{F}_β on particle β will produce disturbance flows that induce a stresslet S_α , on the surface of particle α . This coupling can be projected onto the two orthogonal subspaces to give

$$\begin{aligned} g_{ijk}^{\alpha\beta}(\phi, r) = & \frac{1}{6\pi\eta a} [x_{\alpha\beta}^s(\phi, r)(\hat{r}_i\hat{r}_j - \frac{1}{3}\delta_{ij})\hat{r}_k \\ & + y_{\alpha\beta}^s(\phi, r)(\hat{r}_i(\delta_{jk} - \hat{r}_j\hat{r}_k) + \hat{r}_j(\delta_{ik} - \hat{r}_i\hat{r}_k))], \end{aligned} \quad (3.4)$$

where δ is the second-rank Dirac tensor and η is the solvent viscosity. The coefficients $x_{\alpha\beta}^s, y_{\alpha\beta}^s$ give the strength of coupling of forces acting along and transverse to the line of centers between the two test particles to the stresslet.

We derived the concentration-dependent mobility couplings $\mathbf{a}, \mathbf{b}, \tilde{\mathbf{b}}$ and \mathbf{c} utilizing this method in our previous work [150]; the couplings $\mathbf{g}, \tilde{\mathbf{g}}, \mathbf{h}, \tilde{\mathbf{h}}$, and \mathbf{m} in Equation (3.2) are obtained in the present study.

3.3 Computational approach

The stochastic sampling technique utilized to efficiently compute and extract the couplings is presented in detail in Chapter 2. Here we review it briefly, and expand it to model new couplings.

Stokesian dynamics is a well-known algorithm utilized to model many-body hydrodynamic interactions in colloidal and non-colloidal suspensions [31]. It utilizes a two-body approach to compute the near-field hydrodynamic interactions, and evaluates far-field many-body hydrodynamics via multipole expansion and efficient methods to carry out inversion operations to produce a many-body coupling. Most recently, with the method of Particle-Mesh-Ewald (PME), Sierou and Brady [133] developed Accelerated Stokesian Dynamics (ASD) simulations, a $O(N \log N)$ algorithm which facilitates simulating $O(10^3)$ particles, where N is the number of particles in the suspension.

In ASD simulations, particle motion \mathbf{U} and $\boldsymbol{\Omega}$ and the induced stresslet \mathbf{S} in Equation (3.2) can be obtained when externally imposed forces, torques, and straining flow are known. Here, \mathbf{U} , $\boldsymbol{\Omega}$, \mathbf{F} , and \mathbf{L} are vectors of size $3N$ representing particle translation and rotation, and hydrodynamic force and torque. The stresslet and strain rate, \mathbf{S} and \mathbf{E}^∞ , are second order tensors; thus the block matrices \mathbf{g} , $\tilde{\mathbf{g}}$, \mathbf{h} , and $\tilde{\mathbf{h}}$ are third rank and \mathbf{m} is fourth rank. For computational convenience these couplings are mapped to second order tensors, e.g., the stresslet/force coupling is converted using a third order tensor \mathbf{P}^E , that preserves the handedness of the coupling,

$$g_{ijk} = P_{ijk}^E g_{lk}. \quad (3.5)$$

Similarly, the stresslet and rate of strain, which are originally second order tensors, are mapped onto vectors with $5N$ elements (because the stresslet and rate of strain are symmetric and traceless, each has 5 degrees of freedom). The stresslet/force coupling in Equation (3.2) is

$$\mathbf{S} = \mathbf{g} \cdot \mathbf{F}. \quad (3.6)$$

We select a random force for $\mathbf{F} = \mathbf{F}^R$, with zero mean and identity covariance,

$$\overline{\mathbf{F}^R} = 0, \overline{\mathbf{F}^R \mathbf{F}^R} = \mathbf{I}_{3N}, \quad (3.7)$$

where \mathbf{I}_{3N} is the $3N$ -dimensional identity tensor, and the overbar signifies an average over realizations of the random force. The dyadic of the stresslet and random force \mathbf{F}^R can thus be written

$$\begin{aligned} \langle \overline{\mathbf{S} \mathbf{F}^R} \rangle &= \langle \overline{\mathbf{F}^R \mathbf{F}^R} \cdot \mathbf{g} \rangle \\ &= \langle \mathbf{I}_{3N} \cdot \mathbf{g} \rangle \\ &= \langle \mathbf{g} \rangle. \end{aligned} \quad (3.8)$$

In our approach, for a particular configuration of particles, we repeatedly generate random forces on each particle; an overline indicates a quantity that has been averaged over several sets of random forces applied to all pairs separated by a given distance. This process is repeated for several particle configurations, and averaging quantities over these realizations gives an ensemble average denoted by angle brackets, $\langle \cdot \rangle$. Subsequent averaging over multiple configurations $\langle \cdot \rangle$ gives the effective pair function $\langle \mathbf{g}_{\alpha\beta} \rangle$. Equations (3.4), (3.5) and (3.8) are then utilized to express the parallel self- and pair-coefficients as:

$$\begin{aligned} x_{11}^g &= \frac{3}{4} \hat{\mathbf{r}}_{\alpha\beta} \hat{\mathbf{r}}_{\alpha\beta} \hat{\mathbf{r}}_{\alpha\beta} : (\langle \mathbf{g}_{\alpha\alpha} \rangle - \langle \mathbf{g}_{\beta\beta} \rangle) \\ &= \frac{3}{4} \hat{\mathbf{r}}_{\alpha\beta} \hat{\mathbf{r}}_{\alpha\beta} \hat{\mathbf{r}}_{\alpha\beta} : (\mathbf{P}^E \cdot \langle \mathbf{g}_{\alpha\alpha} \rangle - \mathbf{P}^E \cdot \langle \mathbf{g}_{\beta\beta} \rangle) \\ &= \frac{3}{4} \hat{\mathbf{r}}_{\alpha\beta} \hat{\mathbf{r}}_{\alpha\beta} \hat{\mathbf{r}}_{\alpha\beta} : (\mathbf{P}^E \cdot \overline{\mathbf{S}_\alpha \mathbf{F}_\alpha^R} - \mathbf{P}^E \cdot \overline{\mathbf{S}_\beta \mathbf{F}_\beta^R}) \\ &= \frac{3}{4} \left\{ (\overline{\mathbf{F}_\alpha^R \cdot \hat{\mathbf{r}}_{\alpha\beta}}) [(\overline{\mathbf{P}^E \cdot \mathbf{S}_\alpha}) : \hat{\mathbf{r}}_{\alpha\beta} \hat{\mathbf{r}}_{\alpha\beta}] \right. \\ &\quad \left. - (\overline{\mathbf{F}_\beta^R \cdot \hat{\mathbf{r}}_{\alpha\beta}}) [(\overline{\mathbf{P}^E \cdot \mathbf{S}_\beta}) : \hat{\mathbf{r}}_{\alpha\beta} \hat{\mathbf{r}}_{\alpha\beta}] \right\}. \end{aligned} \quad (3.9)$$

$$\begin{aligned} x_{21}^g &= \frac{3}{4} \left\{ (\overline{\mathbf{F}_\alpha^R \cdot \hat{\mathbf{r}}_{\alpha\beta}}) [(\overline{\mathbf{P}^E \cdot \mathbf{S}_\beta}) : \hat{\mathbf{r}}_{\alpha\beta} \hat{\mathbf{r}}_{\alpha\beta}] \right. \\ &\quad \left. - (\overline{\mathbf{F}_\beta^R \cdot \hat{\mathbf{r}}_{\alpha\beta}}) [(\overline{\mathbf{P}^E \cdot \mathbf{S}_\alpha}) : \hat{\mathbf{r}}_{\alpha\beta} \hat{\mathbf{r}}_{\alpha\beta}] \right\}. \end{aligned} \quad (3.10)$$

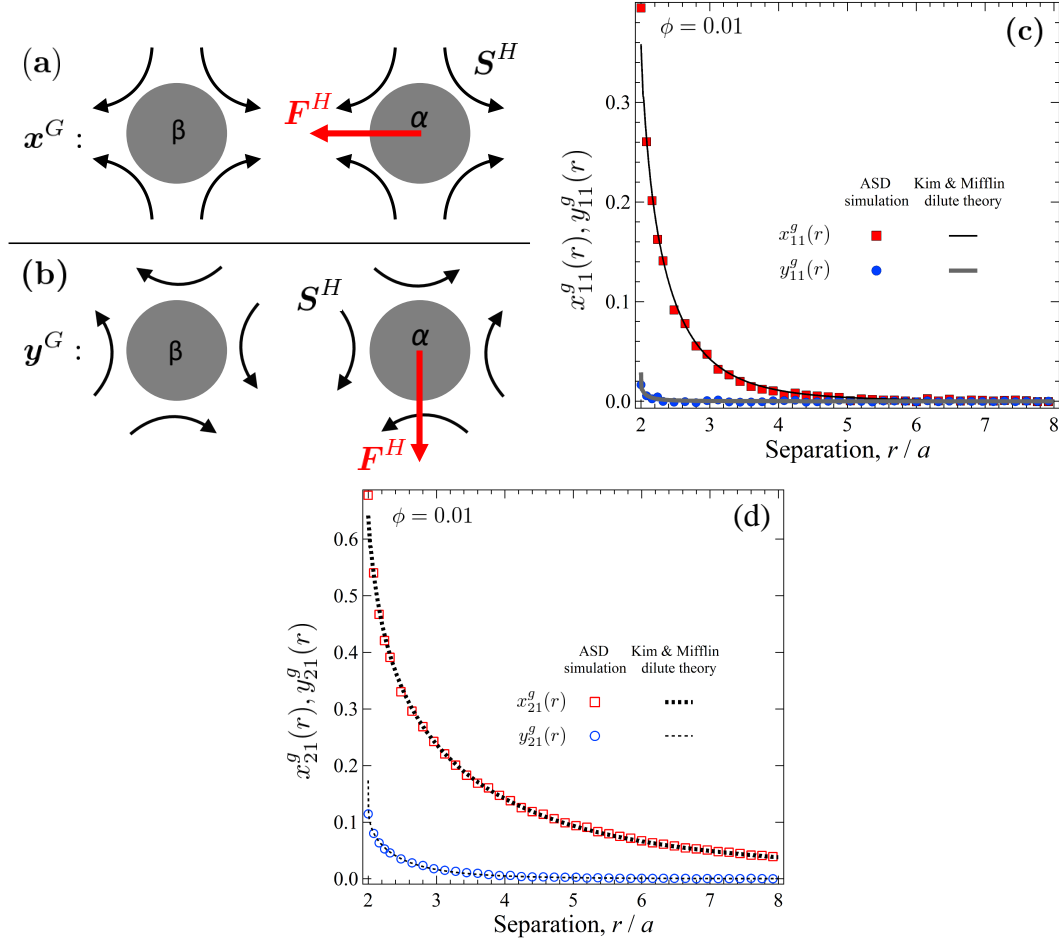


Figure 3.1: Longitudinal and transverse mobility coefficients coupling hydrodynamic stresslet, S^H , on the surface of a particle to the hydrodynamic force, \mathbf{F}^H , of that and other particles. (a) Profile of longitudinal coupling, x^g . (b) Profile of transverse coupling, y^g . (c) Self mobility coefficients, x_{11}^g and y_{11}^g ; (d) Pair mobility coefficients, x_{21}^g and y_{21}^g . Lines: dilute theory of Kim and Mifflin [89]. Symbols: simulation results from present study for volume fraction $\phi = 0.01$. From [136], with permission.

The transverse coefficients, y_{11}^g and y_{21}^g , can be obtained following a similar procedure by projecting the coupling onto the transverse subspace. Utilizing the same method as for the parallel coefficients, we compute these transverse coefficients and those of the remaining couplings, which are given in the Appendix.

The coefficients are averaged over all pairs within a radial bin of width of $a/50$, and is repeated for 30 configurations. For each configuration, 50 sets of

different random forces are applied. We take into account pair separations up to $r/a = 8$, as this recovers the relevant physics in the problem at a moderate computational cost.

3.4 Results

In this section, we present the concentration-dependent mobility coefficients in Equations (3.4), (3.12), and (3.14), as computed via Equations (3.9), (3.10), (3.23), (3.24), (3.27), (3.28), (3.30), (3.31), (3.32), for suspensions at volume fractions ranging from $0.01 \leq \phi \leq 0.5$. We begin with the stresslet-force coupling $\mathbf{g}_{\alpha\beta}$. The coefficients $x_{\alpha\beta}^s(r, \phi)$ and $y_{\alpha\beta}^s(r, \phi)$ give the strength of the hydrodynamic stresslet \mathbf{S}^H induced on the surface of particle α by a disturbance flow arising from the hydrodynamic force on the surface of particle β , where \mathbf{S}^H is the symmetric first moment of the traction. A hydrodynamic force on the surface of an isolated particle in a solvent produces no stresslet on its own surface because the Stokes drag on an isolated hard sphere is constant over its surface. In the presence of a second particle, the hydrodynamic coupling between the pair produces a disturbance flow that induces a stresslet on the forced particle, a consequence of its inability to deform. This coupling is illustrated in Figure 3.1(a) and 3.1(b) for a hydrodynamic force acting along and transverse to the line of centers of the pair, respectively.

The coefficient x^s describes the coupling between stresslet and force on a pair of particles when the hydrodynamic force acts along the line of centers, and is represented by the curved lines in Figure 3.1(a). Physically, if particle β is located downstream along the direction of the external force on particle

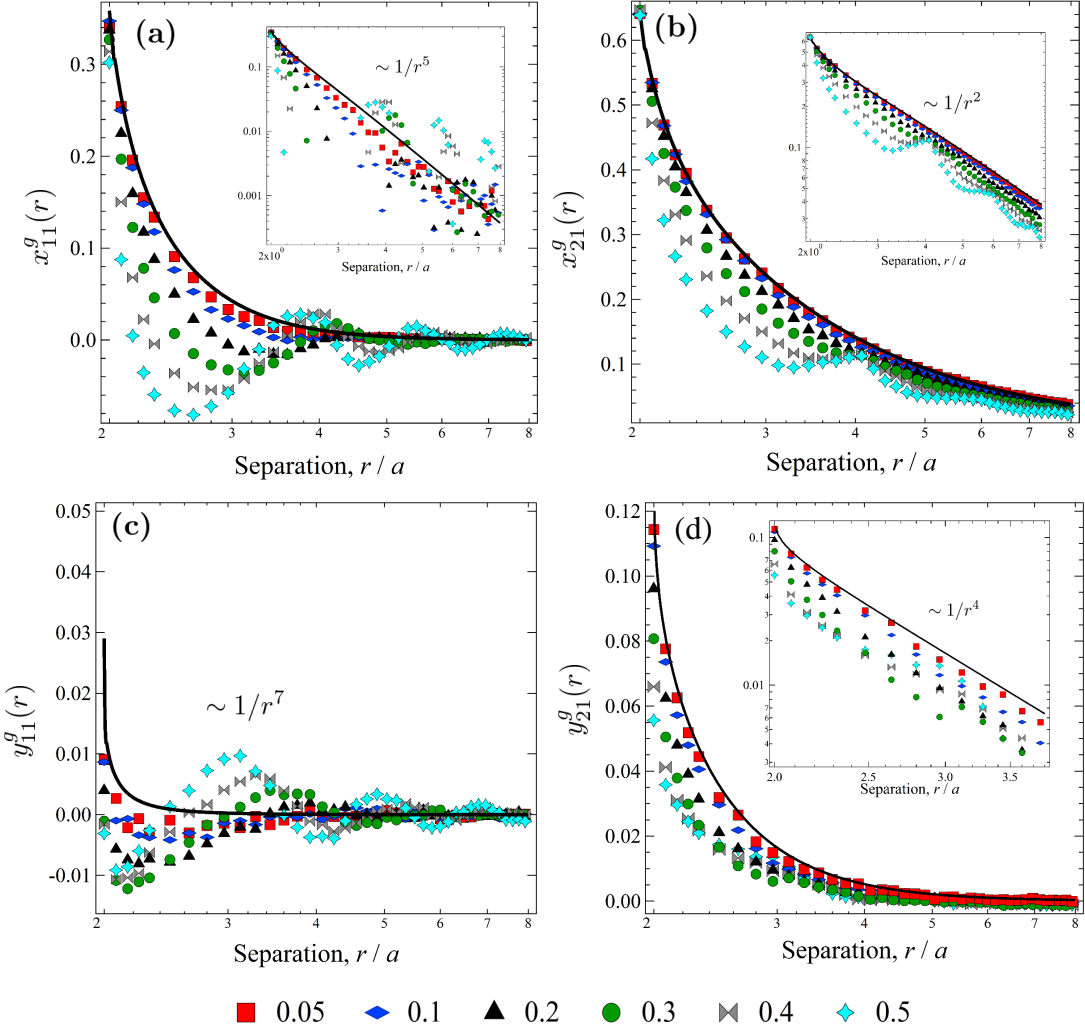


Figure 3.2: Longitudinal and transverse mobility coefficients coupling stresslet on the surface of a particle to the force of that and other particles, in a concentrated suspension. Solid lines: dilute theory of Kim and Mifflin [89]. Symbols: simulation results from present study for volume fractions as shown in legend. (a) Longitudinal self-mobility. (b) Longitudinal pair-mobility. (c) Transverse self-mobility. (d) Transverse pair-mobility. The inset of the figures are the log-log plots of the couplings, indicating the decay rate holds as concentration increases. The log-log plot of transverse self-mobility is not shown because the couplings fluctuate around zero. From [136], with permission.

α , the fluid field is disturbed by the finite size of particle β . The distortion to fluid streamlines would tend to elongate a deformable particle along the line of centers; a stresslet will arise on any particle more rigid than the fluid. These

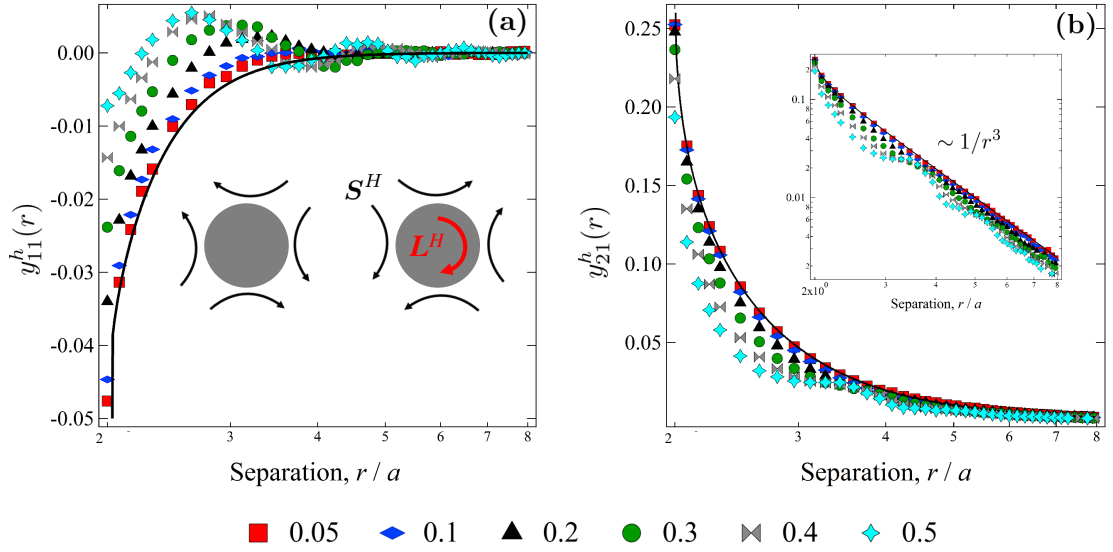


Figure 3.3: Transverse mobility coefficients coupling stresslet on the surface of a particle to the torque of that and other particles, in a concentrated suspension. Solid lines: dilute theory of Kim and Mifflin [89]. Symbols: simulation results from present study for volume fractions as shown in legend. (a) Transverse self-mobility. (b) Transverse pair-mobility. The inset of (a) represents the profile of the couplings. The inset of (b) shows the log-log plot of transverse pair-mobility, indicating the decay rate holds as concentration increases. From [136], with permission.

interactions reflect back and forth ad infinitum.

The coefficient y^g corresponds to the stresslet that arises from a force acting transverse to the line of centers, as shown in Figure 3.1(b). The disturbance flow decays with distance from particle α , and is thus stronger on the portions of the surface of particle β that are closer to particle α . In consequence, the hydrodynamic traction varies with position on the surface of particle β , tending to elongate a deformable particle along the direction shown.

The symmetry of the grand coupling matrix in Equation (3.2) demands that the stresslet-force coupling, $\mathbf{g}_{\alpha\beta}$, is symmetric to the velocity-strain rate coupling, $\tilde{\mathbf{g}}_{ijk}^{\alpha\beta} = \mathbf{g}_{jki}^{\alpha\beta}$. Thus, once the stresslet-to-force coupling is computed, the

velocity-to-strain rate coupling is known.

To test the validity of this method, we compare theory results for isolated pairs [89] to simulation results at concentration $\phi = 0.01$ obtained in this study (Figure 3.1(c-d)). The solid and dashed lines represent the coefficients $x_{\alpha\beta}^g(r, \phi \rightarrow 0)$ and $y_{\alpha\beta}^g(r, \phi \rightarrow 0)$ for isolated pairs, respectively. In both plots, the strength of the coupling is most pronounced at contact. For the self-coupling, the longitudinal and transverse components decay as $1/r^5$ and $1/r^7$, respectively. Simulation results from the present study for $\phi = 0.01$ are also plotted in Figure 3.1(c-d) (filled and open symbols). The agreement between simulation and theory is excellent, demonstrating the accuracy of the simulation method at the pair level.

To examine the effect of concentration on the pair couplings, the suspension concentration is increased, spanning the range $0.05 \leq \phi \leq 0.5$. The resulting self- and pair coefficients are plotted in Figure 3.2 for the longitudinal (x^g) and transverse (y^g) couplings (symbols), alongside the dilute theory of Kim and Mifflin [89] (solid lines). The qualitative algebraic decay appears unaffected by many-body hydrodynamic interactions (as shown by the log-log plots at the inset of Figure 3.2), but as concentration becomes high, undulations in the curves suggest the emergence of local structure. Recall that a positive longitudinal coupling, $x^{\alpha\beta}$, indicates that particle α has the tendency to elongate along the line of centers, as shown in Figure 3.1. Thus for longitudinal couplings with an arbitrary concentration (Figure 3.2(a-b)), where the curves cross above the dilute theory, the coupling tends to produce stronger deformation, toward a prolate shape along the line of centers. Where the curves fall below it, this effect is weakened. Negative values indicate a tendency to form an oblate spheroid.

The former appears at separations that permit an integer number of intervening particles; the latter occurs for non-integer numbers of intervening particles.

This behavior can be understood as follows. When the separation between a pair is just large enough to fit another particle ($r = 4a$), the disturbance is transmitted by thin fluid gap, essentially a near-contact interaction. Particles thus tend to deform along the line of centers. However, when the separation between a pair is not large enough to fully fit another particle, the larger volume of intervening fluid permits greater decay of the fluid disturbance between the pair. These lubrication forces tend to compress the shape of particles along the line of centers. At higher concentration, this effect becomes more dominant than the near-contact effect, and leads to a tendency to deform transversely to the line of centers. The sign change signals that this transition emerges at $\phi \approx 0.2$.

The transverse coupling shows the opposite trend (Figure 3.2(c-d)): at the separation just sufficient to fit another particle, the couplings relax. Here, the hydrodynamic force is transverse to the line of centers, and so the lubrication force which connects the three particles tends to pull particles together, i.e., inducing a tensile traction transverse to the direction of the hydrodynamic force, thus relaxing the coupling. However, when the separation excludes another particle, the lubrication force from the surrounding particles enhances the coupling. As shown in Figure 3.2(c-d), a separation distance $r \approx 3$ corresponds to the first occurrence where the separation excludes another particle, manifesting in a peak. As $r \rightarrow 4a$, there is just enough intervening space between the pair to fit another particle, resulting in a decrease in the strength of the coupling. For larger separation, the evolution of the coupling follows this pattern and repeats.

Though concentration variations cause these liquid-like structural behav-

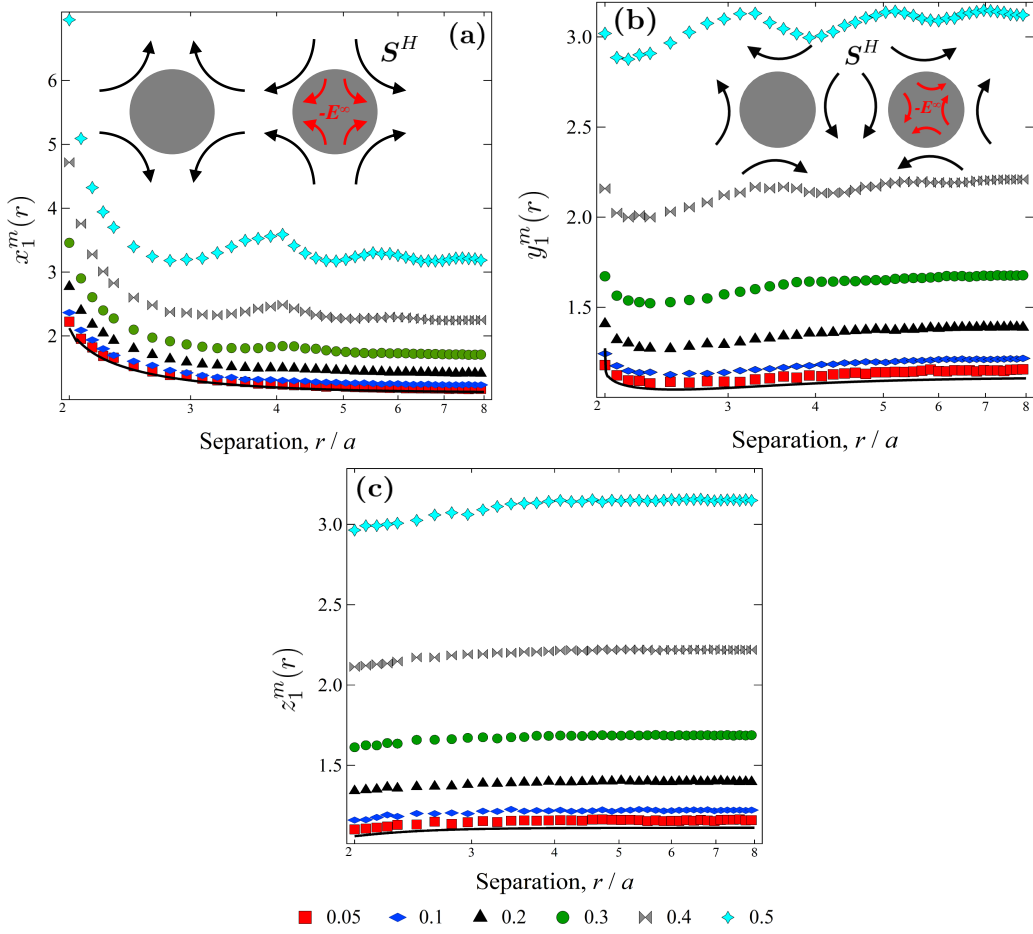


Figure 3.4: Longitudinal, transverse and perpendicular mobility coefficients coupling stresslet on the surface of a particle to the strain of that and other particles, in a concentrated suspension. Solid lines: dilute theory of Kim and Mifflin [89]. Symbols: simulation results from present study for volume fractions as shown in legend. (a) Longitudinal mobility. (b) Transverse mobility. (c) Perpendicular mobility. The insets of (a) and (b) represent the profile of longitudinal and transverse couplings, respectively. From [136], with permission.

iors, the scalings of the decay of these functions are the same as those in dilute theory, consistent with the conclusion of Zia et al. [150]. Hydrodynamic interactions are not screened, but can be accounted for utilizing the mobility data presented here.

We now move on to study the strength of the couplings between stresslet on one particle and hydrodynamic torque on another particle, $\mathbf{h}_{\alpha\beta}$, viz.,

$$\mathbf{S}_\alpha = \mathbf{h}_{\alpha\beta} \cdot \mathbf{L}_\beta. \quad (3.11)$$

The coupling is a third-rank tensor and can be projected onto the corresponding subspaces, giving

$$h_{ijk}^{\alpha\beta} = y_{\alpha\beta}^h(r, \phi)(\hat{r}_i \epsilon_{jkl} \hat{r}_l + \hat{r}_j \epsilon_{ikl} \hat{r}_l). \quad (3.12)$$

Here ϵ is the third-rank Levi-Civita tensor. The coefficient $y_{\alpha\beta}^h(r, \phi)$ gives the strength of the coupling transverse to the line of centers, and the superscript h signifies the stresslet-torque coupling. When the torque points along the line of centers, the hydrodynamic force on the surface of both particles is zero and produces no stresslet; thus the parallel component for the stresslet-torque coupling disappears. Similar to the coupling between stresslet and force, the symmetry of the grand mobility tensor gives $\tilde{h}_{ijk}^{\alpha\beta} = h_{jki}^{\alpha\beta}$.

The couplings between stresslet and torque for concentrations from dilute to concentrated are shown in Figure 3.3. The dilute theory (solid lines) and dilute simulations show excellent agreement. The transverse pair coupling $y_{21}^h(r)$ decays as $1/r^3$ and the transverse self coupling $y_{11}^h(r)$ decays as $1/r^6$. The pair coupling is set by the first reflection of the rotation of particle α while the self coupling is set by the second reflection back from the disturbance of particle β , thus giving the more rapid decay of the latter. In the far field, the couplings decay to zero. A sketch of the stresslet arising from an external torque is shown by the inset of Figure 3.3(a). The origin of this stresslet is similar to that of y^g , where the strength of the traction from the disturbance flow is non-uniform over particle surfaces, producing a tendency of the fluid to deform a soft particle or produce a stresslet on a rigid particle.

In concentrated suspensions, undulations appear, again suggesting local structure. At separations where a third particle can be fit between the pair, the magnitude of the self- and pair- couplings increases because the third particle replaces the fluid gap, strengthening the entrainment.

Finally, the strength of the couplings between stresslet on one particle and the flow rate of strain at the center of another particle is $\mathbf{m}_{\alpha\beta}$,

$$\mathbf{S}_\alpha = \mathbf{m}_{\alpha\beta} \cdot \mathbf{E}_\beta. \quad (3.13)$$

Physically, an imposed flow rate of strain exerted on the particle pairs tends to deform soft particles, producing a stresslet on the surface of rigid particles. This coupling is a fourth-rank tensor which is expressed as

$$\begin{aligned} m_{ijkl}^{\alpha\beta} = & \frac{3}{2} x_{\alpha\beta}^m (\hat{r}_i \hat{r}_j - \frac{1}{3} \delta_{ij}) (\hat{r}_k \hat{r}_l - \frac{1}{3} \delta_{kl}) \\ & + \frac{1}{2} y_{\alpha\beta}^m (\hat{r}_i \delta_{jl} \hat{r}_k + \hat{r}_j \delta_{il} \hat{r}_k + \hat{r}_i \delta_{jk} \hat{r}_l + \hat{r}_j \delta_{ik} \hat{r}_l \\ & + \hat{r}_j \delta_{ik} \hat{r}_l - 4 \hat{r}_i \hat{r}_j \hat{r}_k \hat{r}_l) + \frac{1}{2} z_{\alpha\beta}^m (\delta_{ik} \delta_{jl} + \delta_{jk} \delta_{il} \\ & - \delta_{ij} \delta_{kl} + \hat{r}_i \hat{r}_j \delta_{kl} + \delta_{ij} \hat{r}_k \hat{r}_l + \hat{r}_i \hat{r}_j \hat{r}_k \hat{r}_l \\ & - \hat{r}_i \delta_{jl} \hat{r}_k - \hat{r}_j \delta_{il} \hat{r}_k - \hat{r}_i \delta_{jk} \hat{r}_l - \hat{r}_j \delta_{ik} \hat{r}_l). \end{aligned} \quad (3.14)$$

The coefficients $x_{\alpha\beta}^m$, $y_{\alpha\beta}^m$ and $z_{\alpha\beta}^m$ give the strength of the coupling along, transverse to and perpendicular to the line of centers, respectively [83]. The superscript m signifies the stresslet-strain rate coupling. The particles are rigid, thus the strain rate of the particles is always zero. Since in many problems the flow is uniform, which means the particle pairs are disturbed by the same flow strain rate, the influence of self- and pair- couplings can be considered together and lead to the definition of Kim and Karrila [88], which sum the self- and pair-

couplings together, i.e.,

$$\begin{aligned} x_1^m &= x_{11}^m + x_{12}^m, \\ y_1^m &= y_{11}^m + y_{12}^m, \\ z_1^m &= z_{11}^m + z_{12}^m. \end{aligned} \tag{3.15}$$

Figure 3.4 shows the corresponding couplings as functions of volume fraction and separation distance for suspensions from dilute to concentrated, where the profile of the straining motion in the parallel and transverse direction and the resultant stresslet for a pair of particles is illustrated in the inset of Figures 3.4(a-b). For the parallel coupling x^m , the straining flow along the line of centers on particle α produces a disturbance flow that tends to elongate particle β transverse to the line of centers. Consequently, a corresponding stresslet (inset of Figure 3.4(a)) is induced on the surface of the second particle. The transverse coupling y^m that the straining flow oriented transverse to the line of centers on the first particle will lead to a mirror profile stresslet on the second particle. The parallel and transverse couplings decay as $1/r^3$, while the perpendicular coupling decays as $1/r^5$. In the far field, coupling decays to that of an isolated particle in a straining flow with a constant stresslet on its surface.

The stresslet-to-strain coupling describes the strength of the traction moment induced by the flow strain, and increases with particle concentration. One might expect that a higher concentration of particles hinders particle motion more, and thus weakens entrainment. However for m , a higher concentration gives rise to a stronger coupling. This is because in the presence of flow strain, a high concentration introduces more particle interactions.

Finally, undulations can again be observed in the parallel and transverse mobilities, but not for z^m (Figure 3.4(c)). For parallel and transverse couplings,

the straining flow and the resulting stresslet lie on the same plane as the line of centers (see inset of Figure 3.4(a-b)). Pair interactions act within this plane; the structure between the pair of particles along the line of centers significantly influences the resulting disturbance flow. However, for the perpendicular coupling, a uniform straining flow acts in the plane perpendicular to the line of centers and gives rise to a corresponding stresslet in this plane. Pair interactions again transmit through the perpendicular plane, and thus the coupling stays in a subspace with no component on the plane of parallel and transverse couplings. Intervening particles located along the line of centers cannot disturb the perpendicular couplings, giving rise to no undulations.

The couplings to the stresslet are essential to calculating rheological quantities in colloidal suspensions such as the viscosity, normal stresses and osmotic pressure. The concentrated mobility functions derived here will permit analytical computation of these quantities for concentrated (near) equilibrium suspensions, a task that typically requires computational modeling or mean-field approximation. To demonstrate this utility, here we compute the high-frequency viscosity for suspensions with volume fraction $0.01 \leq \phi \leq 0.5$. The high-frequency viscosity, η'_∞ , is the “intrinsic” viscosity of a suspension arising from the presence of the no-slip surfaces of the particles. In the context of sheared suspensions, it is the flow-independent, off-diagonal particle-phase shear stress, Σ_{xy}^p , normalized by the flow rate E_{xy} , and solvent viscosity η ,

$$\eta'_\infty = \frac{\Sigma_{xy}^p}{2\eta E_{xy}}. \quad (3.16)$$

The bulk stress of a dilute suspension of hard spheres undergoing simple shear

was given by Batchelor and Green [18]:

$$\begin{aligned}\Sigma^p = & 2\eta E \left(\frac{5}{2}\phi + \frac{5}{2}\phi^2 + \right. \\ & \left. \frac{15}{2}\phi^2 \int_2^\infty (K(r) + \frac{2}{3}L(r) + \frac{2}{15}M(r))g^{eq}(r)r^2 dr \right),\end{aligned}\quad (3.17)$$

where K , L , and M are linear combinations of the hydrodynamic coefficients of the stresslet-strain coupling, \mathbf{m} , and $g^{eq}(r)$ is the equilibrium pair distribution function.

However, these functions have thus far only been derived for dilute suspensions. Here we extend Batchelor's theory to finite concentration by defining volume-fraction dependent forms of K , L , and M as

$$K(r, \phi) = z_1^m(r, \phi) - z_1^{m,0}(\phi), \quad (3.18)$$

$$L(r, \phi) = (y_1^m(r, \phi) - z_1^m(r, \phi)) - (y_1^{m,0}(\phi) - z_1^{m,0}(\phi)), \quad (3.19)$$

$$\begin{aligned}M(r, \phi) = & (\frac{3}{2}x_1^m(r, \phi) - 2y_1^m(r, \phi) + \frac{1}{2}z_1^m(r, \phi)) \\ & - (\frac{3}{2}x_1^{m,0}(\phi) - 2y_1^{m,0}(\phi) + \frac{1}{2}z_1^{m,0}(\phi)).\end{aligned}\quad (3.20)$$

The coefficients $x_1^{m,0}$, $y_1^{m,0}$ and $z_1^{m,0}$ provide a re-normalization for convergence [18], and are equivalent to the far-field (constant) value of x_1^m , y_1^m and z_1^m . Insertion of these expressions into Equation (3.17) gives the volume-fraction dependent high-frequency viscosity:

$$\begin{aligned}\eta'_\infty(\phi) = & \frac{5}{2}\kappa(\phi)\phi + \frac{5}{2}\kappa(\phi)\phi^2 + \\ & \frac{15}{2}\phi^2 \int_2^\infty (K(r, \phi) + \frac{2}{3}L(r, \phi) + \frac{2}{15}M(r, \phi))g^{eq}(r, \phi)r^2 dr.\end{aligned}\quad (3.21)$$

Here, the pair distribution function g^{eq} also depends on volume fraction, ϕ , and radial separation, r , and can either be calculated from Percus-Yevick equation [122] or measured directly from simulation (Figure 5). The coefficient $\kappa(\phi)$, which is a combination of $x_1^{m,0}$, $y_1^{m,0}$ and $z_1^{m,0}$, arises from the renormalization of

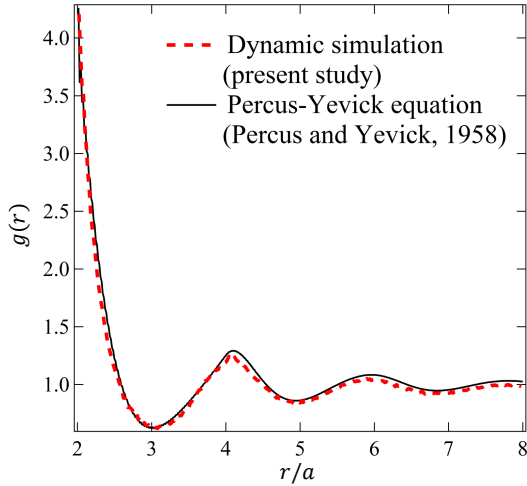


Figure 3.5: Pair distribution function $g(r)$, as a function of distance from particle center, r , for volume fraction $\phi = 0.45$. The solid line is the theoretical results calculated from Percus-Yevick equation [122]. The dash line is the measurement from our simulation. From [136], with permission.

the integration in Equation (3.21). Physically, an isolated sphere under straining flow develops a hydrodynamic stresslet on its surface, $\mathbf{S}^H(\phi \rightarrow 0) = 20\pi a^3 \eta E/3$. For arbitrary concentration, the isolated sphere is suspended in a medium of bath particles, and its effective stresslet is given by $\mathbf{S}^H(\phi) = 20\pi a^3 \eta \kappa(\phi) E/3$, which is equivalent to a sphere suspended in a solvent of viscosity $\kappa(\phi)\eta$. Figure 6 shows the high-frequency viscosity thus obtained, utilizing the concentrated stresslet-strain coupling \mathbf{m} and Equation (3.21). The results (symbols) are shown alongside the results from dynamic simulations via Sierou and Brady [133] (line); agreement is excellent.

3.5 Summary and Conclusions

We have extended our theoretical and computational approach, based on the Accelerated Stokesian Dynamics algorithm, to measure the concentration-

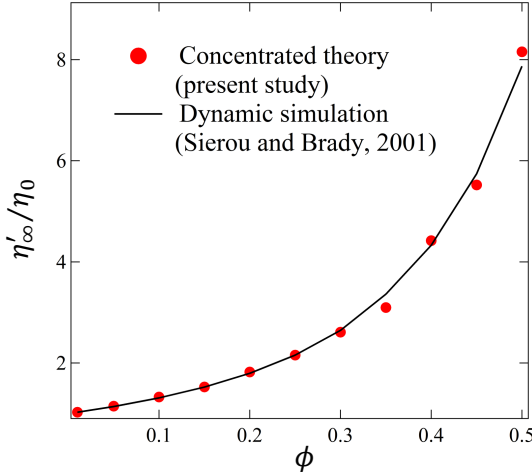


Figure 3.6: High-frequency viscosity as a function of volume fraction. The symbols are from evaluating Equation (3.21) utilizing the concentrated mobility function $\mathbf{m}(r, \phi)$. The solid line is the result of dynamic simulations from Sierou and Brady [133]. From [136], with permission.

dependent hydrodynamic mobility functions coupling the surface traction of one particle to forcing and straining motion of a second particle, with a view toward developing a set of hydrodynamic pair-mobility functions analogous to the dilute functions of Kim and Mifflin [89], but now for arbitrary suspension concentration. In our previous work [150], we showed that hydrodynamic interactions do not screen entrained motion in suspensions of freely diffusing particles, regardless of the concentration. In the present work, our finding again indicate no change in the algebraic decay of pair interactions in the presence of an intervening medium, but do reveal a concentration dependence important for calculations involving particle interactions.

The couplings computed in the present and recent articles together constitute a set of orthogonal coupling functions which may now be used in a pair-like Smoluchowski equation governing many-body hydrodynamically interacting particles. The presented mobility functions are derived assuming a homogeneous and isotropic hard-sphere suspension. Because these functions

are only volume-fraction and configuration dependent, they take on exactly the same form in equilibrium suspensions where additional microscopic forces change configuration, i.e., electrostatic potentials. Although the assumption of an isotropic suspension formally restricts attention to weak flow, we have begun evaluating their applicability to flowing suspensions.

Our technique can be easily extended to compute mobility functions for other particle-surface boundary conditions, by modifying the mobility functions for e.g. slip conditions or flux conditions for permeable particles, for example. Our method can also be utilized to compute particle mobilities in bounded systems [3, 5].

3.6 Appendix: Evaluation of the hydrodynamic coefficients

To get the transverse component of $\mathbf{g}_{\alpha\beta}$, we triple dot $(\hat{\mathbf{r}}_i \delta_{jk} + \hat{\mathbf{r}}_j \delta_{ik} - 2\hat{\mathbf{r}}_i \hat{\mathbf{r}}_j \hat{\mathbf{r}}_k)$ to both sides of Equation 3.4 and plug Equations (3.5) and (3.6) into the formula, obtaining

$$\begin{aligned}
 y_{\alpha\beta}^g &= \frac{1}{4} g_{kij}^{\alpha\beta} (\hat{\mathbf{r}}_i \delta_{jk} + \hat{\mathbf{r}}_j \delta_{ik} - 2\hat{\mathbf{r}}_i \hat{\mathbf{r}}_j \hat{\mathbf{r}}_k) \\
 &= \frac{1}{4} U_k^\alpha E_l^\beta P_{lij}^E (\hat{\mathbf{r}}_i \delta_{jk} + \hat{\mathbf{r}}_j \delta_{ik} - 2\hat{\mathbf{r}}_i \hat{\mathbf{r}}_j \hat{\mathbf{r}}_k) \\
 &= \frac{1}{4} \{(\mathbf{E}^\beta \cdot \mathbf{P}^E) : (\mathbf{U}^\alpha \hat{\mathbf{r}}_{\alpha\beta}) \\
 &\quad + (\mathbf{E}^\beta \cdot \mathbf{P}^E) : (\hat{\mathbf{r}}_{\alpha\beta} \mathbf{U}^\alpha) - \frac{4}{3} x_{\alpha\beta}^G \}
 \end{aligned} \tag{3.22}$$

i.e.,

$$\begin{aligned} y_{11}^g = & \frac{1}{8} \{ (\mathbf{E}^\alpha \cdot \mathbf{P}^E) : (\mathbf{U}^\alpha \hat{\mathbf{r}}_{\alpha\beta}) + (\mathbf{E}^\alpha \cdot \mathbf{P}^E) : (\hat{\mathbf{r}}_{\alpha\beta} \mathbf{U}^\alpha) \\ & - (\mathbf{E}^\beta \cdot \mathbf{P}^E) : (\mathbf{U}^\beta \hat{\mathbf{r}}_{\alpha\beta}) \\ & - (\mathbf{E}^\beta \cdot \mathbf{P}^E) : (\hat{\mathbf{r}}_{\alpha\beta} \mathbf{U}^\beta) - \frac{8}{3} x_{\alpha\alpha}^G \} \end{aligned} \quad (3.23)$$

$$\begin{aligned} y_{12}^g = & \frac{1}{8} \{ (\mathbf{E}^\beta \cdot \mathbf{P}^E) : (\mathbf{U}^\alpha \hat{\mathbf{r}}_{\alpha\beta}) + (\mathbf{E}^\beta \cdot \mathbf{P}^E) : (\hat{\mathbf{r}}_{\alpha\beta} \mathbf{U}^\alpha) \\ & - (\mathbf{E}^\alpha \cdot \mathbf{P}^E) : (\mathbf{U}^\beta \hat{\mathbf{r}}_{\alpha\beta}) \\ & - (\mathbf{E}^\alpha \cdot \mathbf{P}^E) : (\hat{\mathbf{r}}_{\alpha\beta} \mathbf{U}^\beta) - \frac{8}{3} x_{\alpha\beta}^G \} \end{aligned} \quad (3.24)$$

The transverse component of $\mathbf{h}_{\alpha\beta}$ is obtained by double dot $\boldsymbol{\varepsilon}$ to both side of Equation (3.12),

$$\begin{aligned} \boldsymbol{\varepsilon}_{jkm} g_{ijk}^{\alpha\beta} &= y_{\alpha\beta}^h (\hat{r}_i \hat{r}_l \boldsymbol{\varepsilon}_{jkl} \boldsymbol{\varepsilon}_{jkm} + \hat{r}_j \hat{r}_l \boldsymbol{\varepsilon}_{kil} \boldsymbol{\varepsilon}_{kjm}) \\ &= y_{\alpha\beta}^h [2\hat{r}_i \hat{r}_l \delta_{lm} + \hat{r}_j \hat{r}_l (\delta_{ij} \delta_{lm} - \delta_{im} \delta_{lj})] \\ &= y_{\alpha\beta}^h (3\hat{r}_i \hat{r}_m - \delta_{im}). \end{aligned} \quad (3.25)$$

Then double dot $\hat{r}_i \hat{r}_m$ to both sides,

$$\begin{aligned} y_{\alpha\beta}^h &= \frac{1}{2} \boldsymbol{\varepsilon}_{jkm} h_{ijk}^{\alpha\beta} \hat{r}_i \hat{r}_m \\ &= \frac{1}{2} \boldsymbol{\varepsilon}_{jkm} \tilde{h}_{kj}^{\alpha\beta} \hat{r}_i \hat{r}_m \\ &= \frac{1}{2} \boldsymbol{\varepsilon}_{jkm} \tilde{h}_{kl}^{\alpha\beta} P_{lij}^E \hat{r}_i \hat{r}_m \\ &= \frac{1}{2} \boldsymbol{\varepsilon}_{jkm} \Omega_k^\alpha E_l^\beta P_{lij}^E \hat{r}_i \hat{r}_m \\ &= \frac{1}{2} (\mathbf{E}^\beta \cdot \mathbf{P}^E) : [(\boldsymbol{\Omega}^\alpha \times \hat{\mathbf{r}}_{\alpha\beta}) \hat{\mathbf{r}}_{\alpha\beta}] \end{aligned} \quad (3.26)$$

Thus,

$$y_{11}^h = \frac{1}{4} \{ (\mathbf{E}^\alpha \cdot \mathbf{P}^E) : [(\boldsymbol{\Omega}^\alpha \times \hat{\mathbf{r}}_{\alpha\beta}) \hat{\mathbf{r}}_{\alpha\beta}] \\ + (\mathbf{E}^\beta \cdot \mathbf{P}^E) : [(\boldsymbol{\Omega}^\beta \times \hat{\mathbf{r}}_{\alpha\beta}) \hat{\mathbf{r}}_{\alpha\beta}] \}. \quad (3.27)$$

$$y_{12}^h = \frac{1}{4} \{ (\mathbf{E}^\beta \cdot \mathbf{P}^E) : [(\boldsymbol{\Omega}^\alpha \times \hat{\mathbf{r}}_{\alpha\beta}) \hat{\mathbf{r}}_{\alpha\beta}] \\ + (\mathbf{E}^\alpha \cdot \mathbf{P}^E) : [(\boldsymbol{\Omega}^\beta \times \hat{\mathbf{r}}_{\alpha\beta}) \hat{\mathbf{r}}_{\alpha\beta}] \}. \quad (3.28)$$

To get the hydrodynamic coefficients for $\mathbf{m}_{\alpha\beta}$, an extra third-rank mapping tensor \mathbf{P}^{S-1} is also involved to convert the simplified second-rank mobility to its origin, the fourth-rank mobility,

$$m_{nmkl} = P_{nmi}^{S-1} m_{ij} P_{jkl}^E. \quad (3.29)$$

By respectively quartic dot the subspace tensor onto $\mathbf{m}_{\alpha\beta}$, the three hydrodynamic coefficients are given as

$$x_1^m = \frac{3}{4} \{ [(\mathbf{P}^{S-1} \cdot \mathbf{S}^\alpha) : (\hat{\mathbf{r}}_{\alpha\beta} \hat{\mathbf{r}}_{\alpha\beta})] [(\mathbf{E}^\alpha \cdot \mathbf{P}^E) : (\hat{\mathbf{r}}_{\alpha\beta} \hat{\mathbf{r}}_{\alpha\beta})] \\ + [(\mathbf{P}^{S-1} \cdot \mathbf{S}^\beta) : (\hat{\mathbf{r}}_{\alpha\beta} \hat{\mathbf{r}}_{\alpha\beta})] [(\mathbf{E}^\beta \cdot \mathbf{P}^E) : (\hat{\mathbf{r}}_{\alpha\beta} \hat{\mathbf{r}}_{\alpha\beta})] \\ + [(\mathbf{P}^{S-1} \cdot \mathbf{S}^\alpha) : (\hat{\mathbf{r}}_{\alpha\beta} \hat{\mathbf{r}}_{\alpha\beta})] [(\mathbf{E}^\beta \cdot \mathbf{P}^E) : (\hat{\mathbf{r}}_{\alpha\beta} \hat{\mathbf{r}}_{\alpha\beta})] \\ + [(\mathbf{P}^{S-1} \cdot \mathbf{S}^\beta) : (\hat{\mathbf{r}}_{\alpha\beta} \hat{\mathbf{r}}_{\alpha\beta})] [(\mathbf{E}^\alpha \cdot \mathbf{P}^E) : (\hat{\mathbf{r}}_{\alpha\beta} \hat{\mathbf{r}}_{\alpha\beta})] \}. \quad (3.30)$$

$$y_1^m = \frac{1}{8} \{ 4[\hat{\mathbf{r}}_{\alpha\beta} \cdot (\mathbf{P}^{S-1} \cdot \mathbf{S}^\alpha)] \cdot [\hat{\mathbf{r}}_{\alpha\beta} \cdot (\mathbf{E}^\alpha \cdot \mathbf{P}^E)] \\ + 4[\hat{\mathbf{r}}_{\alpha\beta} \cdot (\mathbf{P}^{S-1} \cdot \mathbf{S}^\beta)] \cdot [\hat{\mathbf{r}}_{\alpha\beta} \cdot (\mathbf{E}^\beta \cdot \mathbf{P}^E)] \\ + 4[\hat{\mathbf{r}}_{\alpha\beta} \cdot (\mathbf{P}^{S-1} \cdot \mathbf{S}^\alpha)] \cdot [\hat{\mathbf{r}}_{\alpha\beta} \cdot (\mathbf{E}^\beta \cdot \mathbf{P}^E)] \\ + 4[\hat{\mathbf{r}}_{\alpha\beta} \cdot (\mathbf{P}^{S-1} \cdot \mathbf{S}^\beta)] \cdot [\hat{\mathbf{r}}_{\alpha\beta} \cdot (\mathbf{E}^\alpha \cdot \mathbf{P}^E)] - \frac{16}{3} x_1^m \}. \quad (3.31)$$

$$\begin{aligned}
z_1^m = & \frac{1}{8} \left\{ 2 \{ [(\mathbf{P}^{S-1} \cdot \mathbf{S}^\alpha) : (\mathbf{E}^\alpha \cdot \mathbf{P}^E)] \right. \\
& + [(\mathbf{P}^{S-1} \cdot \mathbf{S}^\beta) : (\mathbf{E}^\beta \cdot \mathbf{P}^E)] \\
& + [(\mathbf{P}^{S-1} \cdot \mathbf{S}^\alpha) : (\mathbf{E}^\beta \cdot \mathbf{P}^E)] \\
& + [(\mathbf{P}^{S-1} \cdot \mathbf{S}^\beta) : (\mathbf{E}^\alpha \cdot \mathbf{P}^E)] \} \\
& - \{ [(\mathbf{P}^{S-1} \cdot \mathbf{S}^\alpha) : \mathbf{I}] [(\mathbf{E}^\alpha \cdot \mathbf{P}^E) : \mathbf{I}] \\
& + [(\mathbf{P}^{S-1} \cdot \mathbf{S}^\beta) : \mathbf{I}] [(\mathbf{E}^\beta \cdot \mathbf{P}^E) : \mathbf{I}] \\
& + [(\mathbf{P}^{S-1} \cdot \mathbf{S}^\alpha) : \mathbf{I}] [(\mathbf{E}^\beta \cdot \mathbf{P}^E) : \mathbf{I}] \\
& + [(\mathbf{P}^{S-1} \cdot \mathbf{S}^\beta) : \mathbf{I}] [(\mathbf{E}^\alpha \cdot \mathbf{P}^E) : \mathbf{I}] \} \\
& + \{ [(\mathbf{P}^{S-1} \cdot \mathbf{S}^\alpha) : \mathbf{I}] [(\mathbf{E}^\alpha \cdot \mathbf{P}^E) : \hat{\mathbf{r}}_{\alpha\beta} \hat{\mathbf{r}}_{\alpha\beta}] \\
& + [(\mathbf{P}^{S-1} \cdot \mathbf{S}^\beta) : \mathbf{I}] [(\mathbf{E}^\beta \cdot \mathbf{P}^E) : \hat{\mathbf{r}}_{\alpha\beta} \hat{\mathbf{r}}_{\alpha\beta}] \\
& + [(\mathbf{P}^{S-1} \cdot \mathbf{S}^\alpha) : \mathbf{I}] [(\mathbf{E}^\beta \cdot \mathbf{P}^E) : \hat{\mathbf{r}}_{\alpha\beta} \hat{\mathbf{r}}_{\alpha\beta}] \\
& + [(\mathbf{P}^{S-1} \cdot \mathbf{S}^\beta) : \mathbf{I}] [(\mathbf{E}^\alpha \cdot \mathbf{P}^E) : \hat{\mathbf{r}}_{\alpha\beta} \hat{\mathbf{r}}_{\alpha\beta}] \} \\
& + \{ [(\mathbf{P}^{S-1} \cdot \mathbf{S}^\alpha) : \hat{\mathbf{r}}_{\alpha\beta} \hat{\mathbf{r}}_{\alpha\beta}] [(\mathbf{E}^\alpha \cdot \mathbf{P}^E) : \mathbf{I}] \\
& + [(\mathbf{P}^{S-1} \cdot \mathbf{S}^\beta) : \hat{\mathbf{r}}_{\alpha\beta} \hat{\mathbf{r}}_{\alpha\beta}] [(\mathbf{E}^\beta \cdot \mathbf{P}^E) : \mathbf{I}] \\
& + [(\mathbf{P}^{S-1} \cdot \mathbf{S}^\alpha) : \hat{\mathbf{r}}_{\alpha\beta} \hat{\mathbf{r}}_{\alpha\beta}] [(\mathbf{E}^\beta \cdot \mathbf{P}^E) : \mathbf{I}] \\
& \left. + [(\mathbf{P}^{S-1} \cdot \mathbf{S}^\beta) : \hat{\mathbf{r}}_{\alpha\beta} \hat{\mathbf{r}}_{\alpha\beta}] [(\mathbf{E}^\alpha \cdot \mathbf{P}^E) : \mathbf{I}] \right\}. \tag{3.32}
\end{aligned}$$

CHAPTER 4

MICROVISCOSITY, NORMAL STRESS AND OSMOTIC PRESSURE OF BROWNIAN SUSPENSIONS BY ACCELERATED STOKESIAN DYNAMICS SIMULATION

4.1 Introduction

Many-body hydrodynamic interactions present in concentrated suspensions, in addition to roughness and Brownian motion, can produce qualitatively different rheology than in dilute suspensions. Thus far we have presented how many-body colloidal interactions can be captured via tabulated mobility functions, which may be suitable for insertion into theoretical models for suspension behavior. In this chapter, we apply these concentrated mobility functions into the case of active microrheology by bridging the dilute theory of microrheology [40, 41] to the concentrated suspensions. In particular, the scaling theory with the mobility functions indicates the role of many-body hydrodynamic interactions in producing non-Newtonian rheology.

Asymmetric distortion and relaxation of the microstructure produces well-known non-Newtonian rheology, such as shear-thinning and thickening [10, 143], viscoelasticity [115], normal stress differences [62], and flow-induced diffusion [60], among others. Many of these effects are explained at the pair level, while three-body interactions can further impose qualitative, concentration-dependent changes in non-Newtonian rheology. Theoretical models of suspension behavior have successfully predicted non-Newtonian flow behavior in suspensions undergoing shear, extensional flow, and falling-ball rheometry, i.e., macroscale flows. Microrheology is an important complement to these macro-

scopic techniques, especially for interrogation of microscopically small systems, and has successfully recovered many rheological behaviors traditionally measured via macroscale techniques, including viscosity, diffusivity and normal stress differences. Detailed theoretical connections of microstructure to rheology are well-established in both macroscope and microscope approaches.

Non-Newtonian rheology in hard-sphere suspensions arises when microstructural symmetry is broken and this asymmetry is sustained over time or length scales long compared to the particle relaxation time scale. In a dilute dispersion, where only pair interactions matter, non-Newtonian rheology corresponds to a loss of Stokes-flow reversibility in relative pair trajectories, where Brownian motion or particle roughness, for example, drive particles off Stokes-flow trajectories. For instance, while a suspension of smooth spheres undergoing simple shear or polydisperse sedimentation in the absence of Brownian motion has spherically symmetric structure and Newtonian rheology, even very weak Brownian motion destroys this symmetry, leading to flow-dependent viscosity. In the same flows of non-colloids, particle roughness also destroys Stokes-flow reversibility. Indeed, surface asperities as small as one ten-thousandth of a particle size produce similar effects [49]. The excluded-annulus model [131], which served as a simplistic, yet useful, representation simulating various surface conditions, has been employed to incorporate the effect of particle roughness into the dilute theory and recover non-Newtonian behaviors. However, missing in all these dilute models is the detailed effect of three-body interactions.

Many-body interactions give rise to qualitative changes in suspension rheology that cannot be captured by the dilute theory where only pair-level particle

interactions are considered. The leading-order effect is the loss of Stokes-flow fore-aft symmetry, time reversibility, and thus Newtonian rheology. The presence of three-body or higher-order interactions breaks fore-aft symmetry, but in principle, particle trajectories are still time reversible. As a result, if the initial configuration is random, the structure of the suspension is still symmetric on average, even though for one realization a third particle breaks the fore-aft symmetry. To trigger non-Newtonian rheology, time reversibility must be destroyed, which is nearly unavoidable in experiments or simulations, owing to the chaotic sensitivity of three-body trajectories to infinitesimally small perturbations, such as residual Brownian motion or particle roughness. That is, in the presence of many-body hydrodynamic interactions, small perturbations quickly amplify and propagate to give time-irreversible suspension mechanics. This idea was first discussed by Leighton and Acrivos [97] in their seminal study of shear-induced migration of non-colloids, an effect the authors attributed to irreversible diffusion arising from a combination of many-body hydrodynamic interactions and particle roughness. More recent work has captured this behavior, beginning most notably with the study of Jánosi et al. [82], who numerically modeled the sedimentation of three particles in Stokes flow, showing that particle motions are extremely sensitive to their initial configurations. They found that the particle trajectories separate exponentially in time with a positive Lyapunov exponent, thus quantifying the chaotic nature of hydrodynamic interactions. Marchioro and Acrivos [111] and Drazer et al. [53] connected this phenomenon to many-body interactions between sheared non-colloids and resultant non-Brownian diffusion. They further showed that, in simple shear flow of non-colloids, even if all external and microscopic forces are deterministic, particle trajectories are stochastic and chaotic. When particle roughness is signifi-

cant, pair encounters break fore-aft symmetry, and thus produce an $O(\phi)$ transverse diffusivity, where ϕ is the particle volume fraction of the suspension. For nearly smooth particles, three-body hydrodynamic interactions are responsible for the loss of fore-aft symmetry, giving rise to irreversible diffusion that scales as $O(\phi^2)$. Pine et al. [126] found a threshold shear rate that separates reversible particle trajectories from chaotic behaviors, by measuring the diffusivity of non-colloidal particles in an oscillatory shear flow with both experiments and simulations. Overall, these studies show that small perturbations and three-body interactions are essential to introducing time irreversibility, but how three-body hydrodynamic interactions quantitatively give rise to non-Newtonian rheology is still not clear.

One way to view the shear-rate and concentration dependence of loss of Stokes-flow symmetry, and its connection to the influence of many-body hydrodynamic interactions on non-Newtonian rheology, is to recognize that from a trajectory perspective, the loss of memory occurs as a pair encounter progresses. In the present work, we utilize Accelerated Stokesian Dynamics (ASD) simulations to study the effect of many-body hydrodynamic interactions on particle trajectories, microstructure, and non-Newtonian rheology. To focus on the connection between particle trajectories and non-Newtonian rheology, we study flow-dependent rheology via active microrheology, in both dilute and concentrated suspensions with varying volume fraction and strength of probe forcing. The active microrheology framework has been described in a review article by Zia [147].

The ASD algorithm rigorously accounts for many-body far-field hydrodynamic interactions and near-field lubrication interactions, thus allowing the

study of suspensions ranging from dilute to maximum packing. Here, we study the evolution of structure and rheology as it evolves with strength of probe forcing. The microviscosity, normal stresses, normal stress differences and osmotic pressure are measured over a range of volume fractions, $0.05 \leq \phi \leq 0.4$. We find that, as concentration increases, the osmotic pressure and normal stresses increase, indicating greater storage of flow energy relative to that dissipated by viscous drag. Structural distortion is more pronounced as volume fraction increases, supporting this view. An increase of osmotic pressure with increasing volume fraction is unsurprising at equilibrium, given the connection of osmotic pressure to the chemical potential. The viscosity also increases as concentration grows. An increase in dissipation (viscosity) with increasing volume fraction also makes sense physically, if one draws on a similar dependence at equilibrium where no-slip surfaces increase stress and viscosity. However, under flow, at the pair level, hydrodynamic coupling lengthens the duration of pair encounters, suppressing the formation of structural asymmetry and thus non-Newtonian rheology. One might then expect an increase in concentration to exaggerate this response. While we do find that increasing volume fraction drives up the non-equilibrium viscosity, we find just the opposite for the normal stress difference and osmotic pressure: increasing volume fraction leads to increased structural asymmetry and enhanced energy storage. This behavior must owe its origins to three-body and higher-order hydrodynamic interactions. We hypothesize that the loss of time- and fore-aft symmetry of relative trajectories caused by three-body hydrodynamic interactions leads to this behavior. To interrogate this idea, we developed scaling theories to bridge the dilute theory for the rheological quantities in suspensions to arbitrary concentration, where the concentrated mobility functions derived recently by Zia et al. [150] are introduced to

collapse the concentrated results onto dilute theory. Agreement between our scaling theory and simulation results in suspension stress suggests that three-body hydrodynamic interactions are most pronounced when probe forcing is strong. Further study shows that the transverse mobility of the particle pair in the presence of the third particle is responsible for the non-Newtonian rheology, since physically it gives rise to loss of fore-aft symmetry. In weak probe forcing, the irreversibility from three-body encounters is not important because advection is weak.

The remainder of this chapter is organized as follows: in section 4.2, the microrheology model system is presented, where the excluded annulus model is utilized to tune the strength of hydrodynamic interactions. The method to evaluate microviscosity and suspension stress from the particle motion is addressed in section 4.3, followed by presentation of the simulation techniques in section 4.4 for the evolution of particle configurations from N -body Langevin equations. Results are presented in section 4.5, beginning with the evolution of the non-equilibrium microstructure under weak to strong probe forcing and dilute to dense particle concentration. Focus is placed on the microviscosity, normal stresses parallel and perpendicular to the direction of the external force, the normal stress difference and the osmotic pressure. The quantities are measured for the full range of forcing, spanning five decades of probe forcing and for volume fraction $0.05 \leq \phi \leq 0.4$, revealing an important transition from the dilute, two-body interaction-dominated regimes to concentrated regimes, where three-body hydrodynamic interactions also matter. To gain insight into the role of many-body hydrodynamic interactions in Non-Newtonian behaviors, we developed a scaling theory to bridge the concentrated rheology to the dilute theory. The study is concluded in section 4.6 with a summary.

4.2 Microrheology model system

We consider a suspension of neutrally buoyant, colloidal hard spheres all of hydrodynamic radius a , immersed in an incompressible Newtonian fluid of density ρ and dynamic viscosity η . In active microrheology, a probe particle is dragged by an external force, \mathbf{F}^{ext} , through a bath of particles. The characteristic velocity \mathbf{U} of probe motion sets the Reynolds number, $Re \equiv \rho U a / \eta$. Because the probe and bath particles are small, $Re \ll 1$, inertial forces can be neglected and thus the fluid mechanics are governed by the Stokes equations. The probe number density, n_a , relative to the number density of bath particles, n_b , is small. Probe motion distorts the equilibrium microstructure while the Brownian motion of the bath particles acts to recover their equilibrium configuration. This gives rise to an entropic restoring force, kT/a , where k is Boltzmann's constant and T is the absolute temperature. The degree of distortion of the microstructure, and hence its influence on probe motion, is set by the strength of probe forcing, F^{ext} , relative to the entropic restoring force, defining a Péclet number: $Pe = F^{ext}/(kT/a)$. The volume fraction of bath particles is defined as $\phi_b \equiv (4\pi a^3/3)N_b/V$, where N_b is the number of bath particles, and V is the system volume.

4.3 Measurement of rheological quantities

Dynamic simulations provide the same particle displacements and interactions as would be measured in experiments. Here we relate probe behavior and bath particle configurations to the rheological quantities we seek. We begin with the microviscosity, which is related to average probe speed via Stokes' drag law.

This is followed by the suspension stress, and its connection to particle configuration.

4.3.1 Microviscosity

In microrheology, since the probe is dragged through a suspension, the neighboring particles are entrained by the motion of the probe. The perturbed bath particles changes the equilibrium configuration, formed a microstructure. This microstructure in turn hinders the probe, slowing its motion. Squires and Brady [135] and Khair and Brady [87] interpreted the mean-speed reduction as a viscous drag of the bath and defined an effective viscosity η^{eff} via the application of Stokes' drag law:

$$\frac{\eta^{eff}}{\eta} \equiv \frac{F^{ext}}{6\pi\eta a\langle U \rangle}, \quad (4.1)$$

where $\langle U \rangle = -\langle \mathbf{U} \rangle \cdot \mathbf{F}^{ext}/F^{ext}$, and $\langle \mathbf{U} \rangle$ is the velocity of the probe, averaged over many encounters with background particles.

The effective viscosity can be written as that due to the solvent drag on the probe, plus the drag due to microscopic forces between the probe and the bath particles:

$$\frac{\eta^{eff}}{\eta} = 1 + \frac{\eta^{micro}}{\eta}. \quad (4.2)$$

The microviscosity, η^{micro} , measures the viscosity arising from both the equilibrium hindrance due to the presence of the particles, and that due to the non-equilibrium distortion of the particle structure. Combing equations (4.1) and (4.2) gives the expression of microviscosity,

$$\frac{\eta^{micro}}{\eta} = \frac{F^{ext}}{6\pi\eta a\langle U \rangle} - 1, \quad (4.3)$$

In experiments and simulation, the microviscosity is measured in a straightforward way as the mean probe velocity over a range of time, whereas in theory it is calculated as an integration over the whole space via probe-bath mobility couplings [135, 87].

4.3.2 Suspension stress

In rheology, the bulk stress $\langle \Sigma \rangle$ can be divided into fluid-phase stress and particle-phase stress [12, 14]:

$$\langle \Sigma \rangle = -\langle p \rangle \mathbf{I} + 2\eta \langle \mathbf{E} \rangle + \langle \Sigma^P \rangle, \quad (4.4)$$

where $\langle p \rangle$ is the pressure of the incompressible fluid, \mathbf{I} is the identity tensor, $2\eta \langle \mathbf{E} \rangle$ is the deviatoric stress contribution from the fluid, and $\langle \Sigma^P \rangle$ is the particle-phase stress. The stresses are ensemble averaged over the whole volume V containing N bath particles, denoted as $\langle \cdot \rangle$. In active microrheology, the particle-phase stress, $\langle \Sigma^P \rangle$, is studied by Chu and Zia [39] for dilute suspensions, where they divided the particle-phase stress into non-hydrodynamic and hydrodynamic contributions, respectively,

$$\langle \Sigma^P \rangle = -n_a k T \mathbf{I} - n_a \langle \mathbf{r} \mathbf{F}^P \rangle + n_a (\langle \mathbf{S} \rangle^{H,ext} + \langle \mathbf{S} \rangle^B + \langle \mathbf{S} \rangle^{P,dis}). \quad (4.5)$$

The first term, $-n_a k T \mathbf{I}$, is the equilibrium particle stress from thermal fluctuations of Brownian particles. The second term, $-n_a \langle \mathbf{r} \mathbf{F}^P \rangle$, is the non-hydrodynamic interparticle stress and originates from interparticle elastic collisions. The remaining term represents the particle-phase stress arising from hydrodynamic interactions. The stresslets, \mathbf{S} , correspond to the symmetric part of the first moment of the stress tensor. Physically, microscopic forces induce relative motion between particles. The relative motion further gives rise to stresslet

on the particle surfaces since particles are hydrodynamically coupled. Specifically, the stresslets induced by external probe forcing, Brownian motion, and interparticle forces are represented by stresslets $\mathbf{S}^{H,ext}$, \mathbf{S}^B , and $\mathbf{S}^{P,dis}$, as shown in Equation 4.5. These stresslets are formulated as:

$$\langle \mathbf{S}^{H,ext} \rangle = -\langle \mathbf{R}_{SU} \cdot (\mathbf{R}_{FU}^{-1} \cdot \mathbf{F}^{ext}) \rangle, \quad (4.6)$$

$$\langle \mathbf{S}^B \rangle = -kT \langle \nabla \cdot (\mathbf{R}_{SU} \cdot \mathbf{R}_{FU}^{-1}) \rangle, \quad (4.7)$$

$$\langle \mathbf{S}^{P,dis} \rangle = -\langle \mathbf{R}_{SU} \cdot \mathbf{R}_{FU}^{-1} \cdot \mathbf{F}^p \rangle. \quad (4.8)$$

In these equations, \mathbf{F}^p denotes the interparticle force, \mathbf{R} represents the hydrodynamic resistance tensors which couple surface traction of particles to their motion. Specifically, \mathbf{R}_{FU} denotes the resistance tensors coupling force and torque to translation and rotation; \mathbf{R}_{SU} denotes the coupling between stresslet on the surface of particles and particle translation or rotation. Physically, the advective flow arising from the externally applied force gives rise to an external-force induced stresslet $\mathbf{S}^{H,ext}$ on a particle surface because it cannot deform. The Brownian stresslet \mathbf{S}^B on particle surfaces arises due to disturbance flows driven by the Brownian motion of bath particles as it acts to smooth microstructural gradients [17]. Finally, relative motion produced by interparticle forces gives rise to disturbance flows that in turn create a stresslet $\mathbf{S}^{P,dis}$ on particle surfaces.

The stress tenor, Σ^p , has six independent elements in general. In microrheology, however, only the normal stresses are non-zero, owing to the axisymmetric geometry of the structure around the probe. We denote the three normal stresses as Σ_{xx} , Σ_{yy} and Σ_{zz} , where x is the direction parallel to the external force. The axisymmetric structure also implies that the stresses perpendicular to the direction of the external force are equal, i.e., $\Sigma_{yy} = \Sigma_{zz}$. Thus in active microrheology, the

suspension stresses are expressed by only two components: the parallel normal stress, Σ_{\parallel} , and the perpendicular normal stress, Σ_{\perp} , where $\Sigma_{\parallel} \equiv \Sigma_{xx}$, $\Sigma_{\perp} \equiv \Sigma_{yy}$.

The normal stress differences characterize the anisotropic deformation of a suspension arising from the distortion of the microstructure, and are formulated as:

$$\begin{aligned} N_1 &= \Sigma_{xx} - \Sigma_{yy}, \\ N_2 &= \Sigma_{yy} - \Sigma_{zz}, \end{aligned} \tag{4.9}$$

where N_1 represents the first normal stress difference, N_2 represents the second normal stress difference. Because the two perpendicular components are identical due to the axisymmetric microstructure, N_2 is always zero. Thus only the first normal stress difference is measured.

The tendency for isotropic expansion or contraction of the particle phase is described by the osmotic pressure, which is defined as negative one third of the trace of the stress tensor,

$$\langle \Pi \rangle = -\frac{1}{3} \mathbf{I} : \langle \boldsymbol{\Sigma}^P \rangle. \tag{4.10}$$

To evaluate the microviscosity, and suspension stress in simulations via Equations (4.3), (5.20), (4.7), (4.8), and (4.10), hydrodynamic couplings and forces must be provided. The external force is prescribed. The interparticle force \mathbf{F}^P is evaluated as the gradient of the interparticle potential between particles, $\mathbf{F}^P = -\nabla \mathcal{V}$, given an arbitrary particle potential, \mathcal{V} . The resistance tensors, \mathbf{R} , are functions of only particle configurations and can be evaluated given the positions of all the particles in the suspension. Thus in simulations, to measure the microviscosity and suspension stress, we must solve for the particle motion and evolve the suspension configurations in each time step. The method of our approach is given next.

4.4 Simulation Method

In Stokesian dynamics simulations, the particle motion is governed by the coupled N -body Langevin equation, a force/torque balance between hydrodynamic, Brownian, interparticle and external forces/torques,

$$\mathbf{0} = \mathbf{F}^H + \mathbf{F}^B + \mathbf{F}^P + \mathbf{F}^{ext}, \quad (4.11)$$

where the left-hand side is zero because inertia is neglected. In Equation 4.11, \mathbf{F} represents force/torque vectors of dimension $6N$. The prescribed external force, \mathbf{F}^{ext} , only acts on the probe and is zero for all bath particles. The method to compute the hydrodynamic, Brownian and interparticle forces are presented below.

In the absence of imposed far-field flow, the hydrodynamic forces on the particles, \mathbf{F}^H , are written as:

$$\mathbf{F}^H = -\mathbf{R}_{FU} \cdot \mathbf{U}. \quad (4.12)$$

Here \mathbf{U} is a vector of $6N$, representing the particle translational/rotational velocity.

The Brownian force \mathbf{F}^B arises from the thermal fluctuations in the fluid and is a Gaussian stochastic variable,

$$\overline{\mathbf{F}^B} = 0, \overline{\mathbf{F}^B(0)\mathbf{F}^B(t)} = 2kT\mathbf{R}_{FU}\delta(t), \quad (4.13)$$

where the overbar denotes an ensemble average over the thermal fluctuations in the fluid, and $\delta(t)$ is the Dirac function.

The interparticle force, \mathbf{F}^P , describes any particle-particle interactions. In our simulations, hard spheres are modeled and the interparticle force is given by

$\mathbf{F}^P = \frac{1}{2}kT\hat{\mathbf{r}}\delta(r-2a)$, where r is the separation distance between particle pairs and $\hat{\mathbf{r}}$ is a unit vector pointing from particle center to center. Since in simulations particles interacting with full hydrodynamic interactions are modeled, where lubrication forces prohibit particles touching each other, the interparticle force is negligible.

By plugging the expressions of forces (Equation 4.12, 4.13) into Equation 4.11 and integrating it over a time step Δt , the displacement equation of particles is obtained:

$$\Delta\mathbf{x} = \mathbf{R}_{FU}^{-1} \cdot \hat{\mathbf{F}}^{ext}\Delta t + kT\nabla \cdot \mathbf{R}_{FU}^{-1}\Delta t + \mathbf{X}(\Delta t) + o(\Delta t), \quad (4.14)$$

with

$$\overline{\mathbf{X}} = 0, \overline{\mathbf{X}(t)\mathbf{X}(t)} = 2kT\mathbf{R}_{FU}^{-1}\Delta t. \quad (4.15)$$

The first term on the right hand side of Equation 4.14 represents the displacement of particles arising from external forcing. The second term describes the Brownian drift, which is the net displacement of a collection of particles due to Brownian motion. The Brownian displacement, \mathbf{X} , representing the diffusive motion of particles, is a random vector with zero mean and its covariance is linear in the inverse of the resistance tensor, as shown by Equation (4.15).

To facilitate our analysis, we nondimensionalize the quantities as follows. Particle position \mathbf{x} is non-dimensionalized by the characteristic particle size a . The time is scaled by the diffusive time scale a^2/D_b for weak forcing and by the advective time scale a/U for strong forcing, where D_b is the diffusivity of a single bath particle in the solvent, U is a characteristic probe velocity. When forcing is weak, the time scaling is set by the diffusive motion, which produces the dimensionless displacement equation:

$$\Delta\mathbf{x} = Pe(\mathbf{R}_{FU}^{-1} \cdot \hat{\mathbf{F}}^{ext})\Delta t + \Delta\mathbf{x}^P + \nabla \cdot \mathbf{R}_{FU}^{-1}\Delta t + \mathbf{X}(\Delta t) + o(\Delta t), \quad (4.16)$$

where the Péclect number, $Pe = F^{ext}/kT$, emerges naturally in the evolution equation after the non-dimensionalization. For strong forcing where advection dominates, the equation reads

$$\Delta \mathbf{x} = (\mathbf{R}_{FU}^{-1} \cdot \hat{\mathbf{F}}^{ext}) \Delta t + \frac{1}{Pe} \nabla \cdot \mathbf{R}_{FU}^{-1} \Delta t + \frac{1}{Pe^{1/2}} \mathbf{X}(\Delta t) + o(\Delta t). \quad (4.17)$$

Particle dynamics are obtained from Equations 4.16 and 4.17 once we construct the resistance tensor, \mathbf{R}_{FU} . As mentioned above, it couples hydrodynamic force and torque to particle motion and is only a function of particle configurations. In simulations, we also compute particle stresslets. To this end, a more general resistance matrix involving couplings between stresslet and particle motion, \mathcal{R} , is defined as

$$\mathcal{R} = \begin{pmatrix} \mathbf{R}_{FU} & \mathbf{R}_{FE} \\ \mathbf{R}_{SU} & \mathbf{R}_{SE} \end{pmatrix}. \quad (4.18)$$

Here the subscript S denotes the stresslet on the surface of the particles, E denotes the rate of strain of particles and fluid. Since hard spheres cannot deform, E can only arise from the imposed flow. The superscripts FE , SU and SE indicate the resistance tensors coupling force and torque to flow rate of strain, stresslet to particle motion, and stresslet to flow rate of strain, respectively.

An extension of Equation (4.11) is obtained according to the grand resistance tensor, \mathcal{R} , viz.,

$$\begin{pmatrix} \mathbf{0} \\ \mathbf{S} \end{pmatrix} = -\mathcal{R} \cdot \begin{pmatrix} \mathbf{U} \\ \mathbf{0} \end{pmatrix} + \begin{pmatrix} \mathbf{F}^B + \mathbf{F}^P + \mathbf{F}^{ext} \\ -\mathbf{rF}^P \end{pmatrix}. \quad (4.19)$$

The resistance tensor, \mathcal{R} , captures the many-body hydrodynamic interactions between all the particles in a suspension. For a pair of particles closely spaced, two-body interactions are pronounced and are well-established analytically in the literature [84, 83]. For particles far from each other, many-body interactions

must be considered because the effect of intervening particles between the pair is significant. Thus \mathcal{R} is evaluated as a sum of the near-field two-body hydrodynamic interactions, and the far-field many-body hydrodynamic interactions,

$$\mathcal{R} = \mathcal{R}_{nf} + \mathcal{M}^{\infty-1}. \quad (4.20)$$

The two-body near-field resistance matrix, \mathcal{R}_{nf} , is directly computed by linear superposition of the analytical, pairwise resistance functions from Jeffrey and Onishi [84], Jeffrey [83] and Jeffrey et al. [85]. The far-field grand mobility matrix, \mathcal{M}^∞ , is constructed from a Taylor expansion of the Green's function of Stokes equation, and truncating the expansion to the first traction moment [28], which estimates the first reflection of long-range hydrodynamic interactions. Furthermore, the inverse of the far-field mobility, $\mathcal{M}^{\infty-1}$, captures the many-body interactions [55]. To accelerate the computation, Particle-Mesh-Ewald (PME) method is utilized to avoid constructing \mathcal{M}^∞ explicitly and an iterative method is utilized to evaluate matrix inverse [133].

To compute the osmotic pressure in simulations, the trace of the resistance \mathbf{R}_{SU} , defined as $\mathbf{P} = \mathbf{I} : \mathbf{R}_{SU}$, must be evaluated, where \mathbf{P} represents the coupling between the pressure moment on the surface of particles and particle motion. Similarly like the construction of resistance matrix \mathcal{R} , \mathbf{P} is computed from the analytical expression of two-body hydrodynamic interactions [85], and the far-field many-body estimation [75].

In our study, each simulation has 25 advective time with time step 0.001 advective time unit. The number of particles is ranging from 187 to 382. We implemented simulations for volume fraction ϕ_b ranging from 0.05 to 0.4, with flow strength ranging from 0.1 to 30000, each case with 100 – 200 simulations. The measured quantities in the simulations are averaged over all the time steps

and all simulations. The periodic boundary condition utilized in the present simulations generates infinite image probes moving in neighboring simulation boxes. Due to the small size of the box, probe motion can be slow down by its images. Thus a correction is implemented to the probe motion, and thus the microviscosity [133].

4.5 Results

Here we examine the influence of volume fraction on the evolution of microstructure with flow strength and on the non-Newtonian rheology of the suspension.

4.5.1 Microstructure

As the probe moves through the bath, its interaction with the bath particles distorts their arrangement. Over long times, the probe encounters many different particle configurations. At steady state, an average of these structures over time approaches an ensemble average over all permissible arrangements, giving the average steady-state microstructure. The positions of all particles were monitored throughout simulation, giving the distribution of bath particles relative to the probe in a frame of reference moving with the probe. The steady-state temporal average was computed and is plotted in Figure 4.1 for several values of forcing strength, Pe , and volume fraction, ϕ . Each column in the figure corresponds to one value of Pe , increasing from left to right. Across each row, volume fraction is held fixed, increasing from top to bottom. The black circle at the cen-

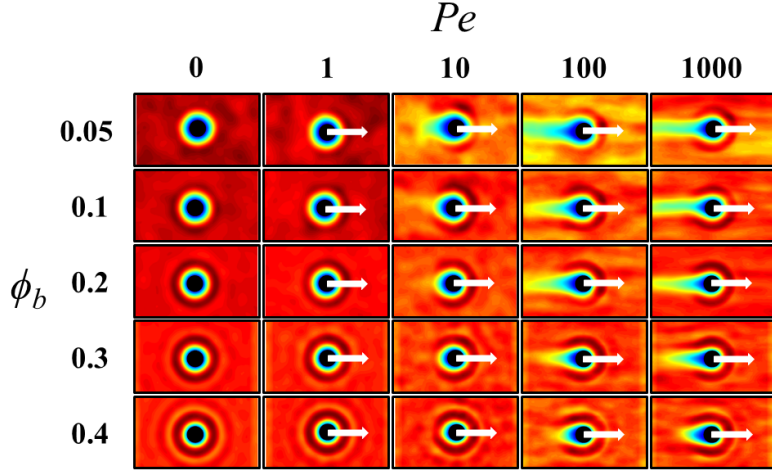


Figure 4.1: Evolution of the microstructure from a side-view of the simulation cell transverse to probe forcing. The black region represents the probe and it is surrounded by a region excluded to particle centers. Probe forcing Pe increases from left to right, and volume fraction ϕ increases from top to bottom, as labeled. Regions in dark red indicate particle-center accumulation; blue regions indicate particle-center depletion.

ter represents the probe and, at equilibrium (far left column) it is surrounded by a blue ring showing the exclusion of bath-particle centers closer than $r = 2a$. A bath-particle accumulation ring (dark red) shows the nearest-neighbor ring that emerges distinctly as volume fraction becomes high enough to produce liquid-like structure.

In the second column, $Pe = 1$ and, in this regime, advection is as important as Brownian motion. Thus, probe motion is able to distort the structure, and Brownian motion cannot fully erase the disturbance, at least for $\phi \leq 0.3$. However, at $\phi = 0.4$ the isotropic structure is still intact. This persistence of structural distortion arises from the volume-fraction dependence of the gradient of particle density that in turn produces local Brownian drift, a deterministic force driving the probe toward more mobile regions, $\langle \nabla \cdot \mathbf{M} \rangle_{nn}$, where $\mathbf{M} = \mathbf{R}^{-1}$ is the configuration-dependent hydrodynamic mobility and $\langle \cdot \rangle_{nn}$ indicates an average over many probe-bath particle relative configurations around the nearest-

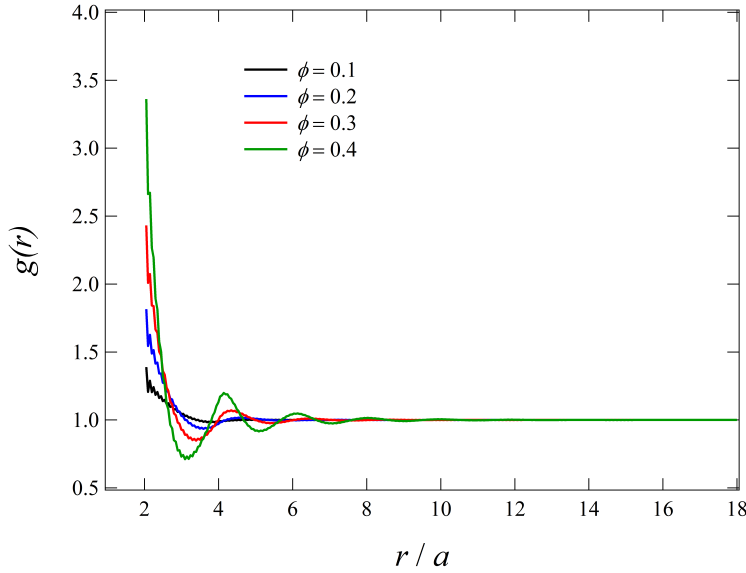


Figure 4.2: Equilibrium pair distribution function $g(r)$ computed from Percus-Yevick equation ([122]) for different volume fractions.

neighbor ring of particles surrounding the probe. In the concentrated regime, a liquid-like structure forms and produces fluctuations in particle density that become more pronounced as volume fraction grows. This is illustrated in Figure 4.2, which is a plot of the pair distribution function $g(r)$ for several volume fractions estimated by the Percus-Yevick equation [122]. These density peaks and troughs produce corresponding mobility troughs and peaks, respectively, and influence relative particle motion [150]. As volume fraction grows, the nearest neighbor peak grows taller, narrows, and moves to the left: the region becomes crowded. Consequently, at high concentration, the relative motion between the probe and bath particles in the region of the nearest-neighbor ring is slowed by the increase in nearby no-slip surfaces (lower relative mobility). Since relative particle velocity decreases but more bath particles flow into the nearest-neighbor region as volume fraction grows, the relative advective flux is relatively unchanged as volume fraction grows at $Pe = 1$. At $Pe = 1$, the

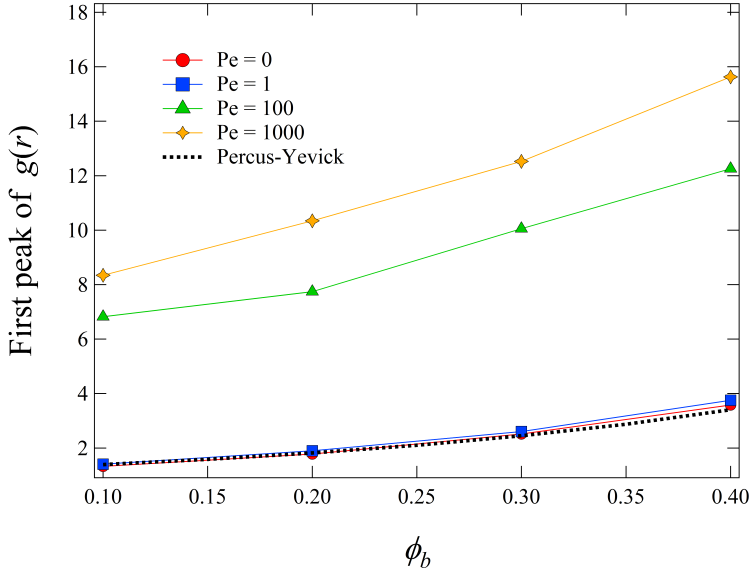


Figure 4.3: The first (largest) peak of pair distribution function $g(r)$, calculated by accounting all upstream bath particles and ignore the angular distribution. The peak value of $g(r)$ is shown as a function of volume fraction ϕ and probe forcing Pe .

advection flux is balanced by the relative diffusive flux, which is driven by radial gradients in the structure, $\partial g / \partial r$, projected through the suspension at a strength given by the radial relative mobility [87, 77]. Close to the probe the relative mobility decreases as volume fraction grows and the nearest neighbor region becomes crowded; the density gradient must thence increase to enforce no relative flux at contact. Consequently, in the $Pe \sim 1$ regime, where Brownian drift is as strong as advection, increases in concentration effectively reduce the Peclet number: concentration-gradient dependent Brownian drift outpaces advection and restores structural isotropy. Overall, when advection is not strong, increased particle concentration preserves the symmetry of microstructure.

As probe forcing grows, however, hindrance from Brownian motion is overcome by advection and the nearest-neighbor ring is broken open in the downstream region, as seen in the columns for $Pe \geq 10$, all rows. Here, the familiar

boundary-layer and trailing wake structure emerge - and the qualitative effect exerted by particle concentration becomes more pronounced. At a fixed value of Pe , particle density in the upstream boundary layer increases as volume fraction increases. To determine whether three-body interactions contribute to this growth, we seek to determine whether $g(r, \phi, Pe)$ shows more significant non-linear relation vs. ϕ , comparing with the equilibrium relation. In particular we are interested in how the nearest-neighbor peak in Figure 4.2 would change with flow strength, because stronger flow strength is expected to produce more three-body interactions, and is most pronounced near contact. We interrogate the simulation data that underlie the contour plots in Figure 4.1, focusing on the upstream region in front of the probe. The region is divided into hemispherical annular bins of thickness Δr . The pair distribution function $g(r)$ is calculated with appropriate normalization for bin volume. The peak of $g(r)$ is identified from the largest value, and plotted as a function of ϕ for several Pe in Figure 4.3. The dashed line indicates the value of first peak of $g(r)$ as a function of volume fraction from the Percus-Yevick equation, and filled symbols are peak values from simulations for a range of volume fraction and Peclet number. For all Pe , increasing volume fraction gives rise to a growth of particle density at the first peak. However, for equilibrium ($Pe = 0$) and near-equilibrium suspensions ($Pe = 1$), the trends are almost the same as that from Percus-Yevick equation. Even at equilibrium, the contributions of three-body interactions to density fluctuation begin to dominate osmotic pressure and particle dynamics at $\phi \geq 35\%$. In a vivid expansion of the density, the coefficient of the three-body interaction term grows with flow strength, Pe , because particles driven closer together couple for longer duration via hydrodynamic interactions. As Pe increases, the increase of pair distribution function at a fixed volume fraction

shows more pronounced accumulation of bath particles upstream of the probe. Instead of a near-linear relation between particle density and volume fraction as shown by the near-equilibrium curves, larger Pe leads to a more pronounced nonlinear increase of particle density inside the nearest-neighbor ring. Since we consider fully hydrodynamic interactions, and two-body interactions only give rise to a linear relation as $g \sim \phi$, this more pronounced nonlinear trend can only arise from three-body and higher-order interactions. For higher concentration ($\phi \geq 0.3$), the slopes of the curves increase as Pe grows, indicating that strong flow creates a region of more likely three-body interactions, and thus give rise to more pronounced nonlinear increase of accumulation of bath particles. For lower concentration ($\phi \leq 0.2$), the slope almost remains the same for flow strength from $Pe = 1$ to 100, but increases as $Pe \rightarrow 1000$. This is because three-body interactions are relatively rare in low concentration, and thus a stronger flow is necessary to introduce more three-body interactions and give rise to the increased nonlinear behavior. Besides the thicker boundary layer upstream, as volume fraction increases, the boundary layer remains attached to the probe farther downstream, wrapping more closely around the trailing side of the probe. Meanwhile, the trailing wake shortens at fixed Pe as volume fraction increases. Since higher concentration also gives rise to higher particle density outside the boundary layer, and the particle density inside the trailing wake is very low for all volume fractions, a sharper density gradient across the wake is produced for higher volume fraction. This leads to a more pronounced Brownian drift force that closes the wake more rapidly. One can anticipate rheological consequences of the thicker boundary layer and shorter trailing wake arising from the high volume fraction. In the next section it will be shown that non-Newtonian rheological behaviors arise from three-body interactions that emerge at higher

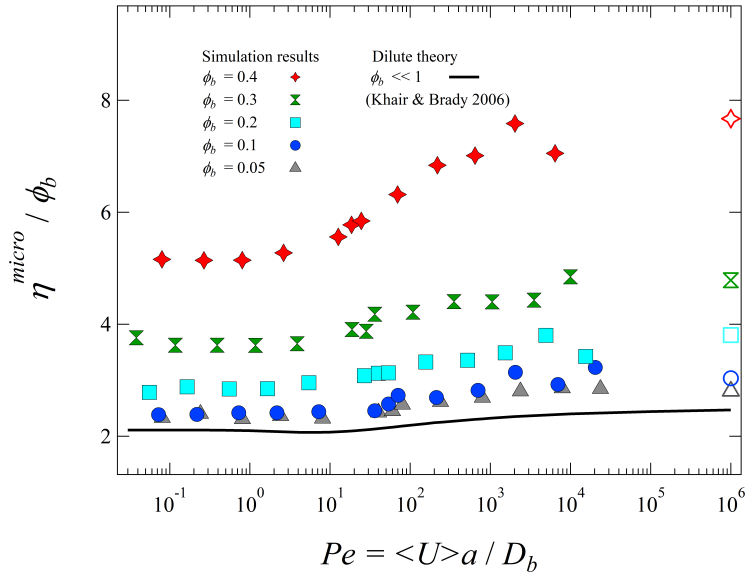


Figure 4.4: Microviscosity as a function of Pe and ϕ_b . Symbols are simulation results from present study; open symbols at far right correspond to $Pe^{-1} = 0$.

concentrations.

4.5.2 Rheology

In the previous section, contour plots of the deformed microstructure around the forced probe showed that increasing particle concentration exerts a qualitative effect on the evolving structure that is expected to alter probe motion and hence the rheology inferred by tracking its motion. In the present section, we examine how microviscosity and stress mirror these structural effects with concentration-dependent non-Newtonian rheology.

4.5.2.1 Microviscosity

The intrinsic ($Pe \rightarrow 0$) viscosity of colloidal suspensions increases as $O(\phi^2)$ when concentration is low, but at $\phi \geq 0.35$, many-body hydrodynamic interactions produce $O(\phi^3)$ contributions that set the speed of divergence as ϕ approaches maximum packing [62]. Here we investigate how concentration affects non-Newtonian rheology of a flowing suspension. In microrheology, the microviscosity is inferred from reductions in average probe speed through the suspension, via application of Stokes' drag law [135, 87]. Figure 4.4 shows the microviscosity η^{micro} computed in this study, as a function of forcing strength Pe , for several volume fractions, ϕ_b . The solid line represents the theoretical results in dilute suspensions [87] for very strong hydrodynamic interactions and the symbols are our simulation results for arbitrary concentration. The microviscosity is scaled by the volume fraction, ϕ_b . When forcing is weak, observable flow thinning occurs in dilute suspensions [87] as advection grows in strength and Brownian motion is too slow to restore structural equilibrium. As flow strength increases, the viscosity force-thickens at $Pe \sim O(10)$ since particles get closer to experience strong lubrication, and thus longer-duration coupling between particle pairs. As Pe tends to infinity, the viscosity asymptotes to the limiting value, 2.51, which corresponds to the falling-ball limit [19, 1]. In this limit, the boundary layer is vanishingly thin. There is negligible contributions from Brownian and interparticle forces, thus only hydrodynamic viscosity matters.

Filled symbols in Figure 4.4 show the simulation results from weak to strong forcing with volume fraction ranging from 0.05 to 0.4. When $Pe^{-1} = 0$, there is no Brownian motion. The empty symbols represent the microviscosity at infinite Pe , measured by turning off the Brownian motion in simulations. Since

the microviscosity is scaled by ϕ , the difference between the simulation results and dilute theory represents the effect of many-body interactions. The increased difference with the growth of concentration shows that, as expected, higher concentration leads to more significant many-body interactions. A higher concentration signifies a more closely-spaced structure. Since the strength of hydrodynamic interactions is inversely proportional to the separation between particles, interactions in concentrated suspensions are stronger, leading to stronger energy dissipation and thus a higher viscosity. Though concentration varies, the viscosity still shows two plateaus in weak and strong probe forcing. However, the slope of force thickening region grows as volume fraction increases, indicating a qualitative change of microviscosity in the presence of three-body interactions. From the microstructure (Figure 4.1), one can observe the change of microviscosity from the nonlinear evolution of structure in high Pe as volume fraction increases. First, bath particles in front of the probe (inside the boundary layer) hinders probe motion via lubrication interactions, and the particle density increases as the volume fraction increases. Second, the lubrication interactions between probe and bath particles downstream also hinder probe motion and increase viscosity. The shorter trailing wake indicates larger hindrance downstream as volume fraction increases. As shown in Figure 4.3, the increase of particle density inside the boundary layer is more pronounced for high concentration due to the three-body interactions, and produces hindrance beyond $O(\phi)$ scaling. As a result, the high- Pe plateau increases faster as volume fraction increases due to the stronger three-body interactions in high concentration. The enhancement of low- Pe plateau is relatively small since three-body interactions are negligible and Brownian motion dominates the rheology. This difference in growth of viscosity in low- and high- Pe regime for different volume fractions

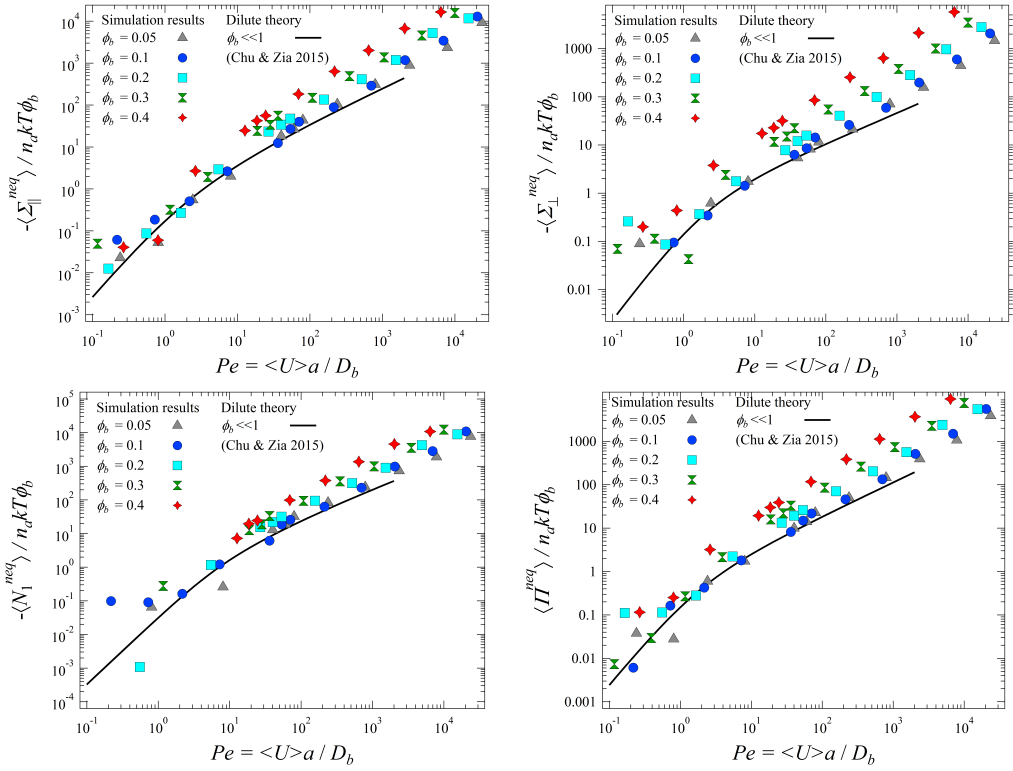


Figure 4.5: Suspension stress as functions of ϕ_b and Pe : (a) parallel normal stress; (b) perpendicular normal stress; (c) first normal stress difference; (d) osmotic pressure. Filled symbols are simulation results, solid lines are dilute theory from Chu & Zia, 2015.

determines the qualitative change of the slopes in the forcing thickening region.

4.5.2.2 Suspension stress

In dilute suspensions, Chu and Zia [39] analytically derived the parallel normal stress, Σ_{\parallel} , perpendicular normal stress, Σ_{\perp} , first normal stress difference, N_1 , and osmotic pressure, Π . Their results for strong hydrodynamics limit are shown by the solid lines in Figure 4.5. The stresses are made dimensionless by $n_a k T \phi_b$, where $n_a k T$ is the ideal osmotic pressure associated with the equilibrium thermal energy of the Brownian particles. Pair-level hydrodynamic interactions are assumed to dominate the higher-order interactions, thus the stresses are

scaled by volume fraction, ϕ_b . In low- Pe , Brownian motion dominates advection. Consequently the disturbance flows that give rise to the Brownian stress are stronger than the weak advective flow due to probe motion. The stresses in this linear-response regime all scales as Pe^2 , which represents a dipolar microstructure disturbance [39]. As Pe grows, the distance that a probe can move in one Brownian time scale grows, and thus give rise to more pair encounters with bath particles and lead to the increase of the suspension stress. For strong probe forcing, Chu and Zia [39] shows that hydrodynamic encounters of probe and bath particles along the line of centers are most pronounced. The scaling is set by the probe-bath lubrication interactions along the line of centers inside the boundary layer, as $Pe^{0.799}$. These non-Newtonian rheology behaviors (non-zero suspensions stress) arise from the asymmetry of the microstructure. For dilute suspensions, this asymmetry arises from small particle roughness and residual Brownian motion.

The filled symbols in Figure 4.5 shows our simulation results of both dilute and concentrated suspensions for volume fraction $0.05 \leq \phi_b \leq 0.4$. In the most dilute suspension, $\phi_b=0.05$, the simulation data and dilute theory of all four stress quantities agree well. However, as concentration increases, the stresses at a given Pe deviate from the dilute theory, and increase monotonically. As mentioned above, the suspension stresses are scaled by $n_a kT$, which represents equilibrium thermal energy of the probe. Thus the suspension stress can be viewed as the energy density of a suspension [148]. Consequently, a distortion of the microstructure gives rise to entropic energy storage, and thus enhance suspension stress. In dilute theory when only pair interactions matter, two-body hydrodynamic interactions preserve fore-aft symmetry and thus suppress structure distortion and give rise to less energy storage and thus a de-

crease of suspension stress. However, as concentration increases, three-body interactions become important. In the presence of a third particle, the pair trajectory loses fore-aft symmetry and thus the microstructure is more distorted. As concentration increases where stronger three-body interactions are involved, the probe motion causes more configuration distortion, i.e., more entropic energy storage on the probe, leading to the enhancement of the suspension stress. This is totally opposite to the effect of pair hydrodynamic interactions in dilute theory, where in dilute limit hydrodynamic interactions are considered to give rise to a decrease of suspension stress and preserve Newtonian rheology. The scaling of stress in high- Pe regime shows a nonlinear evolution, which again corresponds to the nonlinear distortion of the microstructure. In the next section, we will quantitatively analyze the influence of this nonlinear microstructure evolution on suspension stress, and how three-body interactions give rise to non-Newtonian rheology.

4.5.3 Scaling theory

In dilute theory, only pair interactions are considered. However, higher concentration leads to non-negligible many-body hydrodynamic interactions. As shown by the microviscosity and suspension stress in both dilute and concentrated suspensions, even scaled out the pair level effect ϕ_b , difference between dilute theory and simulations is significant, indicating that three-body factor ϕ_b^2 and even higher order factors matter when concentration increases. Thus, a new predictive theory is necessary to describe concentrated suspensions with the consideration of the many-body hydrodynamic interactions. We obtain this by bridging the pair-level dilute theory to our concentrated simulation results

utilizing our new simple scaling theory. Different scaling regimes are applied for microviscosity and suspension stress respectively. For the suspension stress, we implement different scalings for low and high Pe regime. To facilitate introducing the idea, we start with the scalings of the suspension stress.

4.5.3.1 Scaling for suspension stress

Chu and Zia [39] derived the high- Pe asymptote of the suspension stress for a dilute suspension,

$$\frac{\langle \Sigma^{neq} \rangle}{n_a k T \phi_b} \sim Pe^\delta g^{eq}(2) \int_0^\pi A(\theta) f(2; \theta) d\theta. \quad (4.21)$$

Here Σ^{neq} denotes the parallel and perpendicular normal stress, the first normal stress difference and the osmotic pressure because the four quantities have the same high- Pe asymptote formulation. The asymptote comprises a Pe scaling, Pe^δ , the equilibrium microstructure $g^{eq}(2)$, and an integral involving the non-equilibrium microstructure f . The strength of the hydrodynamic interactions inside the boundary layer is evaluated by $A(\theta)$, a function of probe surface angle, θ . Physically, Pe^δ represents the scaling of particle density inside boundary layer. In dilute theory, it is derived by Batchelor [17] as:

$$\delta = \frac{W_0}{G_1} = 0.799, \quad (4.22)$$

where W_0 and G_1 are the leading orders of hydrodynamic mobility functions transverse to and along the line of centers, respectively [[84]]. The pair-distribution function outside the boundary layer, g , is estimated as

$$g(2; \theta) = g^{eq}(2)[1 + f(2; \theta)], \quad (4.23)$$

where $g^{eq}(2)$ represents the equilibrium contribution of the pair-distribution function outside the boundary layer, and is identically equal to 1 for dilute sus-

sensions. Inside the bracket, $f(2; \theta)$ represents the non-equilibrium distortion of the microstructure normalized by the equilibrium microstructure, and is only angular dependent. Physically, as particle approach each other, the boundary layer thickness is $O(Pe^{-1})$ and the strength of the stress for an individual probe-bath encounter is proportional to the probe forcing, $O(Pe)$. Thus, the average stress on the surface of the probe is proportional to the thickness of the boundary layer ($O(Pe^{-1})$), the number density of bath particles inside the boundary layer ($O(Pe^\delta)$), the pair-distribution function around the surface ($g(2; \theta)$), and the strength per probe-bath hydrodynamic encounter ($O(Pe)$). The combination of all these factors sets the high- Pe asymptote of suspension stress in Equation (4.21), and gives rise to the high- Pe scaling $Pe^{0.799}$ in dilute suspension.

In concentrated suspensions, many-body interactions become significant. To bridge the dilute theory and the concentrated suspensions, we consider the hydrodynamic interactions in dense suspensions still in the pair level. In dilute suspensions, one particle can only “see” another and they interact hydrodynamically through the solvent. Thus theoretical solutions of two-body hydrodynamic functions derived by Jeffrey and Onishi [84] are utilized to model particle interactions. In contrast, a pair of particles in concentrated suspensions do not only interact through the solvent, but also are influenced by the intervening particles between them. Here we consider the effect of both intervening particles and solvent together, i.e., we view them as an intermediate medium. Thus particle pairs directly interact through this effective “solvent”. From this perspective, all the formulations in dilute theory still hold. The only difference which characterizes the medium properties are the hydrodynamic mobility functions. In dilute theory, the hydrodynamic couplings only depend on the separation distance between the pair. However, when intervening particles

matter, if considering particle pairs in this intermediate solvent, the couplings also depend on the volume fraction ϕ_b of the intervening particles. Thus, in concentrated suspensions, new pair hydrodynamic mobilities, which are functions of both volume fraction of the suspension and separation distance between the pair, must substitute the two-body hydrodynamic functions from previous analytical study [84]. Zia et al. [150] derived these concentrated mobility functions for a range of volume fractions by stochastically averaging the hydrodynamic couplings of all possible particle pairs in certain configurations via ASD simulations. We utilized these new mobilities functions to develop the scaling theory for suspension stress in the concentrated regime.

As discussed above, the high- Pe asymptote of suspension stress in dilute theory (Equation 4.21) still holds from a view of intermediate medium, but volume fraction matters appropriately in this formulation. In dilute theory, $g^{eq}(2)$ represents the equilibrium pair-distribution function outside the boundary layer. As concentration increases, there is larger probability to find a bath particle outside the boundary layer, thus the equilibrium pair-distribution is also a function of volume fraction, i.e., $g^{eq}(2; \phi_b)$. It can be estimated from the Carnahan-Starling equation of state [36]:

$$g^{eq}(2; \phi_b) = \frac{1 - 0.5\phi}{(1 - \phi)^3}. \quad (4.24)$$

The change of microstructure distortion $f(2; \theta)$ is neglected as concentration increases because the crucial contribution to average stress on the particle surface is the number of bath particles around the surface, which is captured by $g^{eq}(2; \phi_b)$. The non-equilibrium distribution of bath particles surrounded the surface influences the stress sufficiently small.

Furthermore, as shown by the microstructure (Figure 4.3), increasing con-

centration give rise to a higher particle density inside the boundary layer, which implies that the scaling of the suspension stress, Pe^δ , also evolves with volume fraction, i.e., $\delta = \delta(\phi_b)$. As shown in Equation 4.22, δ is a ratio of leading orders of mobility functions transverse to and along the line of centers. Since particle pairs are viewed as interacting through solvent and intervening particles, a new set of concentrated mobility functions derived by Zia et al. [150], which capture the effect of both separation distance and intervening particles is utilized to substitute the pair mobility functions in dilute theory. Thus for an arbitrary concentration, this ratio can be estimated by evaluating the concentrated mobility functions in the limit of particles near contact:

$$\delta(\phi_b) = \frac{W_0(\phi_b, r \rightarrow 2)}{G_1(\phi_b, r \rightarrow 2)}. \quad (4.25)$$

A more careful examination of these two mobility functions for arbitrary concentrations indicate that the leading order term along the line of centers, G_1 , almost keep the same, but the one transverse to the line of centers, W_0 , grows with the increase of concentration. Thus quantitatively, the transverse mobility changes the high- Pe stress scaling. Physically, inside the boundary layer, lubrication interactions dominate. For parallel hydrodynamic couplings, two-body interactions dominate because a third particle is not able to fit in the thin fluid gap between the pair, which makes G_1 keep consistent as concentration increases. However, a third particle placed transverse to the line of centers contributes to the coupling and leads to a three-body hydrodynamic interaction transverse to the line of centers. More importantly, the transverse interaction gives rise to a transverse particle motion, and thus breaks the fore-aft symmetry of pair trajectory, and owes to non-Newtonian rheology. That is, the non-Newtonian rheology arising from hydrodynamic interactions is set by the three-body transverse mobility couplings. Involving all the concentration effects, the

high- Pe scaling of the suspension stress is written as:

$$\frac{\langle \Sigma^{neq} \rangle^{conc}}{n_a k T \phi_b} \sim Pe^{\delta(\phi_b)} g^{eq}(2; \phi_b). \quad (4.26)$$

Remind that the scaling of the dilute theory reads

$$\frac{\langle \Sigma^{neq} \rangle^{dilu}}{n_a k T \phi_b} \sim Pe^{\delta_D} g^{eq}(2; \phi_b \ll 1), \quad (4.27)$$

where D denotes dilute limit and $\delta_D \equiv 0.799$. The equilibrium structure $g^{eq}(2; \phi_b \ll 1) \equiv 1$ in dilute theory. A comparison of Equation 4.26 and Equation 4.27 suggests a scaling theory to bridge the dilute theory and concentrated suspensions:

$$\frac{\langle \Sigma^{neq} \rangle^{conc}}{g^{eq}(2; \phi_b) Pe^{\delta(\phi_b) - \delta_D}} \sim \langle \Sigma^{neq} \rangle^{dilu}. \quad (4.28)$$

In Figure 4.6 we apply this scaling to the parallel and perpendicular normal stress, the first normal stress difference and the osmotic pressure. For high Pe , concentrated stresses with different volume fractions all collapse onto the dilute theory. Thus this validates our idea that the concentrated suspensions can be considered as particle pairs interacting through a medium of intervening particles and solvent, where the formulations are consistent with the dilute theory but concentrated mobilities are utilized to model the medium property.

After providing the scaling theory for high- Pe regime, next we will apply the scaling theory into low- Pe regime. The low- Pe asymptote of the suspension stress is given as

$$\frac{\langle \Sigma^{neq} \rangle}{n_a k T \phi_b} \sim Pe^2 g^{eq}(2; \phi_b \ll 1). \quad (4.29)$$

The low- Pe scaling Pe^2 arises from the entropic recovery of the structure distortion. As shown by the microstructure in Figure 4.3, for weak probe forcing, the particle density near contact is almost consistent with the equilibrium microstructure. Thus the low- Pe scaling keeps unchanged with volume fraction.

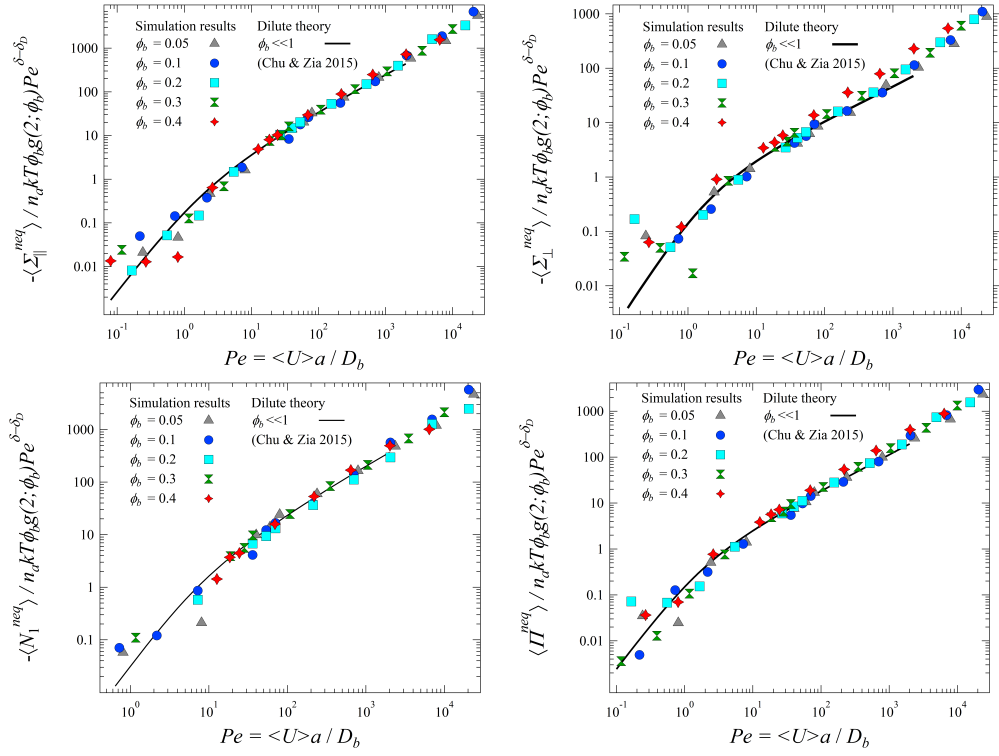


Figure 4.6: High- Pe scaling theory (Eq. 4.28) of suspension stress, as a function of ϕ_b and Pe : (a) parallel normal stress; (b) perpendicular normal stress; (c) first normal stress difference; (d) osmotic pressure. The filled symbols are simulation results. The solid lines are dilute theory from [39].

Similarly to the discussion for the high Pe , a simpler scaling regime is suggested only based on g^{eq} , the equilibrium pair-distribution function just outside the boundary layer:

$$\frac{\langle \Sigma^{neq} \rangle^{conc}}{g^{eq}(2; \phi_b)} \sim \langle \Sigma^{neq} \rangle^{dilu}. \quad (4.30)$$

We select osmotic pressure as an example to show the validity of the low- Pe scaling theory for the suspension stress. Figure 4.7(a-b) represents simulation results (filled symbols) of the osmotic pressure for arbitrary concentrations after applying the scaling theory in Equation 4.30, compared with the dilute theory of Chu and Zia [39] (solid lines). However, disparity can be observed at low Pe . This is because the Brownian contribution to the suspension stress is significant at low Pe , and the variance of Brownian stress is high, as shown by the error

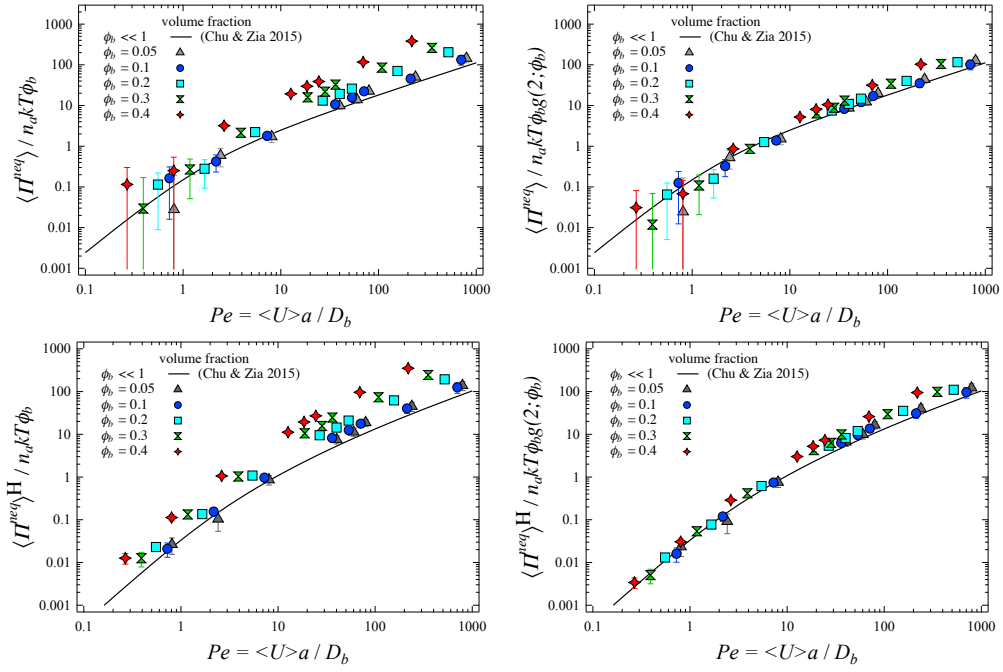


Figure 4.7: Low- Pe scaling (Eq. 4.30) of the osmotic pressure as a function of ϕ_b and Pe : (a) total osmotic pressure before scaling; (b) total osmotic pressure after scaling; (c) hydrodynamic osmotic pressure before scaling; (d) hydrodynamic osmotic pressure after scaling. The filled symbols are simulation results. The solid lines are dilute theory of Chu and Zia [39].

bars in Figure 4.7. To validate the scaling theory, we can justify it by just looking at the hydrodynamic contribution, which is the same order of magnitude as the Brownian part at $Pe \sim O(1)$. In Figure 4.7(c-d), we compare the hydrodynamic osmotic pressure before and after applying the low- Pe scaling. Clearly, with the scaling, hydrodynamic osmotic pressure of all volume fractions collapse onto the dilute theory. Low- Pe regime also shows non-Newtonian behaviors (non-zero suspension stress). However, the unchanged Pe scaling indicates that three-body interactions are not important. This is also observed by the comparison of low- Pe microstructure with the equilibrium structure, as shown by Figure 4.3. In weak probe forcing, the relative motion between particle pairs is small, and the deviation from the fore-aft symmetric trajectory via three-body encounters is negligible. Thus three-body interactions cannot provide qualita-

tive change of suspension stress. The concentration only gives rise to entropic and structural evolution, which is captured by the Carnahan-Starling equation of state. In low- Pe regime, the non-Newtonian rheology mainly arises from the Brownian motion, which destroy the time-reversibility of the trajectory.

In summary, in a suspension with arbitrary concentration, the interactions between probe and bath particles can be modelled as pair interactions through an intermediate medium. The medium models the effect of solvent, as well as the intervening particles between the pair. The properties of the medium is captured by the concentrated hydrodynamic couplings derived by Zia et al. [150], as a function of both suspension concentration and pair separation. In an arbitrary concentration, two effects may influence the suspension stress. The probability for the probe to interact with a bath particle depends on the concentration, and is captured by the equilibrium pair-distribution function, which gives rise to a change of magnitude of the suspension stress. More importantly, for strong probe forcing, the hydrodynamic couplings transverse to the line of centers give rise to break of fore-aft symmetry when three-body encounters. This distortion of microstructure contributes to the non-Newtonian rheology, and leads to the change of high- Pe scaling of the suspension stress. For weak probe forcing, Brownian motion dominates. Because the relative motion of particles is small and quickly recovered by the Brownian motion, the effect of breaking fore-aft symmetry owing to the three-body encounters is weak. Consequently, only pair-distribution function contributes to the change of suspension stress. The non-Newtonian behaviors mainly arise from the Brownian motion. The effect of many-body hydrodynamic interactions may be negligible.

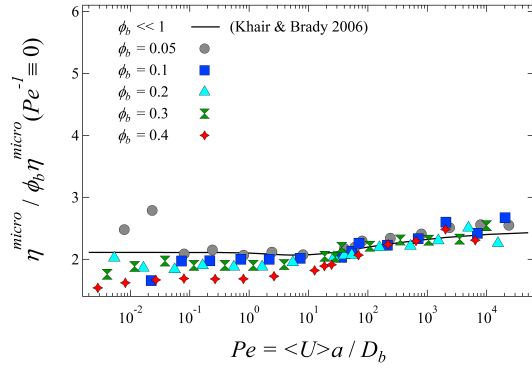


Figure 4.8: Microviscosity as a function of Pe and ϕ_b . The solid line is dilute theory [87]. The filled symbols are the scaled simulation results with finite Pe .

4.5.3.2 Scaling for microviscosity

Khair and Brady [87] derived the high Pe asymptote of the microviscosity in the dilute suspension, $\eta^{micro} \sim \alpha + \beta Pe^{\delta-1}$. Here, α and β are functions of pair mobilities. The constant represents the viscosity arising from interactions outside the boundary layer, whereas the Pe dependent term denotes that inside the boundary layer. In concentrated suspensions, following the idea above, the asymptote formulation still holds. But now α and β are functions of concentrated mobilities. However, these two coefficients are difficult to directly compute due to their complicated relations to the mobilities. As $Pe \rightarrow \infty$, asymmetric structure and thus the boundary layer vanishes, and the microstructure recovers its spherical symmetry. The microviscosity totally arises from the hydrodynamic interactions in the outer region, i.e., α . In simulations, this constant can be measured with setting $Pe = \infty$ by turning off the Brownian motion. This suggests that in high Pe we can scale the microviscosity with the microviscosity in the infinite- Pe limit since it captures the many-body hydrodynamic effects at high Pe .

$$\frac{\eta_{conc}^{micro}(\phi_b)}{\eta_{conc}^{micro}(Pe^{-1} \equiv 0) / \eta_{dilu}^{micro}(Pe^{-1} \equiv 0)} \sim \eta_{dilu}^{micro}(\phi_b \ll 1). \quad (4.31)$$

Figure 4.8 shows the microviscosity comparing with the dilute theory after the scaling above and in high Pe the agreement is excellent.

4.6 Summary and Conclusions

We have studied the microstructure, microviscosity and suspension stress in a fully hydrodynamically interacting dispersion of hard colloidal spheres in the active microrheology for arbitrary concentrations via ASD simulation, and elucidated the effect of three-body interactions on rheological quantities. The behavior was studied for probe forcing from weak to strong, for suspensions from dilute to concentrated. For microstructure, we found that increased particle concentration preserves the symmetry of microstructure for $Pe \sim 1$, and three-body interactions enhance particle density inside the boundary layer more significantly in high Pe than low Pe regime. In dilute theory, particle roughness breaks fore-aft symmetry during a pair encounter, and thus produces non-Newtonian rheology. As a result, all rheological quantities scale as $O(\phi)$. In more concentrated suspensions, many-body hydrodynamic interactions play a role, giving rise to a deviation from the $O(\phi)$ scaling. For suspension stress, instead of suppressing energy storage as two-body hydrodynamic interaction does in dilute theory [39], three-body interactions enhance suspension stress. Two-body hydrodynamic interactions preserve fore-aft symmetry of a pair trajectory and introduce Newtonian rheology. In contrast, three-body hydrodynamic interactions give rise to loss of fore-aft symmetry in the presence of a third particle for a pair trajectory and thus lead to non-Newtonian rheology. Agreement between our scaling theory and simulation results in suspension stress suggests that three-body hydrodynamic interactions are most pronounced when probe

forcing is strong. In strong probe forcing, the relative motion between a pair of particles is large, thus the irreversible trajectory arising from the third particle is pronounced and lead to the non-Newtonian rheology, i.e., normal stress difference and particle pressure. Further study shows that the transverse mobility of the particle pair in the presence of the third particle is responsible for the non-Newtonian rheology, since physically it produces the loss of fore-aft symmetry. In weak probe forcing, the irreversibility from three-body encounters is not important because advection is weak. The residual Brownian motion introduces irreversibility and leads to non-Newtonian rheology. For microviscosity, three-body interactions produce a qualitative change for force-thickening. As $Pe \rightarrow \infty$, the boundary layer is vanishingly thin and only hydrodynamic interactions matter. A scaling via the infinite Pe value signifies the three-body hydrodynamic interactions in high- Pe regime. The quantitative disagreement for viscosity points toward long-range interactions that are still important in concentrated suspensions. Since energy dissipates fast transversely, our scaling theory, which empresses concentrated effect at pair contact, successfully captured the non-Newtonian rheology for suspensions stress. However, the effect of particle motion decays slow as $1/r$ in even concentrated suspensions [150]. As a result, the agreement of viscosity between concentrated and dilute suspensions cannot perform well without considering the concentration effect in long-range interactions. The viscosity in concentrated suspensions may be obtained accurately when directly applying the concentrated mobility functions into the Smoluchowski equation.

CHAPTER 5

LARGE-SCALE ACCELERATED STOKESIAN DYNAMICS SIMULATION WITH MANY-BODY HYDRODYNAMIC INTERACTIONS

5.1 Introduction

Understanding the flow of particles in a fluid has applications in a variety of fields. Biological applications range from the motion of proteins within the cell to the transport of particulates in the respiratory system through the flow of red blood cells in the plasma. Industrial applications are for instance, the flow of paint and ink and in geophysics the sediments transport in rivers and oceans. The formation of soft matter such as colloidal gels [149, 95] is another example of particles suspended in a fluid. In these systems where particles are immersed in a fluid, the particles movements are correlated. When a particle moves, it induces a fluid disturbance which entrains other particles. In turn these particles induce a fluid disturbance too. This fluid-particles coupling and particle-particle coupling, where the solvent mediates the forces between the particles, gives rise to a rich and complex physical behavior [88]. To unravel and shed light on the physics underlying these phenomena different experiments have been developed. Experimental methods to study particulate flow include standard rheology measurements and modern techniques such as optical particle tracking which can provide significant details on the relative motion of particles [113]. Yet, large-scale simulations can provide rich information, insight and understanding of the key relevant physics of colloidal suspensions not available from experiment.

Many different computational approaches can be used to study the dynam-

ics of colloidal suspensions [112]. A broad approach to model and simulate particulate flows is to solve the Navier-Stokes equation over the entirety of the fluid domain. For this purpose the Navier-Stokes equation is discretized on a mesh representing the fluid domain. One strategy within this approach is to impose no-flux and no-slip boundary conditions at the particles surface in a sharp manner. With finite element methods this requires complicated algorithms to generate a mesh which conforms to the particles surfaces [81, 79, 80] and with finite difference methods this requires sophisticated mathematics combined with level set methodology to discretize the boundary condition at the particles interface [68, 98, 74, 25, 37]. These approaches can simulate any domain geometry with any particle shape and even an evolving geometry or shape. However they require to update the mesh and interpolate quantities from one mesh to another at each time step. In addition to the implementation complexity these methods are very challenging for a large number of particles as they require hundreds to thousands of grid points per particle.

A simplification of the sharp-boundary condition philosophy is to solve the Navier-Stokes equation over the entirety of the domain including the particles volume and represent the particles in a fictitious manner. One strategy is to represent the particles through a force density they exert on the fluid localized to a point [128]. Point particles method, can be useful to obtain a first answer on how the particles will affect the fluid flow. However these methods are mostly suitable when the suspended particles are very small compared to the typical length of the flow. Other possible methods which describe the fluid in a fictitious manner are the force coupling method, distributed Lagrange multiplier, immersed boundary method and immersed body method. The force coupling method solves the Navier-Stokes equation by smearing the fluid/particle interface with

a Gaussian shape, and expanding the force density to a force monopole and dipole [108, 145, 109, 107, 47]. The distributed Lagrange multiplier method solves the Navier-Stokes equations and constrains the fluid inside the particles volume to move as a rigid body with Lagrange multiplier functions [69, 70]. Immersed boundary method apply a local momentum impulse [32, 123] and immersed body method apply a forcing inside the particle volume [117, 109] to correct the fluid velocity to account for the particles presence. These methods still require many grid points per particle and more important the lubrication interactions are strongly affected by the specific chosen hyper parameters and therefore in practice can't be captured exactly in non-dilute suspensions at the viscous regime. Other approaches such as Dissipative Particle Dynamics [78] or Lattice-Boltzman [91, 92] do not naturally extend perfectly when viscous forces are dominant and hyper parameters are hard to match.

Approaches to mathematical modeling of particulate flows in an incompressible Newtonian fluid are influenced deeply by the length scales over which particle motions are correlated. In the case of particles suspended in a flowing continuum liquid, such conditions arise from body forces and solvent-mediated interactions. The influence of solvent mediated interactions on correlated particle motion depends on the speed with which and the distance over which momentum is transferred through the fluid. Both are set by the Reynolds number which is the dimensionless strength of flow inertia relative to viscous stress, but equivalently gives the ratio of the dissipative timescale to the advective time scale. In inviscid flows (infinite Re) the disturbance scales as $1/r^3$. However at finite Re fluid/particle interactions are confined to a small region near the fluid/particle interface. The fluid at and near the particle surface is a special dynamical region, a momentum boundary layer in which viscous stress is as

important as inertia, in order to decay far-field flow velocity to the particle velocity. Thus, fluid disturbances induced by the presence of particle boundaries or by particle motion do not strongly influence the motion of other particles as long as they are well outside the momentum boundary layer. Thus mathematical modeling of particulate flows is constrained by the distance over which deformation of flow structure propagates, relative to the length scale of and between suspended particles.

For finite Reynolds number, the boundary layer is inversely proportional to the Re around the particle where the disturbance due to the particle presence is felt. For very high Re (but not infinite) such as turbulent flow there is a ratio of large to small length scales which scales proportionally to the Reynolds number. At the smaller length scale – the so called Kolmogorov length scale – the energy dissipation occurs and is transferred to bigger length scales at a finite speed inversely proportional to the Re number and thus is slow [103]. Moreover, in flow past bodies a long region of turbulent flow is formed behind the body (the wake) and at sufficiently large distances the disturbance decays faster than $1/r$ even inside the wake [103].

On the other side of the spectrum, in viscous suspensions, the Re is small and the dissipative timescale is much smaller than the advective timescale. In fact dissipation occurs instantaneously and there is no lag in the particle correlation. In Stokes flow, $Re = 0$, inertia does not matter, and thus there is no momentum boundary layer; instead, when a hydrodynamic force is exerted on a particle by the fluid, the particles resultant motion entrains fluid with a disturbance that decays quite slowly, as $1/r$, where r is the distance from the center of the particle to a position in the fluid. Moreover, when a particle moves it's ef-

fect is felt immediately everywhere in the domain and information propagates at an infinite speed which leads to strongly correlated particle systems with many-body hydrodynamic interactions. This is captured by the scaling of the Navier-Stokes equation where length and time scales are set by both the flow and the suspended particles where a judicious way to model particle systems at this regime is the Stokes equation which accounts for this scaling. Even in this regime at finite but small Re and high r it is shown than the disturbance decays with $r \times (Re \times r)$ where r is the distance to the particle [103].

On the other hand, when the Reynolds number is nearly zero, one can use the Stokes equation instead of the full Navier-Stokes equation to develop faster numerical techniques. Using the Lorentz reciprocal theorem, the velocity disturbance in the fluid due to the presence of a rigid particle is formulated through an integral over the particle surface. The integral is over the product of the stress tensor with the Stokeslet at the particles boundary [88]. This formulation can be computed with a boundary integral method which breaks the surface of the particle into discrete elements [86, 88, 146]. However this method is expensive as it still requires many elements per particle. In the case that we are interested only in the particles trajectories but still want to account for accurate HI we can use methods which bypass the solution of fluid velocities such as Fast multipole methods (FMM) or Stokesian Dynamics (SD). FMM, which originally developed for electrostatics [73], have been applied to Stokes flow by expanding the surface integral into different terms [132, 120] but would require many terms to include lubrication interaction. SD is based on a multipole representation of the far field and lubrication corrections [28, 55, 31]. In addition, thermal fluctuations of the solvent which are of interest for colloidal suspensions are modeled accurately [26].

FMM and SD share resemblances with molecular dynamics (MD) or Brownian dynamics (BD) simulations as only particles motion is resolved [57]. However BD and MD, when modeling the colloid motion only, do not account for MBHI and lubrication interaction. To account for MBHI with BD/MD would require to add small water molecules $N_w \propto (10^9)N_p$ and to reduce the time step of the simulation to prevent particles overlap to account for colloid-solvent collisions: this would be too slow. Therefore, in order to model particles motion in large scale colloidal suspension with many-body hydrodynamic interactions and Brownian motion we will use SD.

While Stokesian dynamics solves the particles dynamics only it originates rigorously from the Stokes equation and is accurate up to the number of moments it includes in the formulation. Stokesian dynamics has allowed to a better understanding of the physics and rheological properties of suspensions [30, 24, 99, 134, 124]. SD has been extended to include bi-disperse suspension [144] and confined systems [138, 3, 4]. On the computational aspect SD has been accelerated (Accelerated Stokesian Dynamics, ASD) by computing the many-body far-field interaction in the Fourier space [133, 8]. It allows the simulation complexity to get reduced from quadratic to linearithmic with the number of particles. It has enabled to simulate $O(100)$ particles while the original implementation enabled $O(10)$ particles only. However, all ASD design thus far has been serial, limiting system size to a few thousand particles. To illustrate the limitation of serial ASD, we first describe the simulation ability on a single core. On one processor, to simulate $N_p = 500$ particles with $N_x^3 = 32^3$ plane waves, would typically takes one day to simulate 10 Brownian times. If we would like to simulate $N_p = 256,000$ particles with $N_x^3 = 256^3$, it would take more than two years to simulate 10 Brownian times (assuming there is enough memory on a

single core). This is too slow. While recently efforts have been done to leverage advances in new computing architectures none has enabled the study of suspension with $N_p > 10,000$.

Wang and Brady [144] implement the far-field tensor action on a GPU to obtain a $O(10)$ speedup and report results up to $N_p = 3000$. However handling $O(100,000)$ particles would require massive parallelization and will be too slow on a single GPU. While SD has been recently parallelized [34, 35], its quadratic computation complexity still limits its application for large-scale systems. To our best knowledge, the accelerated Stokesian dynamics version, which is linearithmic, has not been implemented on distributed memories. Parallelization of algorithms has gained traction in recent years due to modern distributed memory machines. Active research and development on parallelization is done from fundamental linear algebra [6], Fast Fourier Transforms (FFT) [63, 121] and adaptive mesh refinement [114] to end physical applications. These algorithms have enabled the investigation of a myriad of physical phenomena which would not have been possible on a single CPU. Therefore, in this chapter we propose algorithms for massive parallelization of ASD on distributed memory architecture. The investigation of large-scale suspensions in a parallel environment will enable to answer fundamental scientific questions on colloidal gels and glasses.

The rest of this chapter is organized as follows: in section 5.2 we explain the parallel algorithms in details. We show how the near-field and far-field hydrodynamic interactions and the communication between these two parts are implemented. We also represent the simulation of Brownian motion in parallel scenario, and provide preconditioner techniques to accelerate matrix computation. In section 5.3 validation and convergence results of our code, scaling

performance of our algorithm and as well a simulation of a large-scale hydro-dynamically interacting colloidal suspension forming a gel at early stages are present.

5.2 Parallel Algorithms

5.2.1 Overview

To construct the parallel algorithm, we partition the computation over multi domains and distribute the particles to many cores. While, this will not reduce the overall computation cost, this will definitely reduce the computational time since each processor needs to carry out only a fraction of the overall computational task. For this purpose we parallelized the initial particle configuration generation, the near field iterative solution, the far field iterative solution and the computation of the Brownian force. We also developed an algorithm to communicate the data between the near field and far field algorithms because they are coupled but typically have different parallel layout data structures. We developed or code in C++ using the Message Passing Interface (MPI) library which allows data communication between processors. When parallelizing ASD, challenges arise from different directions. The first is inherent to any parallel code, where careful design is required to minimize communication in order to develop scalable code. The second is natural to any large-scale system where complexity does not increase linearly. In 5.2.2, we discuss the initial particle configuration generation and in 5.2.3 the near field parallelization. In 5.2.4, we discuss in details the far field parallelization and the data communication between the

near field and far field. In 5.2.5 we discuss the methods and strategies to precondition and solve the large scale linear systems obtained in different physical regimes. Finally, in 5.2.6, we discuss the Brownian displacement computation and its parallelization.

5.2.2 Initial Configuration Generation

In this study we generated random configuration for the dilute to the semi dilute regime, i.e $\phi < 0.3$. While it is challenging to generate random configurations even in serial for the concentrated regime [130], we want point here some important remarks about the semi dilute regime in parallel. In serial case, a simple Monte-Carlo simulation is enough: each particle is generated randomly uniformly in the computational domain V ; it checks that no other particle occupy this region; if it does the particle is regenerated until there is no overlap. This process is repeated until all the particles are generated without overlapping with each other. This method is pretty straightforward but scales as $O(N_p^2)$ and is not practical for $N_p \propto 100,000$. In parallel, one possible approach is that each processor will generate particles in a predefined region and then will check overlapping within its own region and neighboring processors. The drawback with this approach is that it generates configurations with low entropy: indeed instead of having a possible number of initial configurations, Ω , proportional to V^{N_p} , we will have only $\Omega \propto (V/P)^{N_p}$ possibilities as illustrated in Figure 5.1, where P is the number of processors we use¹. One simple remedy is to allow each processor to generate particles simultaneously everywhere in the domain. Then an all-to-all communication is required to send all particles to the pro-

¹We use \propto instead of $=$ because we have finite size particles and not point particles. Computing exactly Ω is beyond the scope of this topic.

cessor it belongs to. Finally we check overlap between particles and its close neighbors. The disadvantage is that all-to-all communication is required, i.e each processor may have to communicate with each processor. In addition, as in the serial case, this procedure needs to be repeated iteratively until we reach an overlap free initial configuration. Nevertheless, this allows to generate configurations with $\Omega \propto V^{N_p}$ with a computational complexity of $(\frac{N_p}{P})^2$ which will keep the computational complexity same as a simulation on one processor with $N'_p = N_p/P$ particles. In more details, we use a backtracking algorithm such that for each pair of particles which overlap we regenerate only the particle that did overlap in the previous iteration. The particle that did not overlap in the previous iteration is kept fixed.

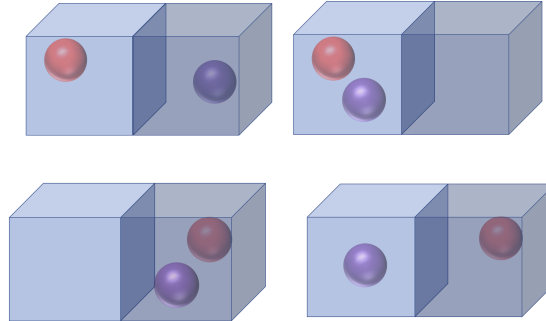


Figure 5.1: A system with two particles and two processors has a higher entropy if each processor can generate particles everywhere in the global domain. Indeed, if each processor is allowed to generate only in its local region the number of possible configurations is proportional to $\frac{V^2}{4}$ where V is the volume of the global domain. That is if the red particle belongs to the light blue processor and the magenta particle belongs to the dark blue processor only the upper left initial configuration can be generated. However if we allow each processor to generate particles anywhere in the global domain, the number of possible configurations is proportional to V^2 and the three other quadrants are also feasible initial configurations. In short if one allows only local generation there is a reduction of entropy proportional to $N_p \times \log P$.

5.2.3 Short-range hydrodynamic interactions

The near-field hydrodynamic interactions are represented by the resistance tensor $\tilde{\mathbf{R}}_{nf}^{FU}$, is derived analytically by Jeffrey and Onishi [84]. Since only two-body short-range hydrodynamic interactions are involved in this near-field portion, particles only interact hydrodynamically with their neighbors and thus $\tilde{\mathbf{R}}_{nf}^{FU}$ is sparse. To construct the sparse matrix in $O(N)$, a neighbor list must be constructed first for each particle, which stores the information of its neighbor particles. The neighbor particles of a particle α are defined as particles within a distance r_c to α . To parallelize this procedure, we follow the algorithm of Plimpton [127], where a 3D domain decomposition is introduced to split the whole simulation box into rectangular subdomains, and each processor assigns a subdomain, as shown in Figure 5.4. Thus, particles near the boundary of the subdomains may have neighbor particles in other processors. To facilitate construction of neighbor list and reduce communication cost, each processor also records information of particles of other processors but close to its boundary. These particles are the so-called ghost particles. To get the information of these ghost particles, following the algorithm of Plimpton [127], each processor (red) communicates with six of its neighbor processors (green) and receives the information of all the ghost particles as described in figure 5.4. Once the neighbor list of each particle is constructed, the near-field sparse matrix ($\tilde{\mathbf{R}}_{nf}^{FU}$ and \mathbf{R}_{nf}^{FE}) operations are implemented using PETSc [6].

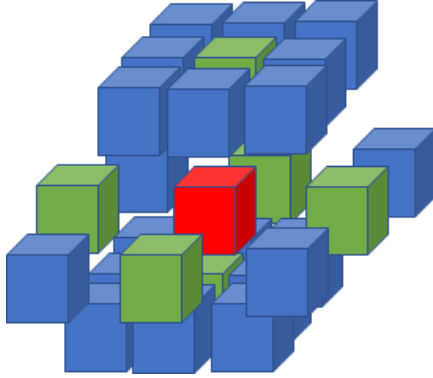


Figure 5.2: The processor grid topology for short range interactions follows a 3D domain decomposition and splits the computational domain in a way to minimize communication among neighborhood processors. Each processor (red) communicates with six of its neighbor (green) and receives the information of all the ghost particles.

5.2.4 Long-range hydrodynamic interactions

Based on Hasimoto work [75] for the periodic solution of the Stokes equation, Sierrou and Brady [133] introduced a fast way to compute the far field mobility matrix action on a vector, i.e $\mathcal{M}^\infty \cdot \mathbf{F}$, without computing the matrix itself. They use an Ewald sum which splits the computation into a real space sum and wave space sum represented as a pair of a Fourier Transform and Inverse Fourier Transform and appropriate operations in between. We review the far field mobility action based on FFT and then discuss its parallelization.

As shown in Equation 1.3, the velocity disturbance $\delta\mathbf{u} = \mathbf{u} - \mathbf{u}^\infty$ is expanded around the particle centers. Sierrou and Brady [133] absorb the torque and the stresslet into the force with a force matching moment method and use the Fourier representation of the Stokeslet to obtain:

$$\delta u_i(\mathbf{r}) = \sum_{\alpha} J_{ij} \cdot F_j^{\alpha} = -\frac{8\pi}{V} \sum_{k \neq 0} \frac{1}{k^4} (\hat{F}_j \cdot k_l k_j - \hat{F}_j k^2) \exp(-i\mathbf{k} \cdot \mathbf{r}), \quad (5.1)$$

where \hat{F} represents the Fourier Transform of the force, $\hat{F} = \mathcal{F}(F)$. Using then the FFT [44] $\mathcal{M}^\infty \cdot F$ can be done in $3N_x^3 \log N_x$ instead of N_x^6 , where N_x is the number of plane waves used in each direction. However, while this sum could be computed with the Fast Fourier Transform, it is unfortunately converging as slow as $1/k^2$. As remedy Sierrou and Brady [133] use the Hasimoto solution [75, 133] to split the computation of $\sum_\alpha J_{ij} \cdot F_j^\alpha$ into two fast converging sums in real space and reciprocal space, respectively. The fluid velocity arising from the real space sum at any point, \mathbf{r} , is given by:

$$\delta u_j^r(\mathbf{r}) = \frac{1}{4\pi\eta} \sum_\alpha F_l^n \left[\frac{-\pi}{\kappa^{3/2}} \phi_{1/2}(\mathbf{r} - \mathbf{r}_\alpha) \|\mathbf{r} - \mathbf{r}_\alpha\|^2 + \kappa^{-1/2} \delta_{jl} + \frac{\pi}{\kappa^{3/2}} \phi_{1/2}(\mathbf{r} - \mathbf{r}_\alpha)_l (\mathbf{r} - \mathbf{r}_\alpha)_j \right], \quad (5.2)$$

where \mathbf{r}_α represents the center of particle α , $\phi_{1/2}(\mathbf{r} - \mathbf{r}_\alpha)$ is an incomplete Γ function and κ is the splitting parameter introduced by Hasimoto [75]. The fluid velocity arising from the wave space sum is given by:

$$\delta u_j^w(\mathbf{r}) = -\frac{8\pi}{V} \sum_{k \neq 0} \frac{1}{k^4} (\hat{F}_l k_l k_j - \hat{F}_j k^2) (1 + \pi\kappa k^2) \exp(-\pi\kappa k^2) \exp(-ik \cdot \mathbf{r}). \quad (5.3)$$

The particle motion is then obtained from the disturbance flow, $\delta\mathbf{u} = \delta\mathbf{u}^r + \delta\mathbf{u}^w$, via the Faxen laws.

The real space interactions have fast Gaussian decay and thus only interactions of neighbor particles are computed. A cutoff r_c is utilized to determine the range of interactions and $\delta\mathbf{u}^r$ is evaluated directly from pairwise summation. The real space computation is local and thus does not require any communication and is highly scalable.

In wave space, we need to compute the FFT of \mathbf{F} , i.e $\mathcal{F}(\mathbf{F}) = \hat{\mathbf{F}}$, from which $\hat{\delta}\mathbf{u}$, the FFT of $\delta\mathbf{u}$ is obtained via Equation 5.3. We then obtain the fluid perturbation velocities with the inverse fast Fourier Transform (IFFT) of $\hat{\delta}\mathbf{u}$, i.e $\delta\mathbf{u} = \mathcal{F}^{-1}(\hat{\delta}\mathbf{u})$. We remark that, the Faxen laws requires not only the fluid perturbation, $\delta\mathbf{u}$, in the xyz directions but also its derivatives, $\nabla\delta\mathbf{u}$, laplacian, $\nabla^2\delta\mathbf{u}$,

and laplacian derivatives, $\nabla \nabla^2 \delta \mathbf{u}$. These can be computed either in the Fourier space or in the real space. To compute $\delta \mathbf{u}$ in Fourier space requires a total of 24 IFFT. The special structure of the Faxen laws and $\nabla \times \nabla^2 = 0$ allows to reduce the number of IFFT to twelve while still computing all the quantities in the Fourier space.

The FFT requires the data in an $1D$ uniform array [44]. Thus, performing a $3D$ FFT is done dimension by dimension and requires values on a $3D$ uniform grid. The near-field and far-field equations are coupled and there is need to send information back and forth between the near and far-field. In our case where the particles do not lay on the grid points there is need to transfer the values from the scattered particles location to the uniform grid (see figure 5.3) and vice versa. This can be done either with a non-uniform FFT (NUFFT) [72] or with the Particle Mesh Ewald (PME) technique [48] as in ASD [133].

In the PME case, \mathbf{F} , the force vector at the particles center needs to be interpolated into \mathbf{f} , the force vector evaluated on an uniform grid as can be seen on figure 5.3. \mathbf{f} is then used to compute $\hat{\mathbf{f}}$ the FFT. This is true also for the Inverse Fourier Transform where the velocities need to be interpolated back from the grid into the particles centers.

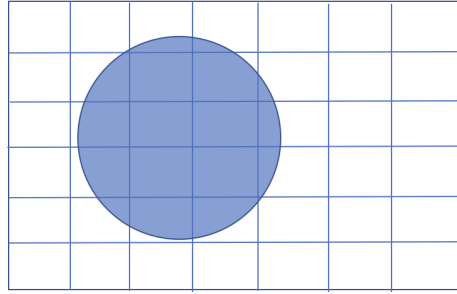


Figure 5.3: Before performing the FFT, the particles forces are interpolated from their center locations to an uniform grid. After performing the Ewald sum and the IFFT, the velocities at the grid points are interpolated back to the particles center location. (This figure is 2D only for illustration: all our simulations are 3D.)

In the PME case as Darden et al. [48], Sierou and Brady [133], we interpolate the values $\delta\mathbf{u}$ at the particles center with a Lagrangian interpolation method: $u_i = \mathcal{P}(u_i)$, $\nabla_j u_i = \mathcal{P}(\nabla_j u_i)$, where \mathcal{P} denotes the Lagrangian interpolation operator. Instead of taking the derivative of the interpolation i.e $\nabla_j u_i = \nabla_j \mathcal{P}(u_i)$ with deteriorates significantly the numerical accuracy, we first differentiate and then interpolate i.e $\nabla_j u_i = \mathcal{P}(\nabla_j u_i)$, where $\nabla_j u_i$ is directly evaluated via \hat{u}_i in wave space. The Lagrangian interpolation requires typically 125 neighboring points, i.e five points in each direction around the dispersed particle.

From a parallelization perspective, PME require to communicate particles' quantities to an uniform grid since the near-field and far-field equations are coupled. There is need of communication because the particles do not share the same domain decomposition as the FFT grid as can be seen in figures 5.4 and 5.5. In serial, it means we need to interpolate. This is because the far-field data is on a grid which is suitable for FFT, while the near-field data is at the particles centers location. In a parallel environment, it means that we also need to com-

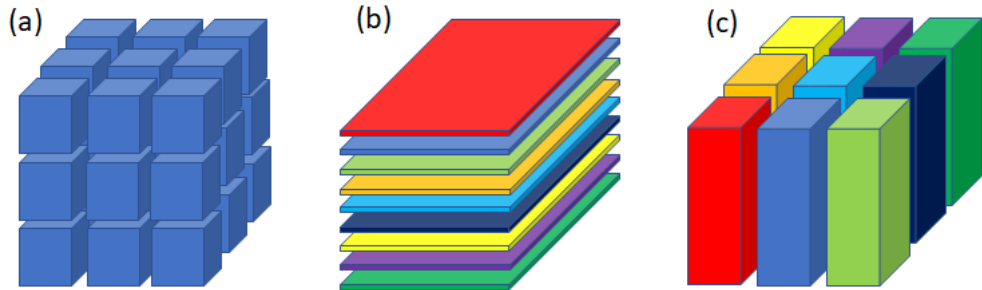


Figure 5.4: Different parallel algorithms use different data layout distribution and have different processor grid topologies. In (a), a 3D domain decomposition which is typically used for short-range interaction. In (b) 1D domain decomposition which is used for the *fftw3*. In (c) a 2D domain decomposition which is used for the *p3dfft*.

municate the data, since the near -field and far-field not only have different data structures but also a different parallel data layout distribution. For this purpose, we designed and implemented efficient communication algorithms between the near and far field parallel data layout structures. Each particle sends values to 146 points on the uniform grid, i.e the scattered data, and each particle receives values from 125 points belonging to the uniform grid, i.e the gathered data. Since the scattered and gathered data typically belong to different processors than the particle, we precompute the number of messages and information each processor needs to send and receive. More precisely for every grid point i the set of particles $\alpha \in S_i = \{\alpha_i^1, \alpha_i^2, \alpha_i^3, \alpha_i^4, \dots\}$ that i needs information from is stored along with their respective processors $p \in U_i = p_i^1, p_i^2, p_i^3, p_i^4, \dots\}$. Then each processor computes these sets for each grid point i it owns and subsequently fuses this information and sends to each processor the particles it would need data from during the iterative solution of ASD. Since the particles are fixed in space during the iterative solution of equation (1.22), we compute it only once every ASD step in the setup phase: it is readily used during the iterative solution of (1.22) and allows to minimize the near field-far field data communication time.

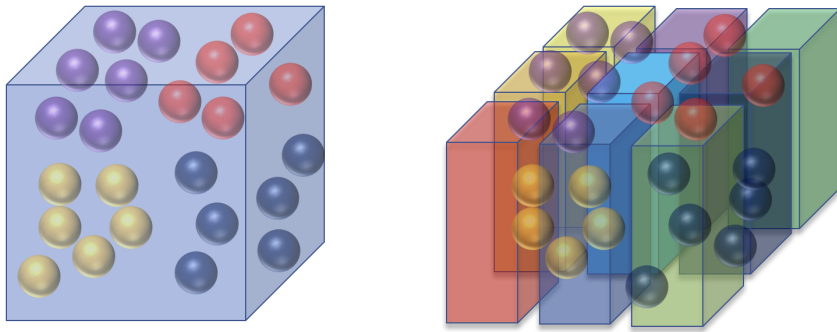


Figure 5.5: Parallel Interpolation: before performing the FFT, the particles velocities need to be interpolated from their center locations to an uniform grid. However, when doing so, interpolation needs to be coupled with communication. As we can see on the figure the particles processor distribution is different than the uniform grid distribution and particles need to be scattered from their previous owner processor to their new owner. In practice, we first interpolate on the grid and then send the data to the appropriate processor. After performing the IFFT and the Ewald sum, the velocities at the grid points need to be interpolated back to the particles center location in a parallel manner as well.

The FFT in 3D is executed dimension by dimension and uses a 1D domain decomposition as illustrated in figure 5.6.

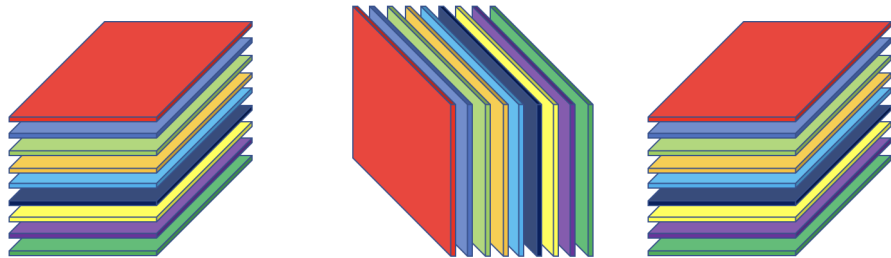


Figure 5.6: FFT parallelization: (1) 2D serial FFTs are performed on the original data layout slab by slab, where each slab belongs fully and only to one processor (2) transpose, i.e communicate the data (3) 1D serial FFTs on transposed data, pencil by pencil, where each pencil belongs fully to one and only processor. (4) The data is transposed back to its original form and in is the Fourier space.

In the *p3dfft* library the parallelization strategy uses a 2D domain decomposition and is similar to *fftw* but uses two transposes. The *p3dfft* parallelization strategy comprises the following steps: (1) 1D serial FFTs are performed on the original data layout pencil by pencil, where each pencil belongs fully and only to one processor; (2) transpose; (3) 1D serial FFTs on transposed data, pencil by pencil, where each pencil belongs fully to one and only processor; (4) transpose again; (5) 1D serial FFTs on transposed data, pencil by pencil, where each pencil belongs fully to one and only processor; (6) The data is transposed back to its original form and in is the Fourier space. In both cases, when alternating the *xyz* directions, there is need to transpose back and forth the data which in parallel requires an all-to-all communication. When we apply subsequently an IFFT to the FFT as in ASD, the transpose back operation is not necessary. We therefore operate on the transposed data to reduce the communication time and we implemented the FFT operations as real to complex and the IFFT operations as complex to real. This significantly decreases the task time. The advantage of *fftw* parallelization over *p3dfft* is that only one transpose is required, while two transpose are required for the *p3dfft*. The advantage of *p3dfft* is that the maximum number of processors possible is $P_{max} = N_x^2$ while for *fftw* $P_{max} = N_x$.

To summarize, the processor domain decomposition for evaluating the short-range particle interactions is cubic and for the FFT either slab by slab as in *fftw* [63] or pencil by pencil as in *p3dfft* [121]. If to use *fftw* we transfer information from a 3D decomposition to a 1D decomposition, alternatively if to use *p3dfft* we transfer information from a 3D decomposition to a 2D decomposition. Both require processors to communicate all their data with other processors for the interpolation to take place. Once the interpolation phase is performed, the 3D FFT on f_x , f_y , and f_z is computed. We denote the interpolation of force mo-

ments on the particles, \mathbf{F} , to forces on the grid, \mathbf{f} , by $\mathcal{P}(\mathbf{F}) = \mathbf{f}$. The communication phase between different domain decompositions is denoted by C , where $f_1 = C_{31}(f_3)$ and $f_2 = C_{32}(f_3)$ represent the communication from a 3D decomposition to a 1D and 2D decomposition, respectively. After the Fourier Transform (\mathcal{F}) are applied, we get $\hat{\mathbf{f}}$, the force on the grid in the Fourier space. Then we apply equation (5.3) to $\hat{\mathbf{f}}$ to get the fluid velocity disturbance in the Fourier space, $\mathcal{G}^w(\mathbf{f}) = \delta\hat{\mathbf{u}}^w$. The inverse Fourier Transform is performed to get the velocity disturbance on the grid in the real space. We then apply an inverse interpolation and communication to get $\delta\mathbf{u}^w$, the fluid velocity disturbance at the particles center. The real-space fluid velocity disturbance, $\delta\mathbf{u}^r$, is directly evaluated via the real-space Stokeslet, given in (5.2). Finally applying Faxen laws (equations (1.4) (1.5) (1.6)) to the velocity disturbance gives the particle motion, \mathbf{U} . This algorithm is summarized in 1.

Algorithm 1: Procedure to compute $\mathbf{U} = \mathcal{M}^\infty \cdot \mathbf{F}$

- I. Perform real-space sum: $\mathcal{G}^r(\mathbf{f}) = \delta\mathbf{u}^r$
 - II. Perform wave-space sum
 1. Perform interpolation locally $\mathbf{f} = \mathcal{P}(\mathbf{F})$
 2. Communicate $f_1 = C_{31}(f_3)$ or $f_2 = C_{32}(f_3)$
 3. Apply FFT $\hat{\mathbf{f}} = \mathcal{F}(\mathbf{f})$
 4. Apply Ewald splitting: $\mathcal{G}^w(\mathbf{f}) = \hat{\mathbf{u}}$
 5. Apply IFFT $\mathbf{u} = \mathcal{F}^{-1}(\hat{\mathbf{u}})$
 6. Apply inverse interpolation to obtain $\delta\mathbf{u}^w = \mathcal{P}^{-1}(\mathbf{u})$
 7. Communicate back $\delta\mathbf{u}_3^w = C_{13}(\delta\mathbf{u}_1^w)$ or $\delta\mathbf{u}_2^w = C_{23}(\delta\mathbf{u}_1^w)$
 - III. Apply Faxen laws: $\mathbf{U} = \mathcal{X}(\delta\mathbf{u}^r + \delta\mathbf{u}^w)$.
-

In summary $\mathcal{M}^\infty \cdot \mathbf{F} = \mathcal{X}(C_{13}\mathcal{P}^{-1}\mathcal{F}^{-1}\mathcal{G}^w\mathcal{F}C_{31}\mathcal{P} + \mathcal{G}^r) \cdot \mathbf{F}$ and $\mathcal{M}^\infty \cdot \mathbf{F} =$

$\chi(C_{23}\mathcal{P}^{-1}\mathcal{F}^{-1}\mathcal{G}^w\mathcal{F}C_{32}\mathcal{P} + \mathcal{G}^r) \cdot \mathbf{F}$ for *fftw* and *p3dfft* respectively.

5.2.5 Near-Field and Far-Field Inverse

To obtain particle dynamics and rheological quantities, we solve (1.22) utilizing iterative methods, such as GMRES. For matrix-free and parallel regime, GMRES, which requires only the matrix-vector multiplication operation, is a natural fit. It also requires the matrix to be positive definite, which is ensured with an appropriate choice of β . We note that we have a nested iteration, where $(\tilde{\mathbf{R}}_{nf}^{FU})^{-1}$, represented as an inner iteration, is solved at each iteration of equation (1.22). This inner iteration is also solved via GMRES. In colloidal suspensions with hydrodynamic interactions, since lubrication interactions are taken into account, the near-field resistance matrix, $\tilde{\mathbf{R}}_{nf}^{FU}$, is usually ill-conditioned. In addition, the condition number of the matrix increases with the number of particles. This problem becomes even more severe as particles get closer, i.e., when we add attractive forces to particles to simulate colloidal gels. The matrix is ill-conditioned because the off-diagonal elements are of the same order as the diagonal elements. Consequently, it gives rise to very slow convergence when solving the linear equations, especially for large-scale systems. To overcome this problem, we introduce a preconditioner to solve $(\tilde{\mathbf{R}}_{nf}^{FU})^{-1}$. However, though using a preconditioner can reduce the number of iterations, it can be computationally expensive to build it. In general one wants a preconditioner fast to build and in the same time to enhance the solver's speed.

In the serial case one good choice is the no-fill incomplete Cholesky (IC0) preconditioning. In IC0, $\mathbf{M} = (\bar{\mathbf{L}}\bar{\mathbf{L}}^T)^{-1} \approx (\tilde{\mathbf{R}}_{nf}^{FU})^{-1}$ serves as preconditioner, where

$\tilde{\mathbf{L}}$ is a lower triangular matrix with the same sparsity pattern as $\tilde{\mathbf{R}}_{nf}^{FU}$ [141] which has been used in ASD [133]. However, for large systems and distributed memories, IC0 may not be the best choice. Firstly the Cholesky decomposition and hence the construction of $\tilde{\mathbf{L}}$ requires a considerable amount of communication between processors on a distributed memory architecture, secondly the solution of the triangular matrix, $\tilde{\mathbf{L}}$, is inherently sequential and its parallelization even with a shared memory paradigm is not trivial [38]. We therefore instead use a sparse approximate inverse (SAI) for preconditioning [23]. The idea of SAI is to use graph theory to predict good sparsity patterns for $(\tilde{\mathbf{R}}_{nf}^{FU})^{-1}$, and build a matrix $M \approx (\tilde{\mathbf{R}}_{nf}^{FU})^{-1}$ such that the Frobenius norm of $\mathbf{I} - \tilde{\mathbf{R}}_{nf}^{FU} M$ is minimized. It has been shown to be easily decomposed into minimization problems for individual rows, which leads to a highly parallel algorithm [23]. The far-field inversion is more complicated since it is a matrix-free and dense linear system and few methods exist which do not extend or work efficiently for every problem [52].

5.2.6 Correlated Brownian motion with hydrodynamic interactions

5.2.6.1 Overview

Stokesian dynamics can include Brownian motion using a stochastic differential equation, where the random movement of the particles originates from the thermal fluctuations in the fluid and is correlated due to the hydrodynamic interactions [8]. $\Delta\mathbf{x}$ occurring within a finite interval Δt is given by [8, 57]:

$$\Delta\mathbf{x} = \sqrt{2}\mathbf{R}_{FU}^{-1/2}\Delta\mathbf{w} + \nabla \cdot \mathbf{R}_{FU}^{-1}(\mathbf{x}(t))\Delta t, \quad (5.4)$$

where $\Delta\mathbf{w} = \int_0^{\Delta t} d\mathbf{w}$ and $d\mathbf{w}$ is a multidimensional uncorrelated Brownian motion. This displacement is subsequently added to the deterministic displacement. The displacement obeys the following statistics $\langle \Delta\mathbf{x}(\Delta t) \rangle = \nabla \cdot \mathbf{R}_{FU}^{-1} \Delta t$ and $\langle \Delta\mathbf{x}(\Delta t) \Delta\mathbf{x}(\Delta t) \rangle = 2\nabla \cdot \mathbf{R}_{FU}^{-1} \Delta t$ consistent with a diffusion equation with configuration dependent tensor $\partial_t p = \partial_i (\mathbf{R}_{ij}^{-1} \partial_j p)$ where $p(\mathbf{r}_i)$ is the N particle distribution function [57]. The term $\mathbf{R}_{FU}^{-1}(\mathbf{x}(t))$ represents the Brownian drift. Mathematically it arises from Taylor expansion of $\mathbf{R}_{FU}(t)$ over time t under Ito interpretation, when solving the stochastic differential equation:

$$d\mathbf{x} = \sqrt{2} \mathbf{R}_{FU}^{-1/2} d\mathbf{w} \quad (5.5)$$

To simulate Brownian motion we follow Banchio and Brady [8] and we evaluate first the Brownian force before obtaining the Brownian displacement. The Brownian force \mathbf{F}^b is built as a random Gaussian vector, which satisfies

$$\langle \mathbf{F}^b \rangle = 0, \quad (5.6)$$

$$\langle \mathbf{F}^b(0) \mathbf{F}^b(t) \rangle = 2 \mathbf{R}_{FU} \delta(t), \quad (5.7)$$

where $\langle \cdot \rangle$ represents an ensemble average over the thermal fluctuations in the fluid, and δ is the delta function. Since the resistance tensor is expressed as an addition of the near-field resistance matrix and the inverse of the far-field mobility, the Brownian force is also expressed as the addition of a near-field portion and a far-field portion,

$$\mathbf{F}^b = \mathbf{F}_{nf}^b + \mathbf{F}_{ff}^b. \quad (5.8)$$

We define the near-field and far-field Brownian force as follows:

$$\langle \mathbf{F}_{nf}^b \rangle = \langle \mathbf{F}_{ff}^b \rangle = 0, \quad (5.9)$$

$$\langle \mathbf{F}_{ff}^b \mathbf{F}_{ff}^b \rangle = 2(\mathbf{M}_{UF}^\infty)^{-1} \quad (5.10)$$

$$\langle \mathbf{F}_{nf}^b \mathbf{F}_{nf}^b \rangle = 2\mathbf{R}_{nf}^{FU} \quad (5.11)$$

and the covariance between \mathbf{F}_{nf}^b and \mathbf{F}_{ff}^b is zero. $\Delta\mathbf{x}$ is then obtained from $\Delta\mathbf{x} = \mathbf{R}_{FU}^{-1}(\mathbf{x}(t)) \cdot \mathbf{F}_b(\mathbf{x}(t))\Delta t$. While it is tentative to work directly with $\Delta\mathbf{x}$, i.e., with the mobility, instead of \mathbf{F} , i.e., the resistance, it is unfortunately computationally very challenging. The reason is that the resistance matrix is additive, $\langle (\mathbf{R}_{nf}^{1/2}\Psi_1 + \mathcal{M}^{\infty-1/2}\Psi_2)^T(\mathbf{R}_{nf}^{1/2}\Psi_1 + \mathcal{M}^{\infty-1/2}\Psi_2) \rangle = \mathbf{R}_{nf} + \mathcal{M}^{\infty-1} = \mathcal{R}$, where Ψ_1 and Ψ_2 are stochastic vectors with zero mean and unit variance. However, the mobility matrix is not additive, i.e., $\langle (\mathbf{R}_{nf}^{-1/2}\Psi_1 + \mathcal{M}^{\infty1/2}\Psi_2)^T(\mathbf{R}_{nf}^{-1/2}\Psi_1 + \mathcal{M}^{\infty1/2}\Psi_2) \rangle = \mathbf{R}_{nf}^{-1} + \mathcal{M}^{\infty} \neq \mathcal{M}$ [55]. We note that since we work with \mathbf{F} and not $\Delta\mathbf{x}$, and thus need $\mathcal{M}^{\infty-1}$, splitting the computation of the Brownian force into the wave space and real space portion respectively is also not possible, because $\langle (\mathbf{M}_w^{-1/2}\Psi_1 + \mathbf{M}_r^{-1/2}\Psi_2)^T(\mathbf{M}_w^{-1/2}\Psi_1 + \mathbf{M}_r^{-1/2}\Psi_2) \rangle = \mathbf{M}_w^{-1} + \mathbf{M}_r^{-1} \neq \mathcal{M}^{\infty-1}$, where \mathbf{M}_w represents the wave-space portion of the far-field mobility, and \mathbf{M}_r denotes the corresponding real-space portion.

However, one can find ways to leverage the split of the wave-space and real space parts by using uncorrelated stochastic vectors Ψ_1 and Ψ_2 :

$$\langle (\mathbf{M}_w^{1/2}\Psi_1 + \mathbf{M}_r^{1/2}\Psi_2)^T(\mathbf{M}_w^{1/2}\Psi_1 + \mathbf{M}_r^{1/2}\Psi_2) \rangle = \mathbf{M}_w^1 + \mathbf{M}_r^1 = \mathcal{M}_{\infty}. \quad (5.12)$$

But, in ASD, since we need to add the near field which comes only in the resistance form:

$$(\mathbf{R}_{nf} + \mathcal{M}_{\infty}^{-1})^{1/2}\Psi = \mathbf{R}_{nf}^{1/2}\Psi_{nf} + (\mathcal{M}_{\infty}^{-1/2})\Psi_{ff} = \mathbf{F}_{nf}^b + \mathbf{F}_{ff}^b = \mathbf{F}_b. \quad (5.13)$$

with the desired statistical properties. We then solve $\mathbf{R} \cdot \mathbf{U}_b = \mathbf{F}_b$ to get $\mathbf{U}_b = \mathbf{R}^{-1/2}\Psi$. Now $\mathbf{R}_{nf}^{1/2} \cdot \Psi_{nf}$ is obtained by taking the square root block-wise as described later. To compute $\mathcal{M}_{\infty}^{-1/2} \cdot \Psi_{ff} = \mathbf{F}_{ff}^b$, we will project $\mathcal{M}_{\infty}^{-1/2}$ to a smaller subspace.

5.2.6.2 Near-Field Brownian force

We follow the approach of Banchio and Brady [8] and extend it to a parallel setting. We construct the 12×12 near-field resistance matrix $\mathbf{R}_{FU}^{nf,(i,j)}$ for each pair of colloids, (i, j) . Then we directly compute the square root of the matrix via Cholesky decomposition, $\mathbf{R}_{FU}^{nf,(i,j)} = \mathbf{L}^{(i,j),T} \mathbf{L}^{(i,j)}$. In parallel regime, the particles are distributed among processors. The contribution of local particles include interactions with other nearby local particles and ghost particles. The interactions with the ghost particles are stored and packed first locally and at the end sent to the belonging processors during the assembly process. We define the set of particle pairs, $\mathcal{S}(p)$, which includes all the near-neighbor pairs for all the local particles in processor p , i.e., $\mathcal{S} = \{(i, j) | i \in p, j \in N(i)\}$, where $N(i)$ represents the colloids in i 's near-neighbor list. We define the assembly operation, \mathbb{A} , which gathers forces computed from individual pair interactions in each processor to a force vector. Thus the near-field Brownian force is given by:

$$\mathbf{F} = \bigcup_{p=1}^P \bigcup_{(i,j) \in \mathcal{S}(p)} \mathbf{L}^{(i,j)} \Psi^{(i,j)}, \quad (5.14)$$

where P denotes the total number of processors, $\Psi^{(i,j)}$ is a 12×1 stochastic vector of pair (i, j) with zero mean and unit variance. Note that even we evaluate the interactions of particle pair (i, j) and (j, i) separately with different gaussian variables, the statistics is still invariant because the stochastic vectors are uncorrelated.

5.2.6.3 Far-field Brownian force

To simulate far-field Brownian force, one should evaluate $(\mathbf{M}_{UF}^\infty)^{-1/2}$, which is not tractable directly since the far-field mobility matrix \mathbf{M}^∞ is never constructed

from the matrix-free algorithm. Banchio and Brady [8] evaluate the far-field Brownian force by solving the full far-field mobility directly,

$$\begin{bmatrix} \mathbf{F}_{ff}^b \\ S_{ran} \end{bmatrix} = \sqrt{\frac{2}{\Delta t}} (\mathbf{M}^\infty)^{-1/2} \cdot \boldsymbol{\psi}_{ff}, \quad (5.15)$$

where $\boldsymbol{\psi}_{ff}$ is a $11N$ Gaussian random variable independent of $\boldsymbol{\psi}_{nf}$.

This requires to solve the linear system such as $(\mathbf{M}^\infty)^{1/2} \cdot \mathbf{x} = \mathbf{y}$. The linear system is again solved via iterative methods, which requires the matrix-vector multiplication, $(\mathbf{M}^\infty)^{1/2} \cdot \mathbf{x}$. But this matrix-vector multiplication itself is a complicated computation. We compute it utilizing the Lanczos process developed by Ando et al. [2]. The Lanczos process computes $(\mathbf{M}^\infty)^{1/2} \cdot \mathbf{x}$ by approximating $(\mathbf{M}^\infty)^{1/2}$ on a much smaller subspace. The Lanczos process itself is an iterative method, which requires the matrix-vector multiplication $\mathbf{M}^\infty \cdot \mathbf{x}$. The number of iterations needed in the Lanczos process depends on the size of the subspace utilized to approximate \mathbf{M}^∞ . As the number of particles grows, the condition number of \mathbf{M}^∞ grows as well, and the subspace size to obtain a good approximation of \mathbf{M}^∞ increases accordingly. Thus, the complexity is not $O(N \log N)$ as $\mathbf{M}^\infty \cdot \mathbf{x}$. In practice, for large-scale particle systems bigger than $O(10^5)$, it is convenient to use a diagonal approximation of \mathbf{M}^∞ for the computation of \mathbf{F}_{ff}^b . This approximated algorithm is named ASDB-nf, and is described in details in Banchio and Brady [8].

5.2.6.4 Brownian drift

To compute the Brownian drift, we utilize the elegant approximation of Banchio and Brady [8]. It requires to advect the particles and reconstruct the resistance matrix. In the parallel regime, it requires to redistribute the particles

among processors and updated accordingly all the parallel data structures. To avoid this and minimize the communication, we advect locally both the local and ghost particles. This allows an efficient parallel implementation of the Brownian drift term.

5.3 Results

5.3.1 Validation results

To test the validity of the parallel algorithms we developed, we compare several results with the theory and a well validated serial code [133, 8, 150, 136]. The high-frequency viscosity, η'_∞ , is the “intrinsic” viscosity of a suspension arising from the presence of the no-slip surfaces of the particles. In the context of sheared suspensions, it is the flow-independent, off-diagonal particle-phase shear stress, Σ_{xy}^p , normalized by the flow rate E_{xy} , and solvent viscosity η ,

$$\eta'_\infty = \frac{\Sigma_{xy}^p}{2\eta E_{xy}}. \quad (5.16)$$

Thus the high-frequency viscosity is computed by imposing a unit simple shear flow where many particle configurations have been sampled to obtain statistical reliable result. Figure 5.7 on the left shows the high-frequency viscosity computation as a function of volume fraction with our parallel code and demonstrates that the results of sequential and parallelized program are in agreement.

The tendency for isotropic expansion or contraction of the particle phase is

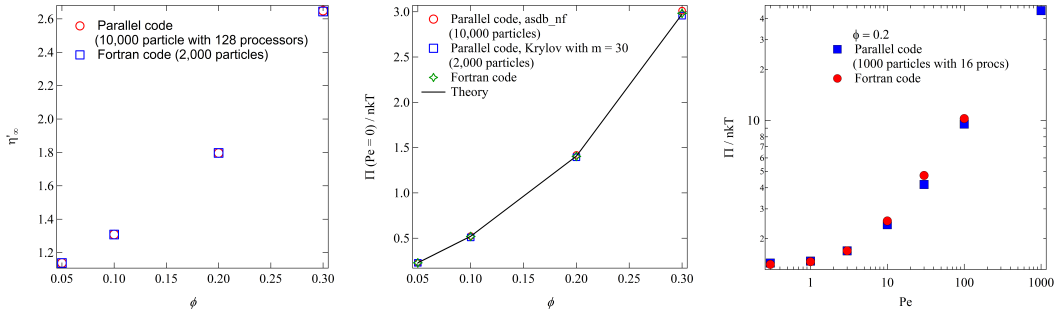


Figure 5.7: These graphs compare physical observables between a validated legacy Fortran serial code and our recently developed parallel code. On the left, high frequency viscosity as a function of volume fraction computed in the absence of Brownian motion and a constant shear such as $Pe = 1$: the parallel code uses 128 processors for $N_p = 10,000$ particles. On the middle, equilibrium osmotic pressure as a function of volume fraction using ASDB (2,000 particles with 16 processors) and ASDB-nf (10,000 particles with 128 processors) in the absence of shear such as $Pe = 0$. On the right non-equilibrium osmotic pressure as a function of Peclet number with ASDB (1,000 particles with 16 processors).

described by the osmotic pressure defined by:

$$\langle \Pi \rangle = -\frac{1}{3} \mathbf{I} : \langle \Sigma^P \rangle, \quad (5.17)$$

where $\langle \Sigma^P \rangle$ represents the particle-phase stress. The stresses are ensemble averaged over the whole volume V containing N particles, denoted as $\langle \cdot \rangle$. Generally, the particle-phase stress, $\langle \Sigma^P \rangle$, is written as

$$\langle \Sigma^P \rangle = -nkT\mathbf{I} + n(\langle \mathbf{S}^H \rangle + \langle \mathbf{S}^B \rangle + \langle \mathbf{S}^P \rangle), \quad (5.18)$$

where $n = N/V$ is the particle density, $-nkT\mathbf{I}$ represents the equilibrium contribution arising from thermal fluctuations of Brownian motion of particles. The remaining terms represent the particle-phase stress arising from hydrodynamic interactions, where \mathbf{S}^H , \mathbf{S}^B and \mathbf{S}^P denotes the hydrodynamic, Brownian and interparticle force stresslets, respectively. The equilibrium osmotic pressure, Π^{equ} only arises from the thermal fluctuations of Brownian motion. In ASD simulation, it is measured in an equilibrium suspension with hard-sphere interparticle potential. In this case, $\mathbf{S}^H \equiv 0$ since there is no imposed flow and \mathbf{S}^P also

vanishes because the hard-sphere potential naturally prevents particles from touching each other and gives rise to zero interparticle force. Thus the osmotic pressure arises from \mathbf{S}^B only. In ASD, it is measured via

$$\langle \mathbf{S}^B \rangle = -kT \langle \nabla \cdot (\mathbf{R}_{SU} \cdot \mathbf{R}_{FU}^{-1}) \rangle. \quad (5.19)$$

Figure 5.7 on the middle represents the equilibrium osmotic pressure as a function of volume fraction. The agreement between parallelized, sequential (Fortran code) simulation results, and theory is excellent. The non-equilibrium osmotic pressure is measured under simple flow, where the strength of the flow is defined by the Peclet number, $Pe = 6\pi\eta a^3\dot{\gamma}/kT$, where $\dot{\gamma}$ is the magnitude of the shear rate. In this case, the imposed flow introduces non-zero hydrodynamic stresslet, \mathbf{S}^H , as well as \mathbf{S}^B . The hydrodynamic stresslet is computed via

$$\langle \mathbf{S}^H \rangle = -\langle \mathbf{R}_{SU} \cdot \mathbf{R}_{FU}^{-1} \cdot \mathbf{R}_{FE} - \mathbf{R}_{SE} \rangle : \langle \mathbf{E} \rangle. \quad (5.20)$$

Figure 5.7 on the right shows the validation results of osmotic pressure for volume fraction 0.2, with Pe ranging from 0.3 to 1000. Also in this case, a good agreement between the benchmark code and our code is observed.

5.3.2 Scaling Results

In this section we present scaling with the number of particles N_p of our parallel code. In all the cases presented in this section except stated otherwise, the timing presented are for a suspension with a concentration $\phi = 0.2$, an inter particle Morse potential (see equation 5.21) between the particles and the Brownian motion is resolved with ASDB-nf. The inter particle force is computed pairwise in an additive fashion with the close neighbors as $\mathbf{F}^P = -\frac{\partial V_{Morse}}{\partial r} \hat{\mathbf{r}}$. The

case of pure shear flow is presented at the end of this subsection. In figure 5.8 is presented scaling on the super computer Stampede 1 with sandy bridge processors and in figure 5.10 scaling on the super computer Stampede 2 with modern knights landing (the so-called knl) processors. In both cases, our code scales with the number of processors. In figure 5.8 on the left are presented the times for different number of particles and different number of processors. In this figure we show results for $N_p = 200$ with $P = 1, 2, 4, 8$; $N_p = 1600$ with $P = 1, 2, 4, 8, 16, 32, 64$; $N_p = 12,800$ with $P = 1, 2, 4, 8, 16, 32, 64$ and $N_p = 102,400$ with $P = 8, 16, 32, 64, 64, 128, 256$. Each time that we double N_x , i.e $N_x = 2N_x$ we multiply by eight the number of particles i.e $N_p = 2^3N_p$. The graph on the right of figure 5.8 shows the strong scaling in the case of $N_p = 102,400$, $N_x = 256$ and $P = 8, 16, 32, 64, 128, 256, 512, 1024$. We note that in this case for $P = 1, 2, 4$ the memory was insufficient to carry the simulations. For $P = 8, 16, 32, 64, 128$ the time plotted is the one obtained with *fftw* while for $P = 256, 512, 1024$ is plotted the time obtained with *p3dfft*. *fftw* scales up to $P = N_x$ so for $P = 512, 1024$ we do not have the choice but to use *p3dfft*. In this graph we show that for a suspension with $N_p = 102,400$ and $\phi = 0.2$, despite the complicated nature of ASD we are able to obtain a significant speed up of ≈ 300 by using 1024 processors indeed with eight processors the cost of an ASD step is $t_{wall} \approx 200\text{seconds}$ while for $P = 1024$ $t_{wall} \approx 5\text{seconds}$ where the time step of the simulation is $\Delta t = 0.001$ ².

In figure 5.9 we show timing results for *p3dfft*, which uses a 2D decomposition where on the x axis is the number of processors P_x in the x direction and

²While the efficiency decreases with the number of processors, in practice there is still a high incentive to scale up to 1,000 processors. For instance if the efficiency to double each time the number of processors is 0.9, the overall efficiency at $2^{10} \approx 1,000$ processors is $0.9^{10} \approx 0.35$. Yet one would still want to double from 500 to 1000. One would not double the number of processors when doubling will cause a sharp drop in efficiency.

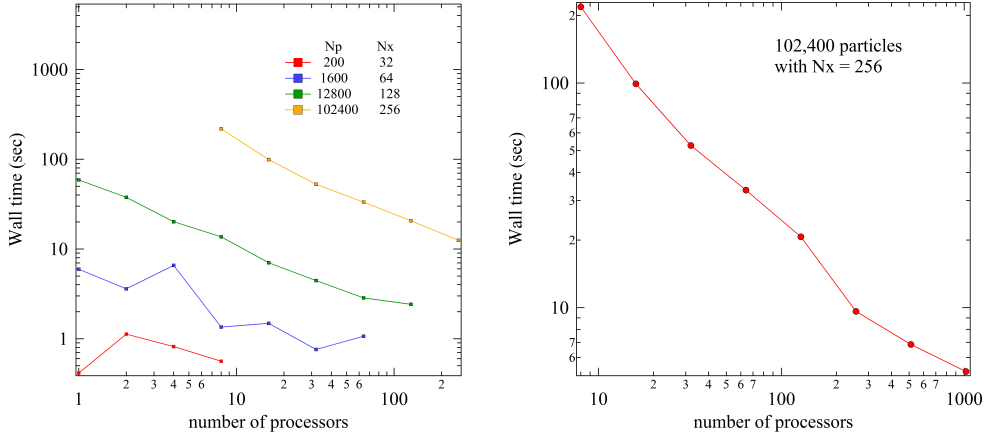


Figure 5.8: Strong scaling of one ASD step on Stampede1 with $\phi = 0.2$, an inter particle force with a Morse potential of strength $V_0 = 5$ and Brownian motion with ASDB-nf. On the left is described the scaling for different number of processors

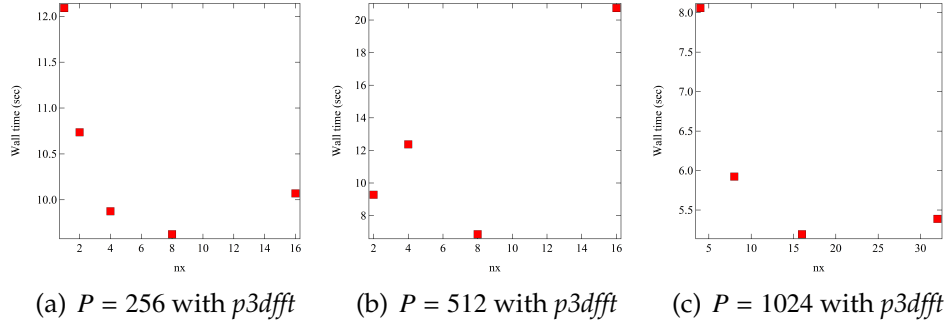


Figure 5.9: Speed up for different grid topologies for $N_p = 102,400, N_x = 256$

$P_y = P/P_x$ the number of processors in the y direction is deduced automatically. For $P = 256$, $P_x = 1, 2, 4, 8, 16$, for $P = 512$ $P_x = 2, 4, 8, 16, 32$ and $P = 1024$ $P_x = 4, 8, 16, 32, 64$. In the later cases where $P > N_x$, P_x does not start from one because we need $P_y \leq N_x$ as we can't use more processors in one direction than the number of layers. When $P_x > 1$ we already have a 2D decomposition and we can see on these figures that in all cases the processor topology has a significant effect on the overall timing. For $P = 256$, $P_x = 8, P_y = 32$ is the optimal choice,

for $P = 512$, $P_x = 8$, $P_y = 64$ and for $P = 1024$, $P_y = 16$, $P_z = 64$ are the optimal choices. We note that from cluster to cluster these numbers can change since the optimal choice is a function of communication time among processors, computation time on a single processor and cluster topology, i.e how the processors in the cluster are physically placed. This obviously depends on which cluster these simulations are runt. We can see that in all cases the time wall dependence on P_x is not monotonic. A judicious choice of the grid topology is required to enhance performance. While an a priori estimation is useful to understand the results, since it is hardware dependent and thus cluster dependent the best is to run a timing analysis for different grid topologies for a specific case before running a long simulation. We know show that our code scales as well on Stampede2. In figure 5.10(d) on the right are presented the times for different number of particles and different number of processors when we use *fftw* for the FFT computations when $N_x > P$ and *p3dfft* when $N_x \leq P$. N_x is the number of plane waves used in each direction for the FFT and P is the number of processors.

We can see that as the number of particles N_p get bigger the parallelization is more efficient. On Stampede1, in the case of $N_p = 200$ we can't even get a speed up by using more than one processor. This is because the communication is more expensive than the gain due to adding processors for the task. When the task is big enough adding processors is more beneficial and the gain due to the parallelization of the computation parts overcomes the communication cost. However even for a big task it will reach a point when the communication cost penalty is heavier than the parallelization gain. The dominant computation parts are the matrix multiplication in the near field part, the computation part in the FFT and the actual interpolation in the interpolation part. The dominant communication parts are the neighboring processors communication in the ma-

trix multiplication of the near field sparse solver, the communications part of the FFT and the communication when we transit from one topology to another and back in the interpolation part.

Figures 5.10(a),(b) and (c) show the strong scaling in the case of $N_p = 12,800, N_x = 128, N_p = 102,400, N_x = 256$ and $N_p = 819,200, N_x = 512$ respectively for the different part of the algorithm: the near field, the FFT, the interpolation, the setup and the real space of each time step. The near field is dominated by computation and communication among neighboring processors which comprises only ghost nodes values exchange. On the other hand interpolation is dominated by all-to-all communication and the computation part is not significant as it is $O(N_p)$. The FFT part is dominated by both computation and all-to-all communication as both these parts are significant in this case. The setup part requires communication but is called only once at each time step and therefore small. The real space part while being significant for a small number of processors is almost insignificant as the number of processors increases. This is because the real space is a local computation which does not require any communication. Fortunately enough our parallel solver which is a combination of these five steps, i.e, near-field, FFT, interpolation, set up and real space still overall has good scaling properties. In figures 5.10(a),(b), the real space computation is as dominant as the FFT on one processor, to become the less significant as the number of processor increases. On the other hand, the near field starts smaller than the interpolation to become bigger at the end. This is because in the interpolation the information required to communicate overall among all the processors remains constant as the number of processor increases while for the near field since the processor's volume shrinks the amount of processors which requires information from each processor to account for the short range

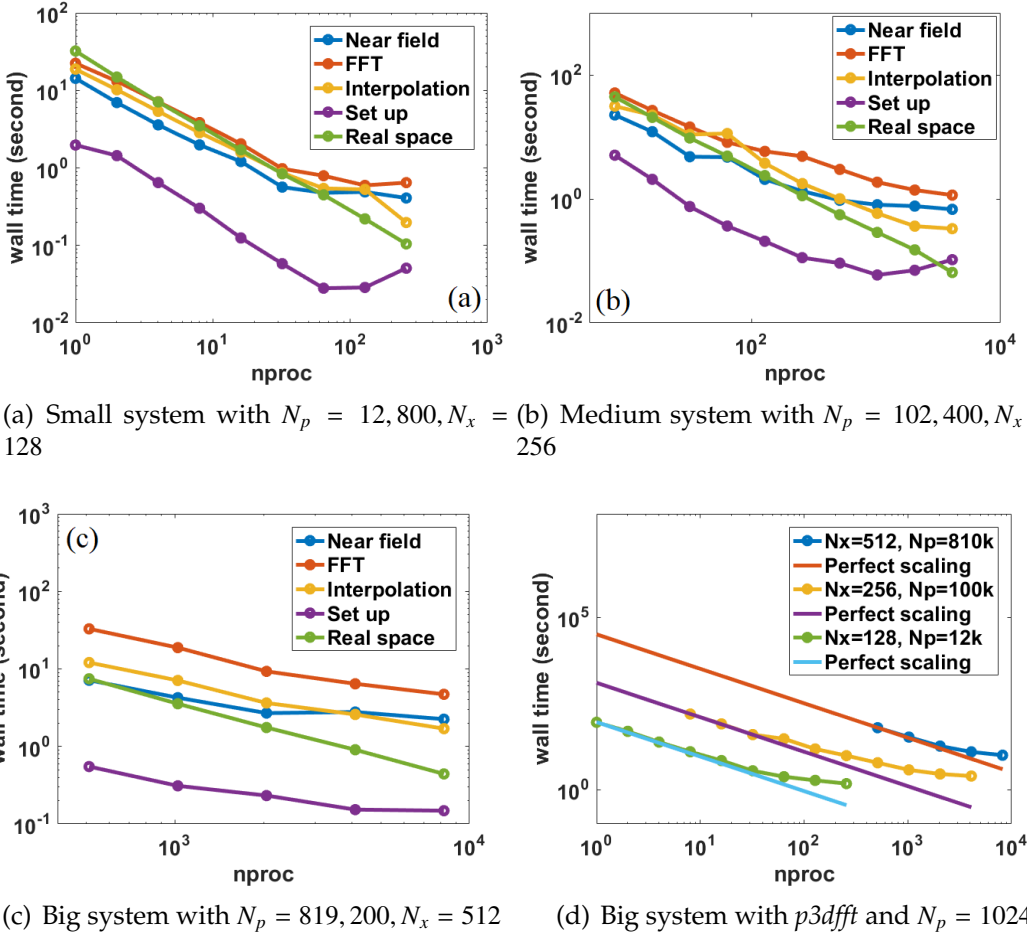


Figure 5.10: Strong scaling of one ASD step on Stampede1 with $\phi = 0.2$, an inter particle force with a Morse potential of strength $V_0 = 5$ and Brownian motion with ASDB-nf.

hydrodynamics increases. Next we discuss in general large-scale simulations regardless of the parallelization followed by the parallelization of shear flow.

We want understand the behavior of the condition number of our different linear systems and thus the number of iterations required to solve them. Rewriting equation (1.22) as $\mathcal{S} \cdot \mathcal{F}^{ff} = \mathcal{B}$, the number of iterations to solve equation (1.22) depends on the condition number of \mathcal{S} , i.e $\kappa(\mathcal{S})$.

The behavior of the condition number of the far-field $\kappa(\mathcal{M}^\infty) = \lambda_{max}/\lambda_{min}$

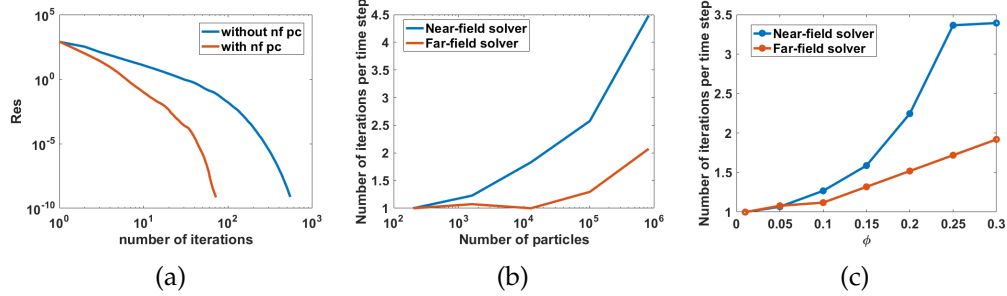


Figure 5.11: In the left, the residual obtained as function of the number of iterations during the near-field inversion. In the middle and left the number of iterations required to invert the ASD linear system as function of the number of particles and as function of the concentration (values are normalized s.t first value is one). The parameters are: (a) $\phi = 0.2, N = 102,400$; (b) $\phi = 0.2$; (c) $N = 102,400$ and an inter particle force with $V_0 = 5$ in all cases and Brownian force.

can be understood as follows. $\lambda_{min} = \frac{1}{6\pi\eta a}$ for uncorrelated particle motion and $\lambda_{max} \propto \frac{1}{\eta L}N$. For a random suspension $L \propto \frac{1}{\phi^{1/3}a}N^{1/3}$ such that $\frac{\lambda_{max}}{\lambda_{min}} \propto N^{2/3}C(\phi^{1/3})$. For gels and polymers L would scale differently but κ will still increase with the number of particles. We now analyze the condition number of the near-field. As particles get closer together the lubrication effect becomes important and the off-diagonal elements of the resistance matrix get bigger. At glance, the near-field depends on the close by particles only and one might be attempted to think that therefore by increasing the number of particles the condition number will not change much. However it does increase. As the number of particles increases, the entropy increases and the probability to find a single pair of particles closer is in fact simply higher. The probability to have a single pair at a given distance is invariant with the number of particles but we simply have more pairs and therefore the higher probability. Secondly the particles dependencies is still more complicated. However, it is important to note that in \mathcal{S} is hidden a complicated operator which combines one far-field matrix-free action and one near-field inversion. In figure 5.11 (a) we show the effect of the number of particles on the *total* number of iterations of the near-field solver required for

applying \mathcal{S} when solving equation (1.22). In figure 5.11(a), it shown that the preconditioning of the near field linear system is critical for high performance for large scale simulations with hydrodynamic and inter particle interaction. The no preconditioned system converges in size of orders more iterations. In figure 5.11 (b) we show the effect of the number of particles on the number iterations required for solving equation (1.22) which is in fact also the required number of far-field matrix-free actions. In figure 5.11 (c) we see that the number of iterations required to invert the linear system increases as well with the concentration. In addition the near-field solver computation time becomes more dominant as the concentration increases.

Finally, we show in figure 5.12 that our code also scales in the case of a shear simulation. In a shear simulation, the computational box is sheared with a rate of $\dot{\gamma} = 1$. On a parallelization perspective, it means that all the subdomains belonging to the different processors are sheared and that the physical distance between the processors changes. This change of processor-processor distance needs to be taken into account when computing the short-range interaction. More saddle, when the box is sheared at $\pi/4$ the box returns to its original form. This is a sudden change of particles location distance and the algorithm described in the near-field section is unable to exchange particles with neighbor communication only. To remedy to it, each time that the box returns to its original form, we perform an all-to-all communication among the processors. Since this occurs only once every $O(10^3)$ ASD steps it is not significant. In figure 5.12 we can see that for a shear simulation a significant speedup is obtained up to 8,192 processors before reaching a plateau at 16,384 processors.

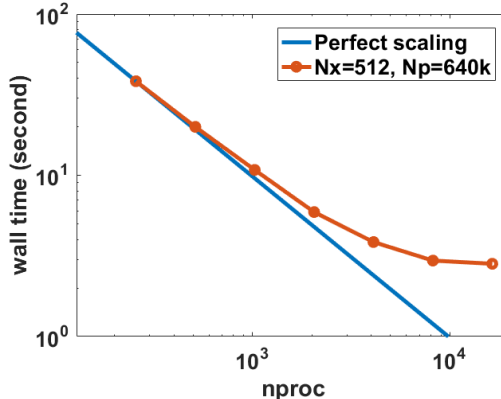


Figure 5.12: Scaling of a shear simulation with the number of processors. In a shear simulation the box is typically sheared until it reaches an angle of $\pi/4$. At this point the box returns to its original form and the shear component is removed from the particles position and the simulation continues from there. On a parallelization perspective, it means that particles will probably migrate by a distance higher than one processor. An algorithm based on neighbor communication only can not remedy to it. Instead each time that the box transits from $\gamma = \pi/4$ to $\gamma = 0$, an all-to-all communication between all the processors occurs. The parameters are $\phi = 0.18, N = 640,000, Pe = 1, N_x = 512$ and no Brownian force and no inter particle force

5.3.3 Large-scale dynamic simulation example: colloidal gels

As an example, we choose to study the gelation of a large-scale colloidal suspension. In a gel of moderate volume fraction, particles attract one another, which gives rise to phase separation into particle-rich and particle-poor regions. Such separation slows or becomes arrested, resulting in the formation of a space-spanning network of colloids. The attractive force between the particles is modeled with a Morse potential:

$$V_{Morse}(r) = V_0(2e^{-\kappa(r-2a)} - e^{-2\kappa(r-2a)}), \quad (5.21)$$

where V_0 is the strength of the attraction at the minimum and κ^{-1} is its range. Figure 5.13 shows the evolution of a gel of 102,400 particles. Particles are colored to indicate the number of neighboring or bonded particles within the dis-

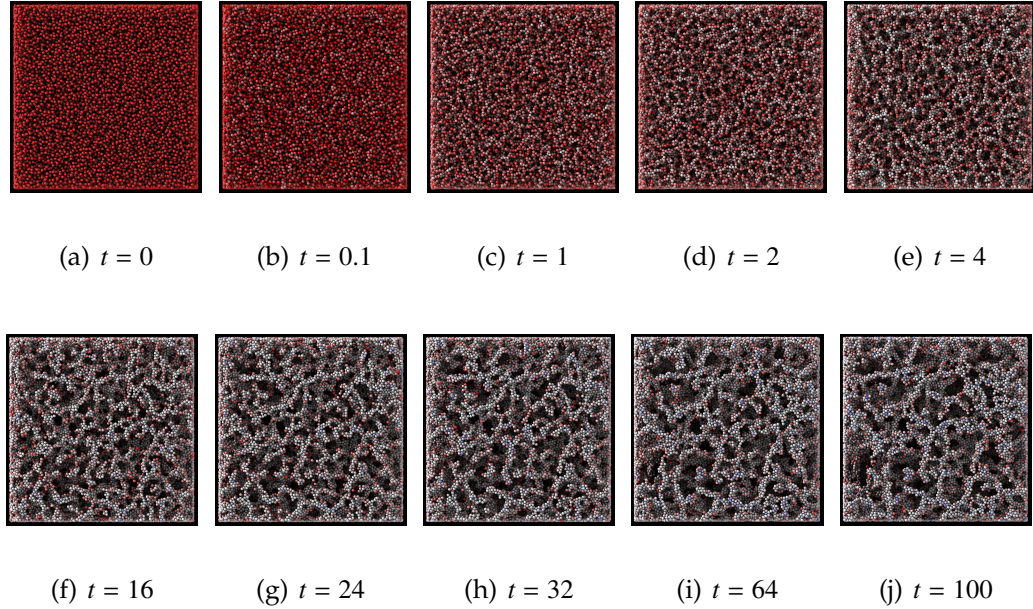


Figure 5.13: Gelation of a hydrodynamically-interacting colloidal suspension under quiescent conditions at $t=0, 0.1, 2, 4, 16, 24, 32, 64, 100$ Brownian times. The time is non-dimensional as it is scaled by a^2/D . These pictures depict the colloids self-assembly dynamics as they form complex bi-continuous space-spanning structures within the fluid. Buried particles (blue) might be in glassy arrest (as shown in [149]) and surface particles (red) are expected to be more mobile. The parameters utilized for the parallel ASD method under quiescent conditions are: $N = 102, 400, N_x = 256$ a Brownian force with ASDB-nf and an inter particle force.

tance of $2.2a$ (we define this as the contact number), the attraction range, of each particle, with red for particles with few contacts to blue for many contacts.

As shown in the figures, initially the configuration is an equilibrium unperturbed suspension and particles are far away from each other. As the time evolves, particles accumulate due to the attractive force and strands self-assemble and branch to form a complex soft material.

Finally in figure 5.14 (a) the evolution of the Brownian pressure. The Brownian pressure grows to a positive value at early time and remains so, indicating that particles are nearby due to the attractive inter-particle interaction and thus

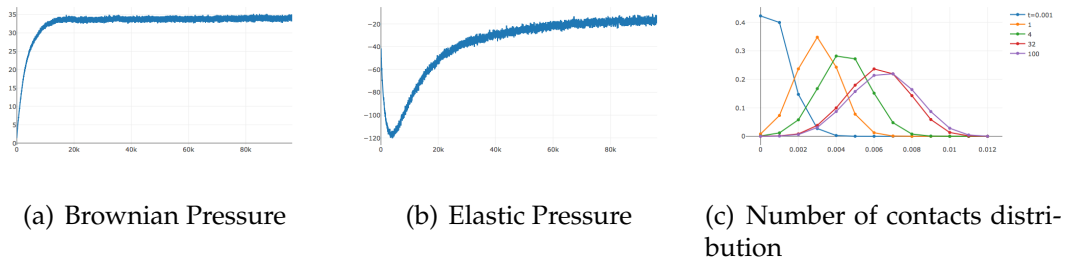


Figure 5.14: Evolution of macroscopic and microscopic properties during gelation. On left the Brownian pressure, on the middle the elastic pressure and on the right the number of contact-number distribution. The colloidal suspension with particle concentration of $\phi = 0.2$ is under quiescent conditions with attraction of strength $5KT$ and range $\kappa = 30$. The parameters utilized for the parallel ASD method are: $N = 102,400$, $N_x = 256$ a Brownian force with ASDB-nf and an inter particle force.

the small molecules within the fluid exert a Brownian but correlated force on the colloids to push particles apart. In figure 5.14 (b) we show the dynamic evolution of the elastic pressure defined by $\langle -\frac{1}{3} \mathbf{I} : \mathbf{rF}_p \rangle$. The elastic pressure is negative, consistent with a condensation process that acts to form the gel network or particle-rich phase. In 5.14 (c) the time evolution of the distribution of the contact-number. Overall, the unsteady elastic pressure and contact number distribution shows an increasing number of bonds and ongoing condensation.

5.4 Summary

In this chapter, we introduced algorithms for the parallelization of Accelerated Stokesian Dynamics. We presented the main ingredients required to have a scalable code for the different parts of ASD. We explained in details the far-field parallelization, the near-field parallelization and the near-field far-field communication due to their inherent coupling. We showed that the code is scalable up to $O(10^4)$ processors for $O(10^6)$ particles in different scenarios such as inter par-

ticle force, shear flow and correlated Brownian motion. This chapter focused on distributed memory architectures and we demonstrated the ability of our algorithms to handle large-scale dynamic simulations. Future work can explore hybrid strategies such as MPI-openmp or MPI-GPU programming models for further speedup. This chapter demonstrated how near-field preconditioning is critical and future research will be devoted on preconditioning the dense and matrix-free linear system. Subsequent research will leverage the algorithms we developed to study in depth large-scale stochastic particle systems with hydrodynamic interactions such as colloidal gels and colloidal glass.

CHAPTER 6

CONCLUSION

In this dissertation, we developed theoretical and computational models to study colloidal suspensions with many-body hydrodynamic interactions in Stokes flow. Accelerated Stokesian Dynamics (ASD) simulation is a powerful tool to study many-body hydrodynamic interactions. However, due to the complexity of the algorithm, it only has the capacity to simulate $O(10^3)$ particles, which limits its application to large systems, such as colloidal gels. In Chapter 2 and 3, we attempt to solve this problem from the theoretical perspective. Jeffrey and Onishi [84] derived a set of mobility functions for a pair of particles suspended in Stokes flow analytically. Thus given force derivatives acting on the surfaces of the particle pairs, with these mobility couplings we can obtain their motion. For N particles suspended in the fluid, due to the complexity of the boundary condition, analytical solutions are intractable. However, if we only view a pair of particles in the fluid and treat any intervening particles between the pair and solvent together as an effective medium, a pair-level model can be constructed similarly. To obtain the effective pair-level mobility couplings in concentrated suspensions, we developed a new stochastic algorithm to extract hydrodynamic couplings via ASD simulations. In Chapter 2, we derived the coupling between forces and particle motion. In addition, we observed that the hydrodynamic couplings always decay as $1/r$ for suspension from dilute ($\phi = 0.01$) to concentrated ($\phi = 0.55$). This phenomenon indicates that hydrodynamic interactions are not screened in even very concentrated suspensions. Neglecting long-range hydrodynamic interactions in concentrated colloidal suspensions would be invalid. In Chapter 3, we followed the stochastic algorithm and derived hydrodynamic couplings between stresslet and straining

motion. Combining with the couplings derived in Chapter 2, these functions constitute a full set of mobility functions for colloidal suspensions. Furthermore, we plugged the coupling between stresslet and straining motion to the Smoluchowski theory to compute the high-frequency viscosity. The good fit between our results and simulation results indicates that these functions can be utilized analytically to study near-equilibrium rheology.

In Chapter 4, we studied microviscosity and normal stress in microrheology. We developed a scaling theory for normal stress utilizing these concentrated mobility functions. We find that in high- Pe regime, the stresslet scales as Pe^δ , where δ is a ratio between longitudinal and transverse mobility functions. With a further analysis of the scaling, we explained that the three-body hydrodynamic interactions induce the non-Newtonian rheology by breaking the fore-aft symmetry via the transverse mobility.

To study colloidal suspensions with many-body hydrodynamic interactions in large-scale systems, we also developed computational model, which is an extension of the current ASD algorithm. The traditional ASD algorithm is sequential and limits to $O(10^3)$ particles. To study multi-length scale system with $O(10^5)$ particles, we developed a massive parallelized ASD algorithm which can handle $O(10^5)$ particles in $O(10^3)$ processors. The foundation of our parallelized algorithm is two matrix-vector multiplication. The near-field multiplication involves direct construction of sparse near-field hydrodynamic interaction matrix, which requires local message transfer between neighbor processors. The message transfer is based on a spatial decomposition of the whole system and each subdomain and particles inside are assigned to a processor to handle the sub-computation. The far-field multiplication is essentially a matrix-free algo-

rithm which involves multiple Fast Fourier Transform (FFT) in each time step. The parallelized FFT requires all-to-all communication from all the processors. The decomposition of parallelized FFT algorithm is different from the near-field portion, thus requires two additional all-to-all message transfer to transform decomposition topology. Current parallel scales well as number of particles increase. To further accelerate the algorithm, one requires to find a far-field matrix-free preconditioner which can significantly reduce the number of iterations in far-field solver as the number of particles and thus the condition number of the far-field matrix increase.

BIBLIOGRAPHY

- [1] Y Almog and H Brenner. Non-continuum anomalies in the apparent viscosity experienced by a test sphere moving through an otherwise quiescent suspension. *Physics of Fluids*, 9(1):16–22, 1997.
- [2] Tadashi Ando, Edmond Chow, Yousef Saad, and Jeffrey Skolnick. Krylov subspace methods for computing hydrodynamic interactions in brownian dynamics simulations. *The Journal of chemical physics*, 137(6):064106, 2012.
- [3] Christian Aponte-Rivera and Roseanna N Zia. Simulation of hydrodynamically interacting particles confined by a spherical cavity. *Physical Review Fluids*, 1(2):023301, 2016.
- [4] Christian Aponte-Rivera and Roseanna N. Zia. Concentrated mobility in spherically confined suspensions. *In preparation*, 2017.
- [5] Christian Aponte-Rivera, Yu Su, and Roseanna N Zia. Equilibrium diffusion in concentrated, 3d confined suspensions. *In preparation*.
- [6] Satish Balay, Jed Brown, , Kris Buschelman, Victor Eijkhout, William D. Gropp, Dinesh Kaushik, Matthew G. Knepley, Lois Curfman McInnes, Barry F. Smith, and Hong Zhang. *PETSc Users Manual*. Argonne National Laboratory, 2012.
- [7] A. J. Banchio, J. Bergenholz, and G. Nägele. Rheology and dynamics of colloidal suspensions. *Phys. Rev. Lett.*, 82(8):1792, 1999.
- [8] Adolfo J Banchio and John F Brady. Accelerated stokesian dynamics: Brownian motion. *J. Chem. Phys.*, 118(22):10323–10332, 2003.

- [9] Adolfo J Banchio, Jacek Gapinski, Adam Patkowski, Wolfgang Häußler, Andrei Fluerasu, Stefano Sacanna, Peter Holmqvist, Gerhard Meier, M Paul Lettinga, and Gerhard Nägele. Many-body hydrodynamic interactions in charge-stabilized suspensions. *Physical review letters*, 96(13):138303, 2006.
- [10] H. A. Barnes. Shear thickening (“dilatancy”) in suspensions of nonaggregating solid particles dispersed in newtonian liquids. *J. Rheol.*, 33, 1989.
- [11] H. A. Barnes. Shear-Thickening (“Dilatancy”) in Suspensions of Nonaggregating Solid Particles Dispersed in Newtonian Liquids. *J. Rheol.*, 33(2):329–366, 1989.
- [12] G. K. Batchelor. The stress in a suspension of force-free particles. *J. Fluid Mech.*, 41(3):545–570, 1970.
- [13] G. K. Batchelor. Brownian diffusion of particles with hydrodynamic interaction. *J. Fluid Mech.*, 74:1–29, 1976.
- [14] G. K. Batchelor. The effect of Brownian motion on the bulk stress in a suspension of spherical particles. *J. Fluid Mech.*, 83:97–117, 1977.
- [15] G. K. Batchelor. Diffusion in a dilute polydisperse system of interacting spheres. *J. Fluid Mech.*, 131:155–175, 1983.
- [16] G. K. Batchelor and J. T. Green. The hydrodynamic interaction of two small freely-moving spheres in a linear flow field. *J. Fluid Mech.*, 56(2):375–400, 1972.
- [17] GK Batchelor. Brownian diffusion of particles with hydrodynamic interaction. *Journal of Fluid Mechanics*, 74(01):1–29, 1976.

- [18] GK Batchelor and JT Green. The determination of the bulk stress in a suspension of spherical particles to order c^2 . *J. Fluid Mech.*, 56(03):401–427, 1972.
- [19] GK Batchelor and C-S Wen. Sedimentation in a dilute polydisperse system of interacting spheres. part 2. numerical results. *Journal of Fluid Mechanics*, 124:495–528, 1982.
- [20] C.W.J. Beenakker. The effective viscosity of a concentrated suspension of spheres (and its relation to diffusion). *Physica A: Statistical Mechanics and its Applications*, 128(1-2):48–81, 1984.
- [21] C.W.J. Beenakker and P. Mazur. Diffusion of spheres in a concentrated suspension II. *Physica A: Statistical Mechanics and its Applications*, 126(3):349–370, 1984.
- [22] J. W. Bender and N. J. Wagner. Optical measurement of the contributions of colloidal forces to the rheology of concentrated suspensions. *J. Colloid Interface Sci.*, 172(1):171–184, 1995.
- [23] Michele Benzi. Preconditioning techniques for large linear systems: A survey. *J. Comput. Phys.*, 182(2):418–477, November 2002.
- [24] J. Bergenholtz, J. F. Brady, and M. Vicic. The non-Newtonian rheology of dilute colloidal suspensions. *J. Fluid Mech.*, 456:239–275, 2002.
- [25] Michel Bergmann and Angelo Iollo. Bioinspired swimming simulations. *Journal of Computational Physics*, 323:310–321, 2016.
- [26] G. Bossis and J. F. Brady. Self-diffusion of Brownian particles in concentrated suspensions under shear. *The Journal of Chemical Physics*, 87(9):5437, 1987.

- [27] J. F. Brady. The rheological behavior of concentrated colloidal dispersions. *J. Chem Phys.*, 99(1):567–581, 1993.
- [28] J. F. Brady and G. Bossis. The rheology of concentrated suspensions of spheres in simple shear flow by numerical simulation. *J. Fluid Mech.*, 155: 105–129, 1985.
- [29] John F. Brady. The long-time self-diffusivity in concentrated colloidal dispersions. *Journal of Fluid Mechanics*, 272(-1):109, 1994.
- [30] John F. Brady. Computer simulation of viscous suspensions. *Chemical Engineering Science*, 56(9):2921–2926, 2001.
- [31] John F Brady and Georges Bossis. Stokesian dynamics. *Ann. Rev. Fluid Mech.*, 20:111–157, 1988.
- [32] Wim-Paul Breugem. A second-order accurate immersed boundary method for fully resolved simulations of particle-laden flows. *Journal of Computational Physics*, 231(13):4469–4498, 2012.
- [33] HC Brinkman. A calculation of the viscous force exerted by a flowing fluid on a dense swarm of particles. *Flow, Turbulence and Combustion*, 1(1): 27, 1949.
- [34] F. Bülow, P. Hamberger, H. Nirschl, and W. Dörfler. A parallel implementation of the stokesian dynamics method applied to the simulation of colloidal suspensions. *Computers and Fluids*, 103:156 – 165, 2014.
- [35] F. Bülow, P. Hamberger, H. Nirschl, and W. Dörfler. A scalable parallel stokesian dynamics method for the simulation of colloidal suspensions. *Computer Physics Communications*, 204:107 – 120, 2016.

- [36] Norman F Carnahan and Kenneth E Starling. Equation of state for nonattracting rigid spheres. *The Journal of Chemical Physics*, 51(2):635–636, 1969.
- [37] Frédéric Chantalat, Charles-Henri Bruneau, Cédric Galusinski, and Angelo Iollo. Level-set, penalization and cartesian meshes: A paradigm for inverse problems and optimal design. *Journal of Computational Physics*, 228(17):6291–6315, 2009.
- [38] Edmond Chow and Aftab Patel. Fine-grained parallel incomplete lu factorization. *SIAM journal on Scientific Computing*, 37(2):C169–C193, 2015.
- [39] Henry CW Chu and Roseanna N Zia. Active microrheology of hydrodynamically interacting colloids: Normal stresses and entropic energy density. *J. Rheol.*, 60(4):755–781, 2016.
- [40] Henry C.W. Chu and Roseanna N. Zia. The non-Newtonian rheology of hydrodynamically interacting colloids via active, nonlinear microrheology. *Journal of Rheology*, page In preparation, 2016.
- [41] Henry C.W. Chu and Roseanna N. Zia. Active microrheology of hydrodynamically interacting spheres: Normal stresses. *Journal of Rheology*, page In review, 2016.
- [42] B. Cichocki and B. U. Felderhof. Diffusion coefficients and effective viscosity of suspensions of sticky hard spheres with hydrodynamic interactions. *J. Chem. Phys.*, 93(6):4427 – 4432, 1990.
- [43] EGD Cohen and IM de Schepper. The colloidal many body problem: Colloidal suspensions as hard sphere fluids. In *Recent Progress in Many-body Theories*, pages 387–395. Springer, 1992.

- [44] James W Cooley and John W Tukey. An algorithm for the machine calculation of complex fourier series. *Mathematics of computation*, 19(90):297–301, 1965.
- [45] John C Crocker, Megan T Valentine, Eric R Weeks, Thomas Gisler, Peter D Kaplan, Arjun G Yodh, and David A Weitz. Two-point microrheology of inhomogeneous soft materials. *Physical Review Letters*, 85(4):888, 2000.
- [46] G. Cummins, H. Z. and Li, W. M. Du, and J. Hernandez. Relaxation dynamics in supercooled liquids. *Physica A*, 204:169–201, 1994.
- [47] SL Dance and MR Maxey. Incorporation of lubrication effects into the force-coupling method for particulate two-phase flow. *Journal of computational Physics*, 189(1):212–238, 2003.
- [48] Tom Darden, Darrin York, and Lee Pedersen. Particle mesh Ewald: An N-log(N) method for Ewald sums in large systems. *The Journal of Chemical Physics*, 98(12):10089–10092, June 1993.
- [49] R. H. Davis and N. A. Hill. Hydrodynamic diffusion of a sphere sedimenting through a dilute suspension of neutrally buoyant spheres. *J. Fluid Mech.*, 236:513–533, 1992.
- [50] I. M. de Schepper, H. E. Smorenburg, and E. D. Cohen. Viscoelasticity in dense hard sphere colloids. *Phys. Rev. Lett.*, 70(14):2178–2181, 1993.
- [51] P. D’Haene, J. Mewis, and G. Fuller. Scattering dichroism measurements of flow-induced structure of a shear thickening suspension. *J. Colloid Interface Sci.*, 156:350–358, 1993.
- [52] Steven Diamond and Stephen Boyd. Stochastic matrix-free equilibration. *Journal of Optimization Theory and Applications*, 172(2):436–454, 2017.

- [53] German Drazer, Joel Koplik, Boris Khusid, and Andreas Acrivos. Deterministic and stochastic behaviour of non-brownian spheres in sheared suspensions. *Journal of Fluid Mechanics*, 460:307–335, 2002.
- [54] L Durlofsky and J. F. Brady. Analysis of the Brinkman equation as a model for flow in porous media. *Physics of Fluids*, 30(11):3329–3341, 1987.
- [55] Louis Durlofsky, John F Brady, and Georges Bossis. Dynamic simulation of hydrodynamically interacting particles. *J. Fluid Mech.*, 180:21–49, 1987.
- [56] A. Einstein. On the theory of the Brownian movement. *Ann. der Physik*, 19(4):371–381, 1906.
- [57] Donald L. Ermak and J. A. McCammon. Brownian dynamics with hydrodynamic interactions. *The Journal of Chemical Physics*, 69(4):1352–1360, August 1978.
- [58] B.U. Felderhof. Brownian motion and creeping flow on the Smoluchowski time scale. *Physica A: Statistical Mechanics and its Applications*, 147(1-2): 203–218, 1987.
- [59] B.U. Felderhof. Brownian motion and creeping flow on the Smoluchowski time scale. *Physica A: Statistical Mechanics and its Applications*, 147(1-2): 203–218, 1987.
- [60] David R Foss and John F Brady. Self-diffusion in sheared suspensions by dynamic simulation. *Journal of fluid mechanics*, 401:243–274, 1999.
- [61] David R. Foss and John F. Brady. Brownian Dynamics simulation of hard-sphere colloidal dispersions. *Journal of Rheology*, 44(3):629, 2000.

- [62] David R Foss and John F Brady. Structure, diffusion and rheology of brownian suspensions by stokesian dynamics simulation. *Journal of Fluid Mechanics*, 407:167–200, 2000.
- [63] Matteo Frigo and Steven G Johnson. The design and implementation of fftw3. *Proceedings of the IEEE*, 93(2):216–231, 2005.
- [64] M. Fuchs and M. E. Cates. Schematic models for dynamic yielding of sheared colloidal glasses. *Faraday discussions*, 123:267–286, 2003.
- [65] Matthias Fuchs and Michael E Cates. Theory of nonlinear rheology and yielding of dense colloidal suspensions. *Physical review letters*, 89(24):248304, 2002.
- [66] F Gadala-Maria and Andreas Acrivos. Shear-induced structure in a concentrated suspension of solid spheres. *Journal of Rheology*, 24(6):799–814, 1980.
- [67] I. Gazuz, A. M. Puertas, T. Voigtmann, and M. Fuchs. Active and nonlinear microrheology in dense colloidal suspensions. *Phys. Rev. Lett.*, 102(24):248302, 2009.
- [68] Frederic Gibou, David Hyde, and Ron Fedkiw. Sharp interface approaches and deep learning techniques for multiphase flows. *Journal of Computational Physics*, 2018.
- [69] Roland Glowinski. Finite element methods for incompressible viscous flow. *Handbook of numerical analysis*, 9:3–1176, 2003.
- [70] Roland Glowinski, Tsorng-Whay Pan, Todd I Hesla, Daniel D Joseph, and Jacques Periaux. A fictitious domain approach to the direct numerical

- simulation of incompressible viscous flow past moving rigid bodies: application to particulate flow. *Journal of Computational Physics*, 169(2):363–426, 2001.
- [71] W. Gotze. “Aspects of structural glass transitions,” in *Liquids, Freezing and the Glass Transition*. Elsevier, New York, 1991.
- [72] Leslie Greengard and June-Yub Lee. Accelerating the nonuniform fast fourier transform. *SIAM review*, 46(3):443–454, 2004.
- [73] Leslie Greengard and Vladimir Rokhlin. A fast algorithm for particle simulations. *Journal of computational physics*, 73(2):325–348, 1987.
- [74] Arthur Guittet, Maxime Theillard, and Frédéric Gibou. A stable projection method for the incompressible navier–stokes equations on arbitrary geometries and adaptive quad/octrees. *Journal of Computational Physics*, 292:215–238, 2015.
- [75] H. Hasimoto. On the periodic fundamental solutions of the Stokes equations and their application to viscous flow past a cubic array of spheres. *Journal of Fluid Mechanics*, 5(2):317–328, 1959.
- [76] W. Hess and R. Klein. Generalized hydrodynamics of systems of interacting brownian particles. *Advances in Physics*, 32(2):173C–283, 1983.
- [77] NJ Hoh and RN Zia. Hydrodynamic diffusion in active microrheology of non-colloidal suspensions: the role of interparticle forces. *Journal of Fluid Mechanics*, 785:189–218, 2015.
- [78] PJ Hoogerbrugge and JMVA Koelman. Simulating microscopic hydrodynamic phenomena with dissipative particle dynamics. *EPL (Europhysics Letters)*, 19(3):155, 1992.

- [79] Howard H Hu. Direct simulation of flows of solid-liquid mixtures. *International Journal of Multiphase Flow*, 22(2):335–352, 1996.
- [80] Howard H Hu, Neelesh A Patankar, and MY Zhu. Direct numerical simulations of fluid–solid systems using the arbitrary lagrangian–eulerian technique. *Journal of Computational Physics*, 169(2):427–462, 2001.
- [81] Thomas JR Hughes, Wing Kam Liu, and Thomas K Zimmermann. Lagrangian-eulerian finite element formulation for incompressible viscous flows. *Computer methods in applied mechanics and engineering*, 29(3):329–349, 1981.
- [82] Imre M Jánosi, Tamás Tél, Dietrich E Wolf, and Jason AC Gallas. Chaotic particle dynamics in viscous flows: The three-particle stokeslet problem. *Physical Review E*, 56(3):2858, 1997.
- [83] D.J. Jeffrey. The calculation of the low reynolds number resistance functions for two unequal spheres. *Phys. Fluids A*, 4(1):16–29, 1992.
- [84] D.J. Jeffrey and Y. Onishi. Calculation of the resistance and mobility functions for two unequal rigid spheres in low-reynolds-number flow. *J. Fluid Mech.*, 139:261–290, 1984.
- [85] DJ Jeffrey, JF Morris, and John F Brady. The pressure moments for two rigid spheres in low-reynolds-number flow. *Physics of Fluids A: Fluid Dynamics*, 5(10):2317–2325, 1993.
- [86] Eric E Keaveny and Michael J Shelley. Applying a second-kind boundary integral equation for surface tractions in stokes flow. *Journal of Computational Physics*, 230(5):2141–2159, 2011.

- [87] Aditya S Khair and John F Brady. Single particle motion in colloidal dispersions: a simple model for active and nonlinear microrheology. *Journal of Fluid Mechanics*, 557:73–117, 2006.
- [88] S. Kim and S. J. Karrila. *Microhydrodynamics: principles and selected applications*. Butterworth-Heinemann, Boston, 1991.
- [89] S. Kim and R.T. Mifflin. The resistance and mobility functions of two equal spheres in low-reynolds-number flow. *Phys. Fluids*, 28(7):2033–2045, 1985.
- [90] Anthony JC Ladd. Hydrodynamic transport coefficients of random dispersions of hard spheres. *The Journal of chemical physics*, 93(5):3484–3494, 1990.
- [91] Anthony JC Ladd. Numerical simulations of particulate suspensions via a discretized boltzmann equation. part 1. theoretical foundation. *Journal of fluid mechanics*, 271:285–309, 1994.
- [92] Anthony JC Ladd. Numerical simulations of particulate suspensions via a discretized boltzmann equation. part 2. numerical results. *Journal of fluid mechanics*, 271:311–339, 1994.
- [93] Anthony JC Ladd. Hydrodynamic screening in sedimenting suspensions of non-brownian spheres. *Physical review letters*, 76(8):1392, 1996.
- [94] OA Ladyzhenskaya. The mathematical theory of incompressible viscous flows. *Gordon and Breach, New York*, 1963.
- [95] Benjamin J. Landrum, William B. Russel, and Roseanna N. Zia. Delayed yield in colloidal gels: Creep, flow, and re-entrant solid regimes. *Journal of Rheology*, 60(4):783–807, 2016. doi: 10.1122/1.4954640.

- [96] P. Langevin. Sur la thorie du mouvement brownien. *C. R. Acad. Sci.*, 146, 1908.
- [97] D. Leighton and A. Acrivos. The shear-induced migration of particles in concentrated suspensions. *J. Fluid Mech.*, 181:415 – 439, 1987.
- [98] Mathieu Lepilliez, Elena Roxana Popescu, Frederic Gibou, and Sébastien Tanguy. On two-phase flow solvers in irregular domains with contact line. *Journal of Computational Physics*, 321:1217–1251, 2016.
- [99] Alexander M. Leshansky and John F. Brady. Dynamic structure factor study of diffusion in strongly sheared suspensions. *Journal of Fluid Mechanics*, 527:141–169, 2005.
- [100] Alex J Levine and TC Lubensky. One-and two-particle microrheology. *Physical review letters*, 85(8):1774, 2000.
- [101] Alex J Levine and TC Lubensky. Response function of a sphere in a viscoelastic two-fluid medium. *Physical Review E*, 63(4):041510, 2001.
- [102] Alex J Levine and TC Lubensky. Two-point microrheology and the electrostatic analogy. *Physical Review E*, 65(1):011501, 2001.
- [103] EM Lifshitz and LD Landau. Course of theoretical physics, volume 6, fluid mechanics, 1959.
- [104] R. A. Lionberger and W. B. Russel. High frequency modulus of hard sphere colloids. *J. Rheol.*, 38(6):1885–1908, 1994.
- [105] R. a. Lionberger and W. B. Russel. Effectiveness of nonequilibrium closures for the many body forces in concentrated colloidal dispersions. *J. Chem. Phys.*, 106(1):402–416, 1997.

- [106] RA Lionberger and WB Russel. A smoluchowski theory with simple approximations for hydrodynamic interactions in concentrated dispersions. *Journal of Rheology*, 41(2):399–425, 1997.
- [107] D Liu, Eric E Keaveny, Martin R Maxey, and George E Karniadakis. Force-coupling method for flows with ellipsoidal particles. *Journal of Computational Physics*, 228(10):3559–3581, 2009.
- [108] Sune Lomholt and Martin R. Maxey. Force-coupling method for particulate two-phase flow: Stokes flow. *J. Comput. Phys.*, 184(2):381–405, January 2003.
- [109] Xian Luo, Martin R Maxey, and George Em Karniadakis. Smoothed profile method for particulate flows: Error analysis and simulations. *Journal of Computational Physics*, 228(5):1750–1769, 2009.
- [110] B.J. Maranzano and N.J. Wagner. Flow-small angle neutron scattering measurements of colloidal dispersion microstructure evolution through the shear thickening transition. *J. Chem. Phys.*, 117:10291–10302, 2002.
- [111] Marco Marchioro and Andreas Acrivos. Shear-induced particle diffusivities from numerical simulations. *Journal of fluid mechanics*, 443:101–128, 2001.
- [112] Martin Maxey. Simulation methods for particulate flows and concentrated suspensions. *Annual Review of Fluid Mechanics*, 49(1):171–193, 2017.
- [113] Bloen Metzger and Jason E. Butler. Clouds of particles in a periodic shear flow. *Physics of Fluids*, 24(2):021703, 2012.
- [114] Mohammad Mirzadeh, Arthur Guittet, Carsten Burstedde, and Frederic

- Gibou. Parallel level-set methods on adaptive tree-based grids. *Journal of Computational Physics*, 322(Supplement C):345 – 364, 2016.
- [115] G Nägele and J Bergenholz. Linear viscoelasticity of colloidal mixtures. *The Journal of chemical physics*, 108(23):9893–9904, 1998.
- [116] G. Nägele and J. K. G. Dhont. Tracer-diffusion in colloidal mixtures: A mode-coupling scheme with hydrodynamic interactions. *J. Chem. Phys.*, 108(22):9566–9576, 1998.
- [117] Yasuya Nakayama and Ryoichi Yamamoto. Simulation method to resolve hydrodynamic interactions in colloidal dispersions. *Physical Review E*, 71 (3):036707, 2005.
- [118] Ehssan Nazockdast and Jeffrey F Morris. Microstructural theory and the rheology of concentrated colloidal suspensions. *J. Fluid Mech.*, 713:420–452, 2012.
- [119] Ehssan Nazockdast and Jeffrey F Morris. Pair-particle dynamics and microstructure in sheared colloidal suspensions: Simulation and smoluchowski theory. *Phys. Fluids*, 25(7):070601, 2013.
- [120] Shailesh S Ozarkar and Ashok S Sangani. A method for determining stokes flow around particles near a wall or in a thin film bounded by a wall and a gas-liquid interface. *Physics of Fluids*, 20(6):063301, 2008.
- [121] Dmitry Pekurovsky. P3DFFT: A Framework for Parallel Computations of Fourier Transforms in Three Dimensions. *SIAM Journal on Scientific Computing*, 34(4):C192–C209, January 2012.
- [122] Jerome K Percus and George J Yevick. Analysis of classical statistical mechanics by means of collective coordinates. *Physical Review*, 110(1):1, 1958.

- [123] Charles S Peskin. The immersed boundary method. *Acta numerica*, 11:479–517, 2002.
- [124] Thanh N. Phung, John F. Brady, and Georges Bossis. Stokesian Dynamics simulation of Brownian suspensions. *Journal of Fluid Mechanics*, 313:181–207, apr 1996.
- [125] Thanh Ngoc Phung. Behavior of concentrated colloidal suspensions by stokesian dynamics simulation. 1993.
- [126] DJ Pine, Jerry P Gollub, JF Brady, and AM Leshansky. Chaos and threshold for irreversibility in sheared suspensions. *Nature*, 438(7070):997–1000, 2005.
- [127] Steve Plimpton. Fast parallel algorithms for short-range molecular dynamics. *Journal of computational physics*, 117(1):1–19, 1995.
- [128] A. Prosperetti and G. Tryggvason. *Computational methods for multiphase flow*. Cambridge university press, 2009.
- [129] P.N. Pusey, H.N.W. Lekkerkerker, E.G.D. Cohen, and I.M. de Schepper. Analogies between the dynamics of concentrated charged colloidal suspensions and dense atomic liquids. *Physica A: Statistical Mechanics and its Applications*, 164(1):12–27, 1990.
- [130] MD Rintoul and Salvatore Torquato. Computer simulations of dense hard-sphere systems. *The Journal of chemical physics*, 105(20):9258–9265, 1996.
- [131] William B Russel. The huggins coefficient as a means for characterizing suspended particles. *Journal of the Chemical Society, Faraday Transactions 2: Molecular and Chemical Physics*, 80(1):31–41, 1984.

- [132] Ashok S Sangani and Guobiao Mo. An $O(n)$ algorithm for stokes and laplace interactions of particles. *Physics of Fluids*, 8(8):1990–2010, 1996.
- [133] Asimina Sierou and John F Brady. Accelerated stokesian dynamics simulations. *J. Fluid Mech.*, 448:115–146, 2001.
- [134] Asimina Sierou and John F. Brady. Shear-induced self-diffusion in non-colloidal suspensions. *Journal of Fluid Mechanics*, 506:285–314, may 2004.
- [135] Todd M Squires and John F Brady. A simple paradigm for active and non-linear microrheology. *Physics of Fluids (1994-present)*, 17(7):073101, 2005.
- [136] Yu Su, James W Swan, and Roseanna N Zia. Pair mobility functions for rigid spheres in concentrated colloidal dispersions: Stresslet and straining motion couplings. *The Journal of chemical physics*, 146(12):124903, 2017.
- [137] J. W. Swan and J. F. Brady. Simulation of hydrodynamically interacting particles near a no-slip boundary. *Physics of Fluids*, 19(11), 2007.
- [138] James W. Swan and John F. Brady. The hydrodynamics of confined dispersions. *Journal of Fluid Mechanics*, 687:254–299, 2011.
- [139] James W Swan and Gang Wang. Rapid calculation of hydrodynamic and transport properties in concentrated solutions of colloidal particles and macromolecules. *Physics of Fluids*, 28(1):011902, 2016.
- [140] M. Tokuyama and I. Oppenheim. On the theory of concentrated hard-sphere suspensions. *Physica A*, 216(1):85–119, 1995.
- [141] Lloyd N. Trefethen and David Bau. *Numerical Linear Algebra*. SIAM, 1997.
ISBN 0898713617.

- [142] Marian Von Smoluchowski. Zur kinetischen theorie der brownschen molekularbewegung und der suspensionen. *Annalen der physik*, 326(14):756–780, 1906.
- [143] N. J. Wagner and J. F. Brady. Shear thickening in colloidal dispersions. *Phys. Today*, 2009.
- [144] Mu Wang and John F. Brady. Spectral ewald acceleration of stokesian dynamics for polydisperse suspensions. *Journal of Computational Physics*, 306:443 – 477, 2016.
- [145] Kyongmin Yeo and Martin R Maxey. Simulation of concentrated suspensions using the force-coupling method. *Journal of computational physics*, 229(6):2401–2421, 2010.
- [146] GK Youngren and Andrias Acrivos. Stokes flow past a particle of arbitrary shape: a numerical method of solution. *Journal of fluid Mechanics*, 69(2):377–403, 1975.
- [147] Roseanna N Zia. Active and passive microrheology: Theory and simulation. *Annual Review of Fluid Mechanics*, (0), 2018.
- [148] Roseanna N Zia and John F Brady. Microviscosity, microdiffusivity, and normal stresses in colloidal dispersions. *Journal of Rheology*, 56(5):1175–1208, 2012.
- [149] Roseanna N. Zia, Benjamin J. Landrum, and William B. Russel. A micro-mechanical study of coarsening and rheology of colloidal gels: Cage building, cage hopping, and Smoluchowski’s ratchet. *Journal of Rheology*, 58(5):1121–1157, sep 2014.

- [150] Roseanna N Zia, James W Swan, and Yu Su. Pair mobility functions for rigid spheres in concentrated colloidal dispersions: force, torque, translation, and rotation. *Journal of Chemical Physics*, 143(224901), 2015.